12-2012

Investigating the Prediction of High Resolution Heat Waves and Extreme Precipitation and the Impact of Heat Waves on Air Quality in U.S. in the 21st Century

Yang Gao
ygao13@utk.edu

To the Graduate Council:

I am submitting herewith a dissertation written by Yang Gao entitled "Investigating the Prediction of High Resolution Heat Waves and Extreme Precipitation and the Impact of Heat Waves on Air Quality in U.S. in the 21st Century." I have examined the final electronic copy of this dissertation for form and content and recommend that it be accepted in partial fulfillment of the requirements for the degree of Doctor of Philosophy, with a major in Civil Engineering.

Joshua S. Fu, Major Professor

We have read this dissertation and recommend its acceptance:

Wayne T. Davis, John B. Drake, Yilu Liu

Accepted for the Council:

Carolyn R. Hodges

Vice Provost and Dean of the Graduate School

(Original signatures are on file with official student records.)

Investigating the Prediction of High Resolution Heat Waves and Extreme Precipitation and the Impact of Heat Waves on Air Quality in U.S. in the 21st Century

A Dissertation Presented for the
Doctor of Philosophy Degree
The University of Tennessee, Knoxville

Yang Gao
December 2012

DEDICATION

I dedicate this dissertation to my family for their endless love and support.

ACKNOWLEDGEMENTS

I would like to thank all those who have helped me in these past thirty years and in my graduate study. First of all, I would like to thank my advisor, Dr. Joshua S. Fu, for his sincere help in both my research and personal life since 2008. With his outstanding teaching skill, I became very interested in research and was able to learn much faster. In addition to research, I also learnt a lot from him on how to communicate with others and work in a team, a skill important for my future. As my committee member, Dr. John B. Drake has been intensively involved in my research study. I really appreciate his efforts on improving my modeling ability and writing skill. As the Dean of the College of Engineering, Dr. Wayne T. Davis has a tight schedule. Yet despite this, when I need a recommendation letter, he responds to me immediately. I really appreciate his support and encouragement. As my committee member, Dr. Yilu Liu has provided invaluable comments on my research design and for improvement of the dissertation. Dr. Jean-Francois Lamarque from the National Center for Atmospheric Research has kindly helped me on the climate and chemistry modeling, and I appreciate his time. I thank Dr. Yang Liu from Emory University for the insight comments on my research and publication.

There are many friends who have helped me. I can not list them all, but I bear in mind all their individual contributions. In particular, I would like to thank Dr. David C. Wong from the U.S. EPA, Dr. Yun-Fat Lam from City University of Hong Kong, Dr. Kan Huang, Melissa R. Allen and Scott DeNeale.

ABSTRACT

In this study, the perennial problem of scale is addressed with an updated set of modeling tools that include global climate, atmospheric chemistry simulation, mesoscale weather, and air quality simulations. The evaluation of coupled model performance across geographic scales and the assessment of local scale climate change impacts under a fossil fuel intensive climate change scenario Representative Concentration Pathway (RCP 8.5) was achieved by linking the global climate model Community Earth System Model (CESM), with the regional climate model Weather Research and Forecasting (WRF) Model. This study is the first evaluation of dynamical downscaling using WRF on a 4km by 4km high resolution scale in the eastern US driven by the CESM. First, the global and regional climate model results were evaluated, and an inconsistency in skin temperature during the downscaling process was corrected by modifying the land/sea mask. In comparison with observations, WRF shows statistically significant improvement over CESM in reproducing extreme weather events, with improvement for heat wave frequency estimation as high as 98%. The RCP 8.5 was used to study a possible future mid-century climate extreme in 2057-2059. Both heat waves and extreme precipitation in 2057-2059 are more severe than present climate in the Eastern US. The Northeastern US shows large increases in both heat wave intensity (3.05 ºC higher) and annual extreme precipitation (107.3 mm more per year). The implementation of a global atmospheric chemistry model (CAM-Chem) in the Community Atmosphere Model (CAM) enables the connection between the global chemistry model (CAM-Chem) and the regional chemistry model Community Multi-scale Air Quality modeling system (CMAQ). The statistical evaluation demonstrates confidence in the regional chemistry downscaling methodology. In U.S., the mean concentrations of Maximum Daily 8-hr ozone is 3.1 to 9.5 ppbv higher during the heat wave periods than non-heat wave periods in RCP 8.5, stressing the importance of control strategies during the heat wave periods.

TABLE OF CONTENTS

LIST OF TABLES

LIST OF FIGURES

LIST OF ABBREVIATIONS

AE6	Aerosol Scheme 6
AQS	Air Quality System
AR4	Fourth Assessment Report
AR5	Fifth Assessment Report
BCON	boundary condition processor
BEIS	Biogenic Emissions Inventory System
CAM	Community Atmosphere Model
CAM-Chem	Community Atmosphere Model with chemistry
CAPE	Convective Available Potential Energy
CCSM	Community Climate System Model
CESM	Community Earth System Model
CLM	Community Land Model
CMAQ	Community Multi-scale Air Quality modeling system
CMIP5	Coupled Model Intercomparison Project Phase 5
CTM	Chemical Transport Model
ENSO	El Niño Southern Oscillation
ESG	Earth System Grid
GCMs	Global Climate Models
ICON	Initial Condition Processor
IPCC	Intergovernmental Panel on Climate Change
MCIP	Meteorology-Chemistry Interface Processor
MDA8	maximum daily 8-h ozone
MFB	Mean Fractional Bias
MFE	Mean Fractional Error
MNB	Mean Normalized Bias
MNE	Mean Normalized Error
NAAQS	National Ambient Air Quality Standards
NCAR	National Center for Atmospheric Research
NCDC	National Climatic Data Center
NCEP	National Centers for Environmental Prediction
NMB	Normalized Mean Bias
NME	Normalized Mean Error
NMVOCs	Non-methane Volatile organic compounds
OBSGRID	Objective Analysis
PBL	Planetary Boundary Layer
PCM	Parallel Climate Model
PM	Particulate Matter

POP	Parallel Ocean Program
RCMs	Regional Climate Models
RCPs	Representative Concentration Pathways
RH	Relative Humidity
RRTMG	Rapid Radiative Transfer Model for GCMs
SETD	Seasonal Extreme Temperature Duration
SMOKE	Sparse Matrix Operator Kernel Emissions
SOA	Secondary Organic Aerosol
SRES	Special Report on Emissions Scenarios
SST	Sea Surface Temperature
USPEA	United States Environmental Protection Agency
WRF	Weather Research and Forecasting
WPS	WRF Preprocessing System

CHAPTER I

1 DISSERTATION OVERVIEW

1.1 Introduction

Since the Industrial Revolution and especially after the 1800s, global and regional climate patterns have significantly changed, largely a result of increasing anthropogenic greenhouse gas emissions. As climate change continues to unfold in response to increasing greenhouse gases emissions, its effects on sensitive ecosystems and interactions with other disturbances will become more pronounced. Compared with average climate change, extreme weather events exert more impact on ecosystems and could cause both property damage and loss of life in a short time period [*Parmesan and Martens*, 2008; *Parmesan et al.*, 2000]. Extreme weather events have already significantly influenced North America. Lott and Ross [2006] report in nearly every year since 1980, extreme events have caused more than 1 billion dollars in damage in the US; in 2005 the annual loss due to extreme events totaled 100 billion dollars. As one of the primary extreme events, heat waves cause severe and harmful impacts on human health and can kill a large number of people in a short period of time. For instance, several hundred people died in a 1995 Chicago heat wave while more than ten thousand heat-related deaths occurred in a 2003 European heat wave [*Robine et al.*, 2008; *Whitman et al.*, 1997]. Several research studies, including the Intergovernmental Panel on Climate Change (IPCC) Fourth Assessment Report (AR4) [*IPCC*, 2007], have found that temperature and heat wave duration and frequency are more likely to increase in the future as a result of global warming [*Ganguly et al.*, 2009; *IPCC*, 2007; *Meehl and Tebaldi*, 2004; *Schar et al.*, 2004; *Tebaldi et al.*, 2006; *Weisheimer and Palmer*, 2005]. All these simulations were based upon IPCC Special Report on Emissions Scenarios (SRES) [*Nakicenovic and Swart*, 2000]. The newly designed scenarios, denoted by 'representative concentration pathways' (RCPs, [*Moss et al.*, 2010]; http://www.pbl.nl/en/publications/2011/special-issue-rcps-climatic-change), use a parallel approach to combine technology, economy, demography and policy to develop

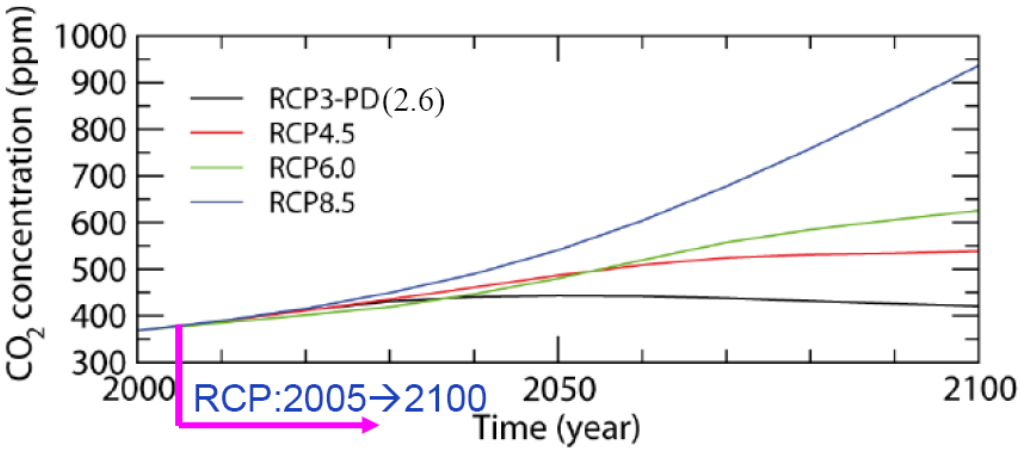

Figure 1.1 CO_2 concentration pathways for the RCP scenarios*

*Source: http://stratus.astr.ucl.ac.be/textbook/pdf/Chapter_6.pdf

plausible CO_2 concentration pathways, shown in Figure 1.1 [*Moss et al.*, 2010; *Riahi et al.*, 2007]. Studies of these scenarios are the central focus of Coupled Model Intercomparison Project Phase 5 (CMIP5) [*Taylor et al.*, 2009; *Taylor et al.*, 2012], and are also the core topic of this research.

During the last few years, global climate models (GCMs) have been further developed and continuously improved. One of the global climate models, Community Earth System Model (CESM), is a state-of-the-art coupled global circulation model, and has now become a true Earth system model through the inclusion of land and ocean biogeochemistry. The effects of CO_2 and nitrogen (N) on plant fertilization and growth are now part of the standard earth system model (CESM1.0, CLM4.0) [*Thornton et al.*, 2009]. In addition, realistic atmospheric chemistry mechanisms were implemented to include chemical reactions involving gases and aerosols that contribute to radiative forcing as well as to air quality parameters such as tropospheric ozone and the sulfur and nitrogen cycles [*Lamarque et al.*, 2010].

Due to limited computational resources, global climate simulations usually use a spatial resolution of a hundred to a few hundred kilometers. Under this spatial scale, it is possible to analyze climate change at a global scale or large regional scale. However, it has become increasingly important to utilize high resolution scale, especially in public

health-related climate studies. There are two primary methods: statistical downscaling and dynamical downscaling. Statistical downscaling demands less computational power but may not accurately reproduce physical relationships between global and regional outputs. Dynamical downscaling methodology is based on fundamental physical theories, so the global and regional models are more transferable. In order to take advantage of better physical relationships and detailed regional topography, the dynamical downscaling technique was used to downscale global climate model outputs and provide the initial and boundary conditions for the regional climate model. This methodology is computationally demanding and requires considerable implementation effort. Thus, a linkage technique which couples global and regional climate models (RCMs) together is necessary. The earliest study to examine differences between GCMs and RCMs is described by *Dickinson et al.* [1989] and used a horizontal resolution of 60 km. As a result, a series of studies on regional climate downscaling were performed with resolutions around 50-60km [*Giorgi*, 1990; *Giorgi et al.*, 1994; *Hostetler et al.*, 1994; *Leung et al.*, 1996; *McGregor and Walsh*, 1994; *Podzun et al.*, 1995]. More recently, finer spatial resolution has been used in studies, with solutions of 30km or less [*Bell et al.*, 2004; *Caldwell et al.*, 2009; *Snyder et al.*, 2002]. In this study, to downscale even finer resolution to a 4 km by 4 km resolution in the eastern US was explored, which may prove extremely valuable for local detailed analysis.

The impact of climate on air quality has achieved wide attention, however, most studies focused on the Intergovernmental Panel on Climate Change (IPCC) Special Report on Emissions Scenarios (SRES) A1 and A2 scenarios [*Nakicenovic and Swart*, 2000]. Bell et al [2007] found by keeping emissions fixed at the present conditions, under A2 climate scenario, an increase of summer daily 1-h maximum ozone was projected from an average of 4.8 pppb, up to 9.6 ppbv, by the 2050s. They also found the mean number of days exceeding the daily maximum 8-h ozone standard increased by 68%. Nolte et al. [2008] found that by the 2050s, an overall increase of 2 to 5 ppbv in maximum daily 8-h ozone in Texas and parts of the eastern U.S. under A1B scenario was to be expected while maintaining emissions at current level.

Compared to SRES scenarios, these new RCP scenarios employ different emissions pathways [*Lamarque et al.*, 2011b], and details are discussed in the Section 6.5.2. Using global chemistry models, the tropospheric ozone is projected to decrease in RCP 2.6, RCP 4.5 and RCP 6.0 [*Lamarque et al.*, 2011b], and increase in RCP 8.5 by the end of 21st century [*Kawase et al.*, 2011; *Lamarque et al.*, 2011b]. The regional scale studies on the RCP scenarios are very limited, thus, to investigate more detailed local impact from climate on air quality in these new RCP scenarios, in this study, dynamical downscaling was applied using a regional chemistry model, and a high resolution, 12 km by 12 km, continental U.S. domain, designed for the regional simulations.

1.2 Research Goals

The goals of this study are: (1) to determine how and to what extent heat waves will occur under changing climate and will lead to air quality perturbations in global scales; (2) to downscale global climate to regional climate for investigating local detailed extreme weather events at present and future climate conditions; (3) to downscale global chemistry modeling to regional scale in order to evaluate the impact of climate change , particularly extreme weather events, on regional air quality.

1.3 Applications of the Study

1. The three hourly global climate outputs (RCP 4.5 and RCP 8.5) have been published in the Earth System Grid (ESG, http://esg2-gw.ccs.ornl.gov/), and are available for use by the research community.
2. Regional downscaling and analysis of extreme events can provide important information for policy makers to take action in protecting ecosystems.
3. This is the first time regional downscaling has been used in such a high resolution domain (4 km by 4 km, eastern US), and the outputs can be widely used by other groups interested in regional-scale climate and chemistry.

a. The high resolution climate data can be used to generate local predictions of Lyme disease and lung cancer, currently the subject of work at Harvard University, Emory Universities and University of Michigan.

b. The high resolution climate output from WRF-CMAQ can be used as input to the biogeochemical model (i.e, PnET-BGC Model) and the hydrologic model, (i.e., Variable Infiltration Capacity Model), to investigate hydrology and water quality response to changes in climate in US. The data can be used to help analyze the effects of heat waves and drought and may also help evaluate ecosystems which are susceptible to extreme climate events.

c. The regional downscaling outputs are easily applied to national park studies. It can be used to quantify the potential impact of climate change, such as ozone and nitrogen depositions, on the national parks, such as the Appalachian Highlands Network, including the Great Smoky Mountains National Park, the Blue Ridge Parkway, Big South Fork Wild and Scenic River and Obed Wild and Scenic River.

d. The data can be used for impact assessment in terms of different regional vulnerabilities. The climate change studies can also provide a basis for policy makers when taking actions on climate mitigation and adaptation.

e. The downscaling methodology developed in this study is applicable to other global climate and chemistry models.

CHAPTER II

2 METHODOLOGY

2.1 Overview of the Methodology

This study requires climate and chemistry simulations at both global and regional scales, shown in Figure 2.1. For global simulations, the study includes present climate and chemistry simulations, and future climate and chemistry simulations under different projected emissions scenarios. With regards to regional downscaling simulations, due to limited computational resources, a four year period (2001-2004) was selected as base case (present) and 3 year period was selected as future case (2057-2059) in both the regional climate and chemistry studies.

2.2 Climate/Air Quality Model Description

2.2.1 Global Climate Model Description

CESM version 1.0 (http://www.cesm.ucar.edu/models/cesm1.0/) was used for global climate simulations. CESM, composed of atmosphere, ocean, land surface, sea-ice, and a coupler, is a state-of-the-art global climate model. The atmospheric component, Community Atmosphere Model (CAM 4.0), uses the finite-volume (FV) dynamical core [*Neale et al.*, 2010]; the land component, Community Land Model (CLM 4.0), incorporates fertilization effects on plant growth by CO_2 and nitrogen (N) [*Thornton et al.*, 2009]. Improvements in CAM 4.0 over the CAM 3.0 to the physical parameterization of tropical deep convection, planetary boundary layers and aerosols have led to better simulation of regional temperatures and precipitation [*Gent et al.*, 2010] as well as improved performance over seasonal and inter-annual times scales. A horizontal resolution of 0.9 by 1.25 degree was used for the global climate simulations. The model has 26 vertical layers and the top layer has a pressure of 2.917 mb, which is about 40 km high and well into the stratosphere.

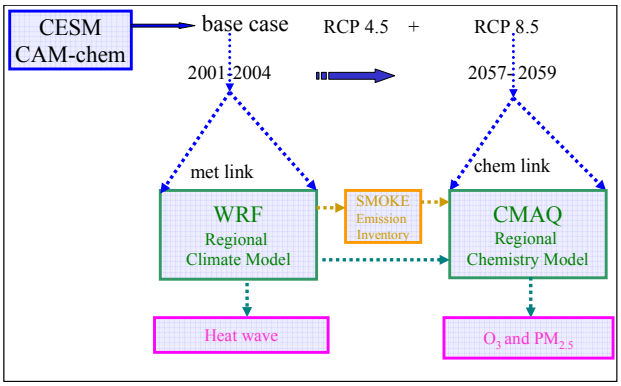

Figure 2.1 Downscaling linkage from global model (CESM and CAM-Chem) to regional climate and chemistry model (WRF and CMAQ)

2.2.2 Global Chemistry Model: CAM-Chem

The atmospheric chemistry has been fully integrated in CESM, referred to as CAM-Chem and discussed by Lamarque et al. [2012]. CAM-Chem was integrated within a fully coupled Earth System model CESM. In addition to the atmospheric component, CESM includes the land and ocean components, and these components enable the chemistry module to take consideration of biogeochemical processes among the atmosphere, land and ocean [Lamarque et al. 2012]. The heat waves (and thermal properties of the solution) are resulted from the standard model configuration where the radiation ozone interaction is prescribed as specified by CMIP5. The major consideration is to keep climate the same as the pure RCP climate scenarios. If chemistry was coupled to the radiation, the climate from CAM-Chem will be different from the RCP scenarios, which deviates from the purpose of this study. Using prescribed aerosols can keep true RCP scenarios and achieve validated climate. CAM-Chem has been widely used and evaluated on its representation in the atmosphere [*Aghedo et al.*, 2011; *Lamarque and Solomon*, 2010; *Lamarque et al.*, 2011a; *Lamarque et al.*, 2011b; *Lamarque et al.*, 2012]. The same resolution as CAM4, CAM-Chem was run on a 0.9 by 1.25 degree (latitude by longitude) spatial resolution with 26 vertical layers.

2.2.3 Regional Climate Model WRF Description

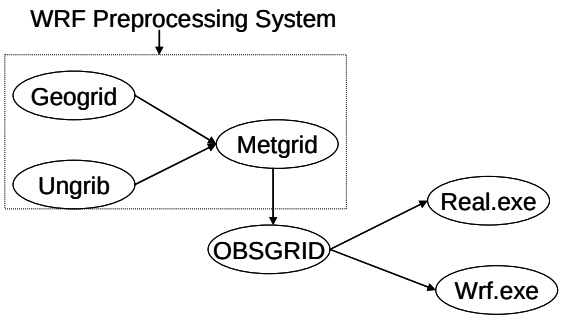

Figure 2.2 WRF system flow chart*

*(based on http://www.mmm.ucar.edu/wrf/users/docs/user_guide_V3/users_guide_chap3.htm)

The Advanced Research Weather Research and Forecasting (WRF) Model version 3.2.1 [*Skamarock and Klemp*, 2008], is a state-of-the-science regional meteorological model. The model contains 34 vertical layers, ranging from the surface to 50 mb (about 20 km). The numerical equations are fully compressible and non-hydrostatic [Wong et al., 2012].

WRF System contains three main components, shown in Figure 2.2, including WRF Preprocessing System (WPS), Objective Analysis (OBSGRID), and WRF simulations. WRF simulations include the initial and boundary simulations (real.exe) and WRF physical simulations (wrf.exe).

2.2.3.1 The WRF Preprocessing System (WPS)

The WRF Preprocessing System (WPS) is composed of three programs (Geogrid, Ungrib and Metgrid,), which are used to prepare inputs for initial and boundary conditions. The descriptions of these three programs are based on the following website (http://www.mmm.ucar.edu/wrf/users/docs/user_guide_V3/users_guide_chap3.htm).

Geogrid is used to define the simulation domains while interpolating static geographical data to the model grids. The static geographic data includes grid based latitude, longitudes, terrain height, etc.

The purpose of Ungrib is to extract meteorological fields from global reanalysis GRIB-formatted data. It is mainly used to reformat the reanalysis data to the format that Metgrid accepts.

After running Geogrid and Ungrib, Metgrid is used to horizontally interpolates all the meteorological fields from Ungrib to the specific model simulation domains defined by the program of Geogrid.

2.2.3.2 Objective Analysis (OBSGRID)

Objective analysis attempts to improve meteorological analyses by incorporating observational information to the modeling domains (http://www.mmm.ucar.edu/wrf/users/docs/user_guide_V3/users_guide_chap7.htm). The observational information may include real observations from National Centers for Environmental Prediction/National Center for Atmospheric Research (NCEP/NCAR) reanalysis data or global climate data for climate downscaling.

2.2.3.3 WRF initial/boundary conditions and WRF simulations

As shown in Figure 2.2, the program real.exe is used to prepare initial and boundary conditions for WRF simulations based upon OBSGRID outputs, while wrf.exe is used for WRF simulations. While WRF simulations involve many different physics options, optimized physics options were used in this study for U.S. climate simulations. The main physical options are: Single-Moment 6-class microphysical scheme (WSM6) [*Hong and Lim*, 2006]; the new Kain-Fritsch convective parameterization [*Kain*, 2004]; Rapid Radiative Transfer Model for GCMs (RRTMG) [*Iacono et al.*, 2008; *Morcrette et al.*, 2008]; the Mellor-Yamada-Janjic planetary boundary layer (PBL) scheme [*Janjić*, 1990; *Mellor and Yamada*, 1982]; and the Noah land surface model [*Chen and Dudhia*, 2001].

2.2.4 Regional Chemistry model Community Multi-scale Air Quality (CMAQ)

The United States Environmental Protection Agency (USEPA) has employed tremendous resources for developing the regional air quality modeling system CMAQ [*Byun and Ching*, 1999; *Byun and Schere*, 2006]. It was first released in July 1998 and has been updated several times. The newest version, CMAQ 5.0 [*Wong et al.*, 2012] is a fully integrated regional atmospheric chemistry model.

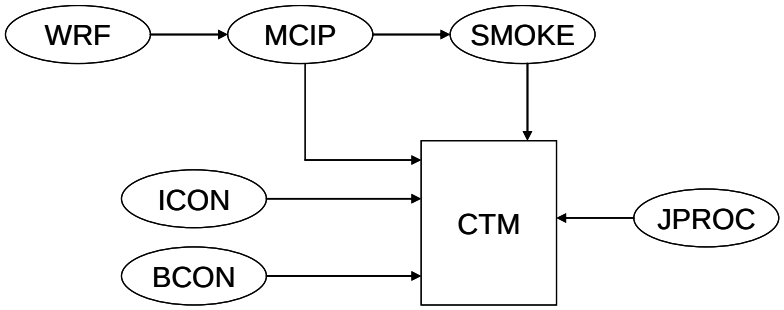

Figure 2.3 CMAQ System diagram

The CMAQ regional air quality modeling system, shown in Figure 2.3, includes six main components: Meteorology-Chemistry Interface Processor (MCIP), emissions generation model Sparse Matrix Operator Kernel Emissions (SMOKE), initial condition processor (ICON), boundary condition processor (BCON), photolysis rates processor (JPROC), and Chemical Transport Model (CTM). The six components were described as follows (based on http://ie.unc.edu/cempd/products/cmaq/op_guidance_4.6/html/ and USERS GUIDE at http://www.cmascenter.org/help/documentation.cfm?MODEL=cmaq&VERSION=5.0).

2.2.4.1 Meteorology-Chemistry Interface Processor (MCIP)

As previously described, WRF is used to prepare meteorological fields for regional chemical model CMAQ; however, CMAQ cannot directly accept WRF outputs. MCIP, an interface which converts WRF outputs format to CMAQ input format, also extracts necessary information for CMAQ. In this process, only the variables used in CMAQ are extracted from WRF, which saves data storage and is efficient in data Input/Output (I/O).

2.2.4.2 Sparse Matrix Operator Kernel Emissions (SMOKE)

SMOKE (http://www.smoke-model.org/index.cfm) is used to process both anthropogenic emissions from the National Emissions Inventory (NEI) and biogenic emissions. Typically, emission inventories from different emission sources are on an annual or daily basis. However, emission data on an hourly basis are required by air quality models. SMOKE is the interface which converts annual or daily emission inventory to hourly emissions on each modeling grid.

2.2.4.3 Initial and Boundary Conditions Processor (ICON and BCON)

ICON and BCON were used to provide initial and boundary conditions, respectively, for air quality simulations. ICON generates chemical species concentrations at the first time step of a simulation period, while BCON provides chemical species at the lateral boundaries for the entire simulation period. By default, the ICON and BCON will generate time-independent background profiles for chemical species. However, the time-independent boundary conditions do not represent diurnal trends, and it may not be acceptable in some real applications. In order to more accurately represent real conditions, downscaling of boundary conditions from a global model on a 3-hour basis is used; more discussion of this downscaling follows.

2.2.4.4 Photolysis Rates Processor (JPROC)

Photolysis Rates Processor (JPROC) is used to calculate the photolysis rates reference table, and then further interpolated to modeling grids during a certain modeling periods.

2.2.4.5 Chemical Transport Model (CTM)

Chemical Transport Model (CTM), the core component of CMAQ, integrates the output from the preprocessors described above (ICON, BCON, JPROC, MCIP and SMOKE), to simulate the atmospheric chemistry and physics processes. The modeled outputs are typically hourly gridded concentrations with different species on multiple vertical layers. The 3-D gridded data outputs typically contain O_3, NO, NO_2, $PM_{2.5}$ species and depositions.

2.3 Dynamical Downscaling from Global to Regional Scales Climate and Chemistry

Dynamical Downscaling is a technique used to link between global and regional models. In the downscaling process, the global model provides the initial and boundary conditions for the regional model. Initial conditions are needed only for the first time step while the boundary conditions have to be 3 to 6 hourly (3-hour in this study) in order to represent diurnal patterns.

2.3.1 Climate Downscaling from CESM to WRF

The dynamical downscale from CESM to WRF includes the downscaling from CESM to WRF Preprocessor System (WPS) and from CESM to Objective Analysis (OBSGRID). In retrospective studies, NCEP/NCAR Reanalysis data is used to provide meteorological fields and drive regional model WRF. In climate studies, global climate model outputs are needed to drive WRF. In WPS, one of the three programs is Ungrib, shown in Figure 2.2. Since the format from global model output is different from NCEP data, a program with similar functions to Ungrib needs to be implemented. Since variable names in CESM and WPS are different, variable matching from CESM to WPS when downscaling is a necessary first step. Table 2.1 lists all the required variables for downscaling from CESM to WRF. Note that for soil moisture and soil temperature, and there are 15 layers in CESM while WPS requires only 4 layers in its Noah Land Surface Model (Noah LSM). Linear interpolation from CESM to WPS was conducted for the soil moisture and soil temperature, but the lack of exact layer matching may lead to some discrepancies.

Table 2.1 Variable matching from CESM to WRF*

CESM 1.0	WRF	Variable Description
PS	PSFC	2d Surface Pressure
PSL	PMSL	2d Mean Sea Level Pressure
LANDFRAC	LANDSEA	2d Land Fraction
TS	SKINTEMP	2d Skin Temperature
TREFHT	TT	2d 2m Temperature
U (First layer)	UU	2d 10m Zonal Wind U
V (First layer)	VV	2d 10m Zonal Wind V
RELHUM	RH	2d 2m Relative Humidity
T	TT	3d Temperature
RELHUM	RH	3d Relative Humidity
U	UU	3d Zonal Wind U
V	VV	3d Zonal Wind V
Z3	GHT	3d Geopotential Height
H2OSOI	SM000010/SM010040/SM040100/SM100200	Soil Moisture
TSOI	ST000010/ ST010040/ST040100/ST100200	Soil Temperature

***** The descriptions of variables are from the CESM and WPS outputs

2.3.1.1 Integrity Comparison between CESM and WPS Outputs

The outputs from CESM and WPS should show similar patterns. All variables were checked for congruency, but only wind vector distributions are shown in Figure 2.4. Similar patterns have been observed through the wind vector comparison between CESM and WPS in three simulation domains (36 km—D1, 12 km—D2 and 4 km—D3). Other variables show similar patterns between CESM and WPS, but there are some exceptions in skin temperature, as discussed below.

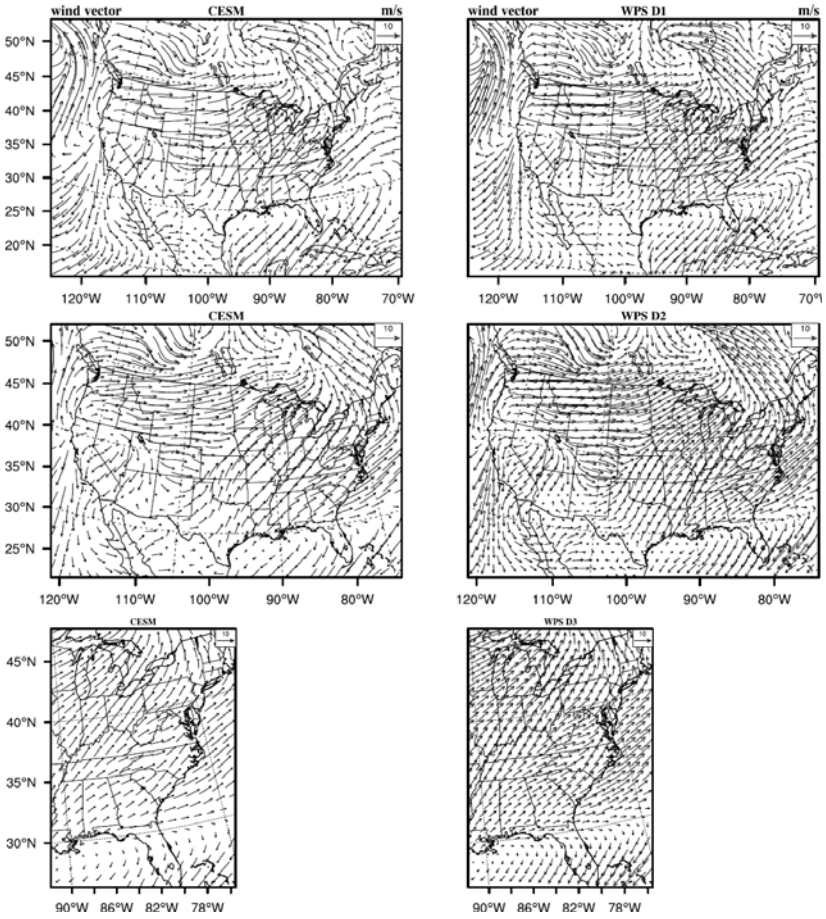

Figure 2.4 Wind vectors comparison: The left figure comes from CESM while the right figure comes from Metgrid (WPS)

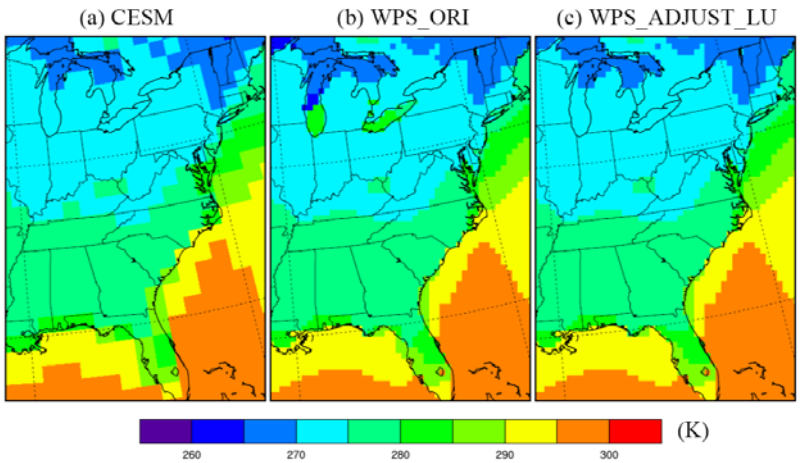

Figure 2.5 Skin temperature comparisons: (a) CESM; (b) WPS output without changing land use type; (c) WPS output after modifying the land/sea mask

Figure 2.5 (a) and (b) shows the spatial distribution between CESM and WPS outputs for the D3 (4 km by 4 km domain), and the other two domains show similar patterns. Significant differences show up near Great Lakes region. While the same methodology is applied for other variables (such as temperature and wind vector), it does not work well for skin temperature (surface temperature). As is reported by *Gao et al.* [2012], in the atmospheric component, CAM, the land use type for the land and lake is the same. When downscaled, land use becomes important for interpolating skin temperature in regional models. When Metgrid horizontally interpolates skin temperature from CESM, for typical variables, the nearest 16 grids are used in distance-weighted interpolation. For skin temperature, however, it is based upon the land/sea mask in land use, so interpolation of skin temperature uses the nearest sea surface temperature. In the Great Lakes region, the land use type is land, so interpolation occurs using the nearest sea surface temperature to the right side, thus leading to somewhat unexpected interpolation. To resolve this problem, the land use type in the Great Lakes region was modified to the same as the ocean land use type. After the modification, the new spatial pattern of WPS outputs is shown in Figure 2.5 (c), which is consistent with CESM (Figure 2.5 (a)).

2.3.1.2 Vertical Interpolation

The vertical coordinate of CAM, is a hybrid sigma-pressure system [*Neale et al.*, 2010]. In the system, higher vertical levels are assigned pure pressure; lower vertical levels are assigned hybrid sigma-pressure and the lowest levels, pure sigma, as is shown

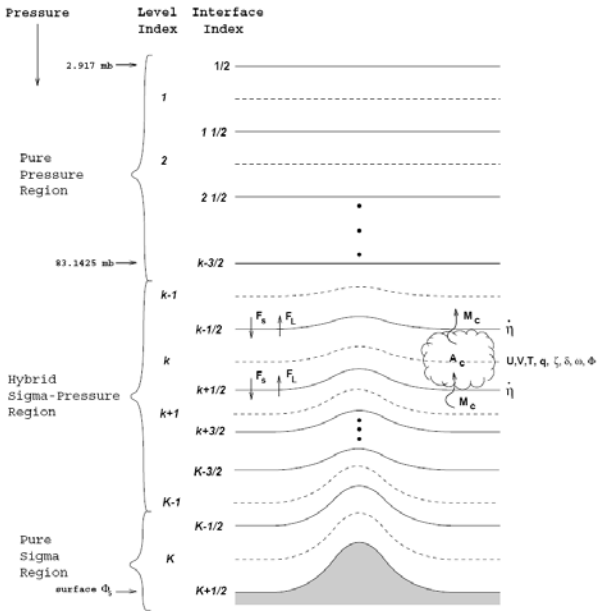

Figure 2.6 Hybrid vertical structure of CAM 4.0 (Source: [*Neale et al.*, 2010])

in Figure 2.6. The vertical layers are typically divided into two categories, full model levels and half model levels. Most of the variables such as zonal wind U, zonal wind V, temperature T, specific humidity q and relative humidity *RH* are defined at the full model levels while surface geopotential is defined at half levels (surface level).

The relationship between pressure and hybrid coordinate in each grid can be expressed in Equation 2.1, and more details are discussed in Neale et al. [2010]. Furthermore, in higher layers (top 7 layers), B_v is 0, which makes the vertical coordinate pure pressure. The lowest layer has A_v of 0, making it pure sigma. Other layers have hybrid pressure-sigma coordinate.

$$p(r,c,v) = A_v P_0 + B_v P_s(r,c) \qquad \text{Equation 2.1}$$

Where p represents the pressure for a certain grid point at a given vertical layer. The index notation of r, c and v represent a specific row, column and vertical layer. The coefficients A_v and B_v are hybrid coefficients at layer midpoints or interfaces. P_0 denotes constant reference pressure, with the value of 100,000 Pa. Ps(r,c) denotes surface pressure at a certain grid point.

The CESM output is in hybrid-pressure coordinate, while Metgrid requires data in pure pressure levels. Thus, interpolation from hybrid-pressure coordinate to pressure coordinate becomes necessary. There are a few conditions that need to be considered.

(a) If the WPS pressure level is between the pressure in layer z_0 and z_1 ($1 \le z_0, z_1 \le 26$) in CAM4, then linear interpolation is used.

$$f(z) = f(z_0) + \frac{f(z_1) - f(z_0)}{p_{z_1} - p_{z_0}} \times (p_z - p_{z_0}) \qquad \text{Equation 2.2}$$

p_{z_0}, f_{z_0} and p_{z1}, f_{z1}: the pressure and certain variable values at layer z_0 and z_1 in CAM4

p_z, f_z: the pressure and certain variable values at layer z in WPS

(b) If the pressure level in WPS is lower than the top layer pressure in CAM4, the variables value is simply equal to the top layer values in CAM4.

(c) If the pressure level in WPS is higher than the pressure in the bottom layer of CAM4, there are two conditions. For variables other than geopotential height and temperature, the variable values in WPS are set to equal the bottom layer values in CAM4. For geopotential height and temperature, Trenberth et al. [1993] found the following interpolation methods more appropriate than assigning the bottom layer values, and these equations were applied to the dynamical downscaling.

$$\Phi = \Phi_s - R_d \times T^* \times \ln\frac{p}{p_s}[1 + \frac{1}{2} \times \alpha \times \ln\frac{p}{p_s} + \frac{1}{6} \times (\alpha \times \ln\frac{p}{p_s})^2] \qquad \text{Equation 2.3}$$

$$T = T^* \times (1 + \alpha \times \ln\frac{p}{p_s} + \frac{1}{2} \times (\alpha \times \ln\frac{p}{p_s})^2 + \frac{1}{6} \times (\alpha \times \ln\frac{p}{p_s})^3] \qquad \text{Equation 2.4}$$

Φ: geopotential

Φ_s: surface geopotential in CESM

R_d: gas constant dry air, 287.04 J Kg^{-1} K^{-1},

$\alpha = L_r \times \frac{R_d}{g}$, unitless, where L_r: constant lapse rate, 0.0065 K/m; R_d: gas constant dry air, 287.04 J Kg^{-1} K^{-1}, g: acceleration due to gravity, 9.80616 m/s^2

p : Pressure in WPS

p_s : Surface pressure in CAM4

T^*: Surface temperature, equals to $T_{BOT}(1+\alpha \times \frac{P_s - P_{BOT}}{P_{BOT}})$ where T_{BOT} : Temperature in the bottom layer of CAM4

2.3.1.3 Interpolation of Soil Moisture

The land component CLM4, contains 15 soil layers, with layer depths of 0.71, 2.79, 6.23, 11.89, 21.22, 36.61, 61.98, 103.80, 172.76, 286.46, 473.92, 782.98, 1292.53, 2132.65, 3517.76 cm (based on CLM4 outputs). In contrast, the soil layer heights in WPS are 10, 40, 100, 200 cm. To estimate the soil temperature of each layer in WPS, the mid-layer temperature is used. For example, the first layer (0 to 10 cm) is represented by the temperature at a depth of 5 cm. Linear interpolation was applied to derive temperatures for WPS, as shown in Equation 2.2. For soil moisture, the unit is mm^3 water per mm^3 soil. The interpolation is shown in the Equation 2.5 and Equation 2.6.

$$f(h_{0\_1}) = \frac{f(k)\times(h_k - h_0) + f(k+1)\times(h_{k+1} - h_0) + ... + f(n)\times(h_1 - h_{n-1})}{h_1 - h_0} \quad \text{Equation 2.5}$$

$f(h_{0\_1})$: Soil moisture in WPS, the 0 and 1 means the low and high height point in one layer

$f(k,...,n)$: Soil moisture in layer k to n in CLM4

$$SM = \frac{f(k)\times(h_k - h_0)}{h_k - h_{k-1}} + f(k+1)\times(h_{k+1} - h_0) + ... + \frac{f(n)\times(h_1 - h_{n-1})}{h_n - h_{n-1}} \quad \text{Equation 2.6}$$

h_0 and h_1 are the low and high height of a certain layer in WPS

2.3.2 Chemistry Downscaling from CAM-Chem to CMAQ

The main purpose of the dynamical downscaling from CAM-Chem to CMAQ is to provide initial and boundary conditions for CMAQ. Initial conditions are needed only for the start of the simulation while boundary conditions require dynamical downscaling from CAM-Chem. Similar to the downscaling from CESM to WRF, the first step in

chemistry downscaling is to match variables in CAM-Chem and CMAQ. Table 2.2 lists the variable matching from CAM-Chem to CMAQ, which is based upon the previous work [*Emmons et al.*, 2010; *Yarwood et al.*, 2005]. The other steps were discussed below.

Table 2.2 Mapping table between CAM-Chem and CMAQ*

CAM-Chem species	**Species Name**	**CMAQ CB05 species**
The unit for gas: mol/mol		ppmv
O3	Ozone	O3
NO	Nitric oxide	NO
NO2	Nitrogen dioxide	NO2
NO3	Nitrate radical	NO3
HNO3	Nitric Acid	HNO3
HO2NO2	peroxynitric acid	PNA
N2O5	Dinitrogen pentoxide	N2O5
OH	Hydroxyl radical	OH
HO2	Hydroperoxyl radical	HO2
H2O2	Hydrogen Peroxide	H2O2
CO	Carbon monoxide	CO
CH3OOH	Methyl hydroperoxide	MEPX
CH2O	Formaldehyde	FORM
C2H4	Ethene	ETH
CH3CHO	Acetaldehyde	ALD2
C2O3	Acetylperoxy radical	C2O3
PAN	Peroxyacetyl nitrate	PAN
CH3COCHO	Methylglyoxal and other aromatic products	MGLY
ROOH	Higher organic peroxide	ROOH
ONIT	Organic nitrate	NTR
ISOP	Isoprene	ISOP
PAR	Paraffin carbon bond (C-C)	PAR
OLE	Terminal olefin carbon bond (R-C=C)	OLE
TOLUENE	Toluene and other monoalkyl aromatics	TOL
SO2	Sulfur dioxide	SO2
C10H16	Terpene	TERP
NH3	Ammonia	NH3
CH4	Methane	CH4
XO2	NO to NO2 conversion from alkylperoxy (RO2) radical	XO2

XO2N	NO to organic nitrate conversion from alkylperoxy (RO2) radical	XO2N
ROR	Secondary alkoxy radical	ROR
CL2	Chlorine gas	CL2
HOCL	Hypochlorous acid	HOCL
HCL	Hydrogen chloride	HCL
Unit for particle (kg/kg)		CMAQ AE6 species
SO4	Sulfate	ASO4J
NH4NO3	Ammonium nitrate	ANH4J+ANO3J
CB1+CB2	black carbon, hydrophobic+ hydrophillic	AECJ
OC1+OC2	organic carbon, hydrophobic+hydrophillic	APOCJ
SSLT1+SSLT2	sea salt, 0.1–0.5 μm, 0.5–1.5 μm	ANAJ/ACLJ
SSLT3+SSLT4	sea salt, 1.5–5 μm,5–10 μm	ANAK/ACLK

* The sources of the table are from Emmons et al. [2010] and Yarwood et al. [2005].

2.3.2.1 Vertical Interpolation Algorithm

Since CAM-Chem output units are mass-based and similar to that of soil moisture, the interpolation methods between soil moisture and CAM-Chem outputs are similar, and it is listed below:

$$f(h_i) = \frac{\frac{f(k)\times(h_{i-1}-h_{k-1})}{h_k - h_{k-1}} + f(k+1)\times(h_{k+1}-h_k) + \ldots + \frac{f(n)\times(h_i - h_{n-1})}{h_n - h_{n-1}}}{h_{i+1} - h_i} \quad \text{Equation 2.7}$$

h_i denotes the top height of a layer in CMAQ, while h_{i-1} denotes the bottom height of a layer in CMAQ;

h_k denotes the starting layer in CESM with the height higher than the bottom height of the layer i in CMAQ, h_{k-1} denotes the bottom height of the layer k in CESM, $h_{k+1,\ldots,n-2}$ denotes the layers of CESM within the layer i in CMAQ and , h_{n-1} denotes the layer of CESM with the height higher than the top height of the layer i in CMAQ.

CHAPTER III

3 OPTIMIZATION OF COMPUTATIONAL EFFICIENCY

3.1 Overview of the Methodology

This study requires a large amount of service units (CPU hours) and storage. Since large simulations are involved, optimization of computational resources becomes extremely important. In the following descriptions, the term "processor" will be used to represent "core" on Kraken, and Kraken has 12 cores per node.

3.2 Optimization of Global and Regional Simulations

In order to select the optimal processor arrangement, a series of sensitivity tests have been conducted.

From the computational tests, the most efficient run for CESM uses 864 processors. For WRF, the most efficient and acceptable processor number selections for 36 km, 12 km and 4 km WRF simulation domains are 24, 84 and 120, respectively. For CMAQ runs, the most efficient and acceptable processor numbers are 48 for 12 km domain. Figure 3.1 visually summarizes the CESM/WRF-CMAQ run requirements. The total service units are also calculated for all the simulations shown in Table 3.1. The total service units used in this study were 5.0 million.

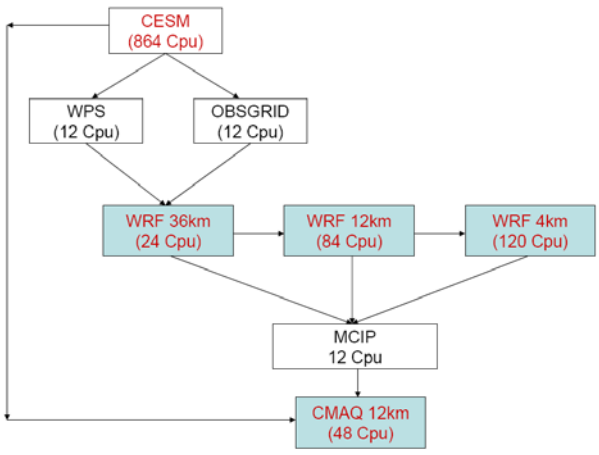

Figure 3.1 Flow chart of CESM downscaling to WRF/CMAQ

Table 3.1 Service Units required for all the simulations

	Processor Numbers	Service Units (Hours)
CESM	864	1,600,928
WPS	12	10,424
OBSGRID	12	24,528
36km WRF	24	47,654
12km WRF	84	457,856
4km WRF	120	1,815,072
MCIP	12	17,554
12km CMAQ	48	930,636
Total		4,904,652

A large amount of outputs has been generated from the simulations. The size for both base case and future case CESM/WRF-CMAQ outputs is about 300 Terabytes. All the data have been archived in the High Performance Storage System (HPSS), in Kraken and Jaguar, respectively, for further analysis and studies.

CHAPTER IV

4 THE INCREASES IN HEAT WAVE AND SEASONAL EXTREME TEMPERATURES IN THE 21ST CENTURY CLIMATE

4.1 Declaration

This chapter is slightly revised based on a manuscript, to be submitted to a journal for publication.

4.2 Abstract

This study examines past and projected extreme temperature events across the planet. A fully coupled earth system model is evaluated but the methodology can be used for a variety of models to assess their ability to simulate extremes in a changing climate. Simulation statistics compare favorably with NCEP observation results during 1948-2005 for 22 regions of the earth including five regions in North America. The Community Earth System Model (CESM 1.0) with the protocols defined in the Coupled Model Intercomparision Project (CMIP5) is used to evaluate the past (1850-2005) and projected forcing of the Representative Concentration Pathways (RCP) 2.6, 4.5, 6.0 and 8.5 (2005-2100) climate scenarios. The global bias for heat wave intensity (-0.1 ºC ± 0.1 ºC), heat wave duration (0.1 days ± 0.2 days) and frequency (0.1 event/year ± 0.1 event/year) validates the use of climate models to simulate regional temperature extremes. More significant heat wave intensity, duration and frequency were found in the projections than earlier SRES A1FI findings with the previous models. It was found that the heat wave intensity increases significantly across high latitude land areas in the northern hemisphere by the end of 21st century in RCP 8.5. This increase reaches 6.8 ºC ± 1.0 ºC in Alaska, 5.8 ºC ± 0.8 ºC in Greenland, 5.3 ºC ± 1.3 ºC in Northern Europe and 6.9 ºC ± 0.5 ºC in North Asia. By the end of the century, the mean duration days across 22 regions range from 1.5 to 3.7 times as high as the period from 1948 to 2005. Large increases in the number of heat wave events occur near tropical areas and in the southern hemisphere, resulting from much narrower seasonal variations of daily maximum temperature in these regions compared to northern regions. In addition to summer heat waves, the seasonal

extreme temperature duration (SETD) is also analyzed. In RCP 8.5 for the Northern Hemisphere, the largest SETD percentage increase occurs in the winter season, indicating significant temperature increase in winter time.

4.3 Introduction

Heat waves are responsible for adverse impacts on human health and have the potential to harm a large number of people in a short period of time. For instance, over seven hundred people died as a result of the week-long 1995 Chicago heat wave, and more than ten thousand heat-related deaths occurred in the 2003 European heat wave [*Robine et al.*, 2008; *Whitman et al.*, 1997]. The conditions responsible for these impacts include daily maximum temperatures, duration of high temperatures and high night-time minimum temperatures over the period.

Three key parameters characterize heat waves: heat wave intensity, heat wave duration and heat wave frequency. Heat wave intensity is associated with the severity of the heat wave and is defined as the highest three night minimum temperatures [*Karl and Knight*, 1997]. To investigate heat wave duration and frequency, a heat wave is usually defined as the longest continuous period during which: 1) the maximum daily temperature reached a threshold value of T1 for at least 3 continuous days, and 2) the mean daily maximum temperature remained above T1 while the daily maximum temperature reached a secondary threshold, T2 each day [*Huth et al.*, 2000; *Meehl and Tebaldi*, 2004, *Gao et al.*, 2012]. In this study, following Huth et al. (2000) and Meehl and Tebaldi (2004), T1 and T2 are assumed to have either the fixed values of 30º C and 25 ºC, or are set to local 97.5th and 81st percentiles for temperature over a given period [*Huth et al.*, 2000; *Meehl and Tebaldi*, 2004]. These specific thresholds were selected in order to compare with previous studies. With the thresholds as percentage values of T1 and T2, heat waves are relative to a local climatology, while with fixed temperature values, heat waves are not. Using T1 and T2 as fixed values would not be appropriate for the study of the characteristics of heat wave events globally [*Huth et al.*, 2000], so the 97.5^{th} and 81^{st} percentile of present-day climate (1961-1990) were used as the thresholds (T1 and T2) for both present and future heat wave evaluation. Each grid point was

calculated separately to retrieve the two thresholds (T1 and T2). After finding all heat waves in a year, the heat wave duration was calculated as the total heat wave days divided by the number of heat waves, and the heat wave frequency was calculated as the number of heat waves per year. Heat waves most often occur in the summer, but changes also occur during other seasons. Hansen et al. [2012] have reported dramatic changes in global seasonal mean temperature patterns. Thus, the heat wave analysis was complemented with the examination of Seasonal Extreme Temperature Duration (SETD) on a regional basis.

Several research studies, including the IPCC AR4 [*IPCC*, 2007], have indicated a high probability that heat wave duration and frequency will increase in the future as a result of increasing levels of carbon dioxide and other heat-trapping gases and particles in the atmosphere [*Ganguly et al.*, 2009; *Meehl and Tebaldi*, 2004; *Schar et al.*, 2004; *Tebaldi et al.*, 2006; *Weisheimer and Palmer*, 2005]. The AR4 simulations, based upon IPCC Special Report on Emissions Scenarios (SRES) [*Nakicenovic and Swart*, 2000], are now superseded by newly designed scenarios for the Fifth Assessment Report (AR5), called 'representative concentration pathway' scenarios* (RCPs [*Moss et al.*, 2010]). These new scenarios use a parallel approach to combine technology, economy, demography and policy for a plausible time-series of atmospheric emissions and resulting concentration in these gases and particles from 2005 to 2100 [*Moss et al.*, 2010; *Riahi et al.*, 2007]. Studies of these scenarios, in addition to past climate (1850-2005) validations, are the central focus of the Coupled Model Intercomparison Project Phase 5 (CMIP5 [*Taylor et al.*, 2009; *Taylor et al.*, 2012]). While not all CMIP5 model outputs are available, as one of the major contributors, the Community Climate System Model version 4 (CCSM4) was selected in this study, and the methodologies in this study can be easily applied to all other CMIP5 models in future.

As a preliminary evaluation of the model's ability to reproduce the climate extremes of temperature, the observational record is compared with simulation results over the

*http://www.iiasa.ac.at/web-apps/tnt/RcpDb/dsd?Action=htmlpage&page=about

period from 1948 to 2005. Following the model evaluation, possible futures are explored by analyzing the characteristics of heat waves under all four new RCP scenarios (RCP 2.6, RCP 4.5, RCP 6.0 and RC P8.5). Regional analysis of extremes is targeted by dividing the globe into 22 regions. The last objective is to assess the coherence of probability functions of extreme heat waves from an ensemble of simulations.

4.4 Model Descriptions and Experiment Design

The Community Earth System Model (CESM1.0, http://www.cesm.ucar.edu/models/cesm1.0/) is made available for climate research by the National Center for Atmospheric Research under sponsorship from the National Science Foundation and the U.S. Department of Energy. One of the subset configurations of this model was referred to as the Community Climate System model (CCSM4). For the CMIP5 [*Taylor et al.*, 2009; *Taylor et al.*, 2012], a series of global climate simulation experiments were designed with the CCSM4 [*Meehl et al.*, 2011]. CCSM4 is composed of four major components, including atmosphere, ocean, land surface and sea-ice. The atmospheric component, Community Atmosphere Model version 4 (CAM4.0), uses the finite-volume (FV) dynamical core [*Neale et al.*, 2010] with a horizontal resolution of 0.9 by 1.25 degree (latitude/longitude) and with 26 vertical layers. The previous version had a horizontal resolution of about 2 degrees; however, by using 0.9 by 1.25 degree resolution, significant errors in Sea Surface Temperature (SST) were reduced in the major upwelling regions and mid-latitudes in the southern hemisphere [*Gent et al.*, 2011]. The reduced error is due to more properly locating of stronger upwelling favorable winds [*Gent et al.*, 2010] as a result of the better representation of topography. In CAM4, substantial improvement of El Niño–Southern Oscillation (ENSO) was achieved by including sub-grid scale convective momentum transport and a dilution approximation for the calculation of convective available potential energy (CAPE) in the deep convection [*Neale et al.*, 2008, *Gao et al.*, 2012]. The Community Land Model used in Parallel climate model (PCM) was the one-dimensional Land Surface Model (LSM) [*Bonan*, 1996], while the Community Land Model (CLM3) [*Dickinson et al.*, 2006; *Lawrence et al.*, 2007] and CLM4 [*Oleson*, 2010] were used in CCSM3 and CCSM4,

respectively. Compared to LSM, high surface temperature bias in semi-arid regions and 2-m air temperature bias have been reduced in CLM3 [*Oleson*, 2010]. In comparison to CLM3, the most significant improvement in CLM4 is the inclusion of a carbon-nitrogen (CN) cycle model, in which carbon, nitrogen and vegetation phenology is prognostic [*Thornton et al.*, 2007; *Thornton et al.*, 2009]. Lawrence et al. [*Lawrence et al.*, 2011] statistically evaluated global surface air temperature for both CCSM3 and CCSM4, and found a slight improvement in CCSM4, with smaller cold bias and 20% reduction in root-mean-square error. The ocean component is updated to the Parallel Ocean Program version 2 (POP2) [*Smith*, 2010], with substantial improvement over POP version 1.4 [*Dukowicz and Smith*, 1994; *Smith and Gent*, 2004; *Smith et al.*, 1992; *Smith et al.*, 1995] in CCSM3 and PCM in the parameterization of sub-grid scale [*Danabasoglu et al.*, 2011] and in the thermocline structure and SST [*Bitz et al.*, 2011] through increasing vertical resolution from 40 in CCSM3 (and 32 in PCM) to 60 vertical levels in CCSM4. The sea ice component is based on the Los Alamos National Laboratory Sea Ice Model, version 4 (CICE4) [*Hunke and Lipscomb*, 2008], that includes a new radiative transfer scheme [*Holland et al.*, 2011]. The simulations from 1850 to 2005 are referred to as historical simulations, while the RCP scenarios cover 2005 to 2100. In the historical simulations, time varying CO_2 and other greenhouse gases are prescribed. The atmospheric aerosol burden, aerosol deposition rate onto snow and nitrogen deposition rates were time dependent, and they were obtained from a separate historical global atmospheric chemistry model CAM-Chem simulations [*Lamarque et al.*, 2010]. Five ensemble members of RCP scenarios are available from 2005 to 2100 on monthly and daily resolution scales in the Earth System Grid (ESG), a Gateway to scientific data including CMIP5 simulation outputs. For the historical simulations, five ensemble members are also available on a monthly scale, while three members are available on a daily scale.

4.5 Intensity, duration and frequency of regional heat waves

4.5.1 Evaluation and intensification of heat wave intensity

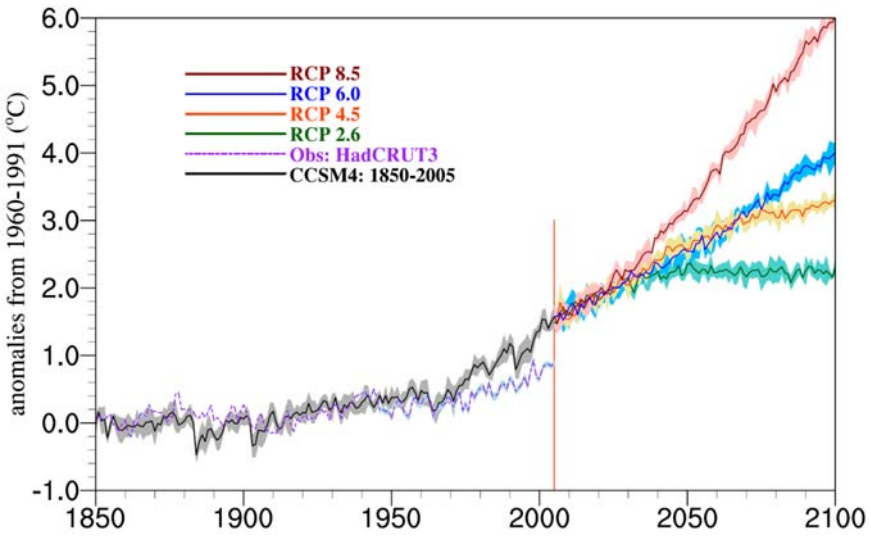

Figure 4.1 Time series of global annual mean surface air temperature anomalies (°C) from 1850 to 2100 (relative to 1900-1919). The solid lines indicate ensemble average while the shaded areas indicate ± one standard deviation. Note that for the observational data, the shaded areas indicate 95% confidence interval due to the data availability.

A time series of global annual mean surface air temperature anomalies (relative to 1900-1919) from 1850 to 2100 is shown in Figure 4.1. The observational temperature anomalies are from HadCRUT3 [*Brohan et al.*, 2006]. During the historical simulations, the trend from CCSM4 is consistent with observational data even though after 1975, the model simulations show more dramatic increasing temperature trends. From 1850 to 1975, the temperature warming in CCSM4 is 0.13 ºC ± 0.04 ºC, while the observed warming is 0.15 ºC ± 0.01 ºC, with an overall bias (CCSM4 - HadCRUT3) of -0.02 ºC ± 0.03ºC. From 1975 to 2005, the CCSM4 show larger warming trends (1.04 ºC ± 0.04 ºC) than observed warming (0.58 ºC ± 0.05 ºC), with an overall positive bias of 0.46 ºC ± 0.04 ºC, which is likely related to the absence of the sulfate aerosol indirect effect [*Meehl et al.*, 2011].

Relative to 1900-1919, the global mean temperature increase is 0.47 ºC ± 0.04 ºC during the 20th century (from 1900 to 2005) and is 2.12 ºC ± 0.01 ºC, 2.58 ºC ± 0.01 ºC, 2.69 ºC ± 0.05 ºC, 3.52 ºC ± 0.04 ºC for RCP 2.6, RCP 4.5, RCP 6.0 and RCP 8.5

(referred to as four RCP) scenarios, respectively, during the 21st century (2005-2100). By the end of the century, the increase reaches 2.31 ºC ± 0.12 ºC, 3.30 ºC ± 0.11 ºC, 4.00 ºC ± 0.14 ºC and 6.03 ºC ± 0.07 ºC in the four RCP scenarios. Even if the warming bias (0.46 ºC) is excluded, the global mean increase still ranges from 1.73 to 5.64 ºC by the end of 21st century.

Heat waves are regional/local phenomenon, so the global land area (except for Antarctica) was divided into 22 regions defined by Giorgi and Francisco [*Giorgi and Francisco*, 2000], shown in Figure 4.2.

Spatial distributions of ensemble mean heat wave intensity anomalies were shown in Figure 4.3. Similar patterns, with values from 0 to 1, in Figure 4.3 (a) and (b) demonstrates relatively reasonable performance in CCSM4 compared with NCEP. The evaluation period of 1948-2005 is close to the base period (1961-1990), which leads to small heat wave intensity anomalies across the whole world. Looking at the four RCP scenarios from 2.6 to 8.5 (Figure 4.3 c, e, g and i), during 2005 to 2100, an increasing trend shows up for the increase of heat wave intensity, and particularly, this increase is more dramatic in the northern hemisphere than the southern hemisphere. Comparing the mean increase of 2005-2100 with the increase in 2100 in every scenario (each row from second row in Figure 4.3), much more intense increases were found in 2100, with scattered increases around 3 ºC in RCP 2.6 (Figure 4.3 d), and large areas more than 5 ºC

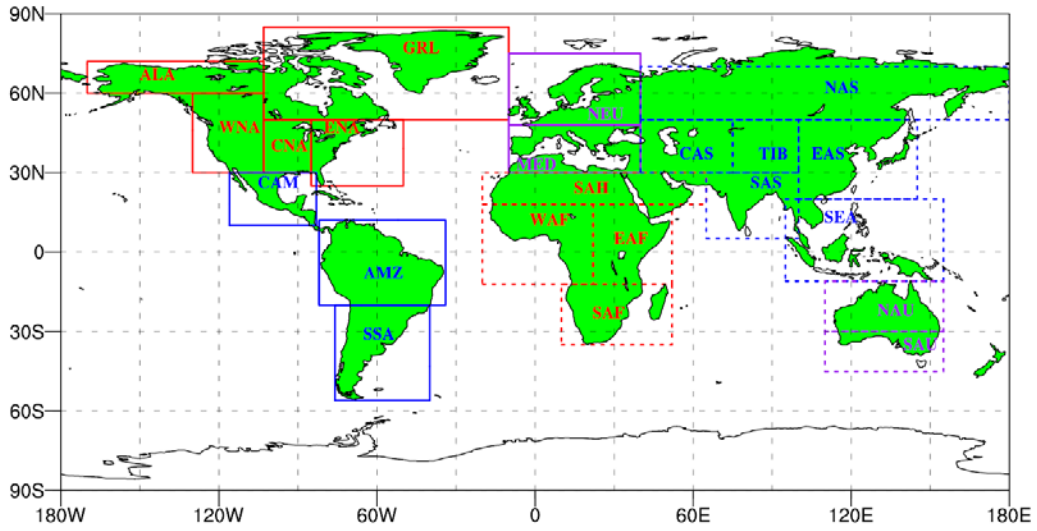

Figure 4.2 22 Regions used in the heat waves studies

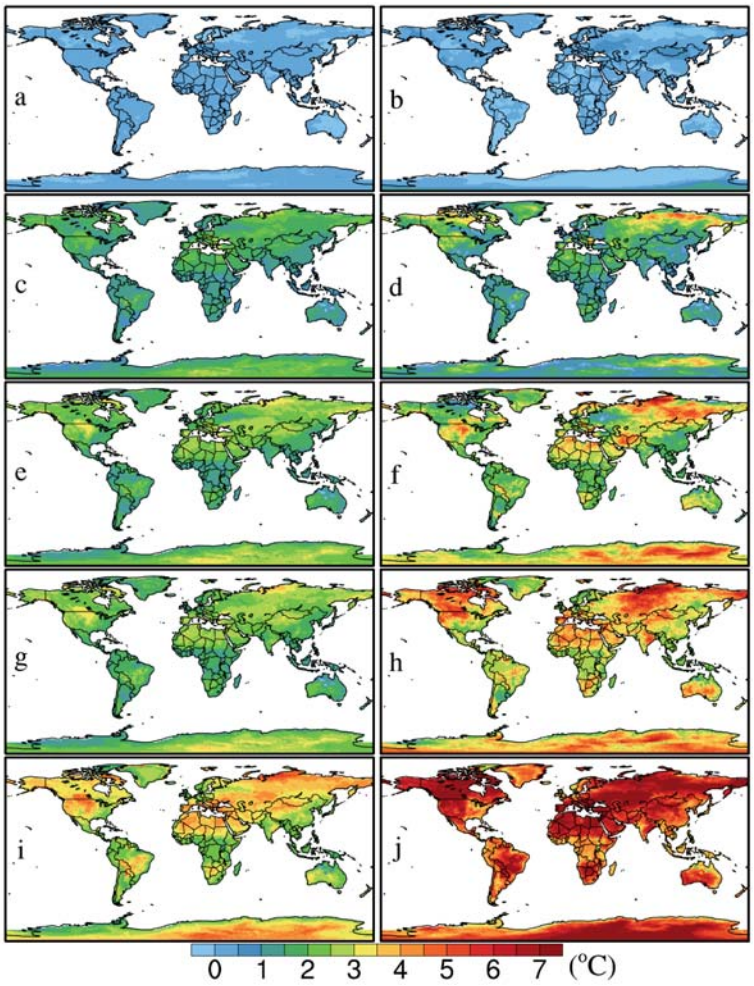

Figure 4.3 Ensemble mean heat wave intensity anomalies (relative to 1961-1990): a: ensemble mean heat wave intensity anomalies (relative to 1961-1990) from CCSM4 during 1948-2005, b: the same as a, but from NCEP; c, e, g and i (left column): ensemble mean heat wave intensity anomalies (relative to 1961-1990) for RCP 2.6, RCP 4.5, RCP 6.0 and RCP 8.5, respectively, during 2005-2100 from CCSM4; d, f, h and j (right column): ensemble mean heat wave intensity anomalies (relative to 1961-1990) for RCP 2.6, RCP 4.5, RCP 6.0 and RCP 8.5, respectively, in the year of 2100 from CCSM4.

(Figure 4.3 f, h and j) for the other three scenarios. Especially, in RCP 8.5, more than half of the world is projected to increase 7 ºC or even more.

The heat wave intensity anomalies (relative to 1961-1990) for the 22 global land regions were shown in Figure 4.4. The regions with the same color are considered to be

within the same continents, including North America (solid red), South America (solid blue), Europe (solid purple), Africa (dashed red), Asia (dashed blue) and Australia (dashed purple). Compared with NCEP, the mean bias during 1948-2005 in CCSM4 ranges from -0.27 ºC ± 0.06 ºC to 0.29 ºC ± 0.01 ºC in all the regions, showing a relatively small bias. In the four RCP scenarios, the mean heat wave intensity increase from 2005 to 2100 (relative to 1961-1990) ranges 0.94 ºC ± 0.01 ºC to 1.97 ºC ± 0.05 ºC (RCP 2.6), 1.27 ºC ± 0.01 ºC to 2.46 ºC ± 0.04 ºC (RCP 4.5), from 1.37 ºC ± 0.02 ºC to 2.55 ºC ± 0.07 ºC (RCP 6.0) and from 1.95 ºC ± 0.02 ºC to 3.77 ºC ± 0.08 ºC (RCP 8.5). The lowest increase occurs in the Southeast Asia (SEA) region, while the largest increase occurs in Mediterranean Basin (MED).

The global heat wave intensity was investigated previously by Ganguly et al. [2009] using Community Climate System Model version 3 (CCSM3) for the SRES A1FI scenario; they found that by the end of 21st century, the severity of heat waves does not increase much at higher latitudes and, in western North America, it does not increase as much as Central and Eastern America. However, using the new CCSM4 results, the higher latitude land areas show significant heat wave intensity increase (Figure 4.3 and Figure 4.4) by the end of 21st century, especially in RCP 8.5, this increase reaches 6.80 ºC ± 0.97 ºC, 5.75 ºC ± 0.83 ºC, 5.29 ºC ± 1.29 ºC, 6.85 ºC ± 0.47 ºC in ALA (Alaska), GRL (Greenland), NEU (Northern Europe) and NAS (North Asia), respectively. In addition, the heat wave intensity, in WNA (Western North America) shows larger increases than CNA (Central North America) and ENA (Eastern North America) in almost all the four RCP scenarios (except RCP 4.5) by the end of 21st century. The intensification is especially noticeable in the RCP 8.5 scenario with an increase in WNA of 7.01 ºC ± 0.58 ºC, while CNA and ENA experience increases of 5.11 ºC ± 0.65 ºC and 4.57 ºC ± 0.27 ºC, respectively.

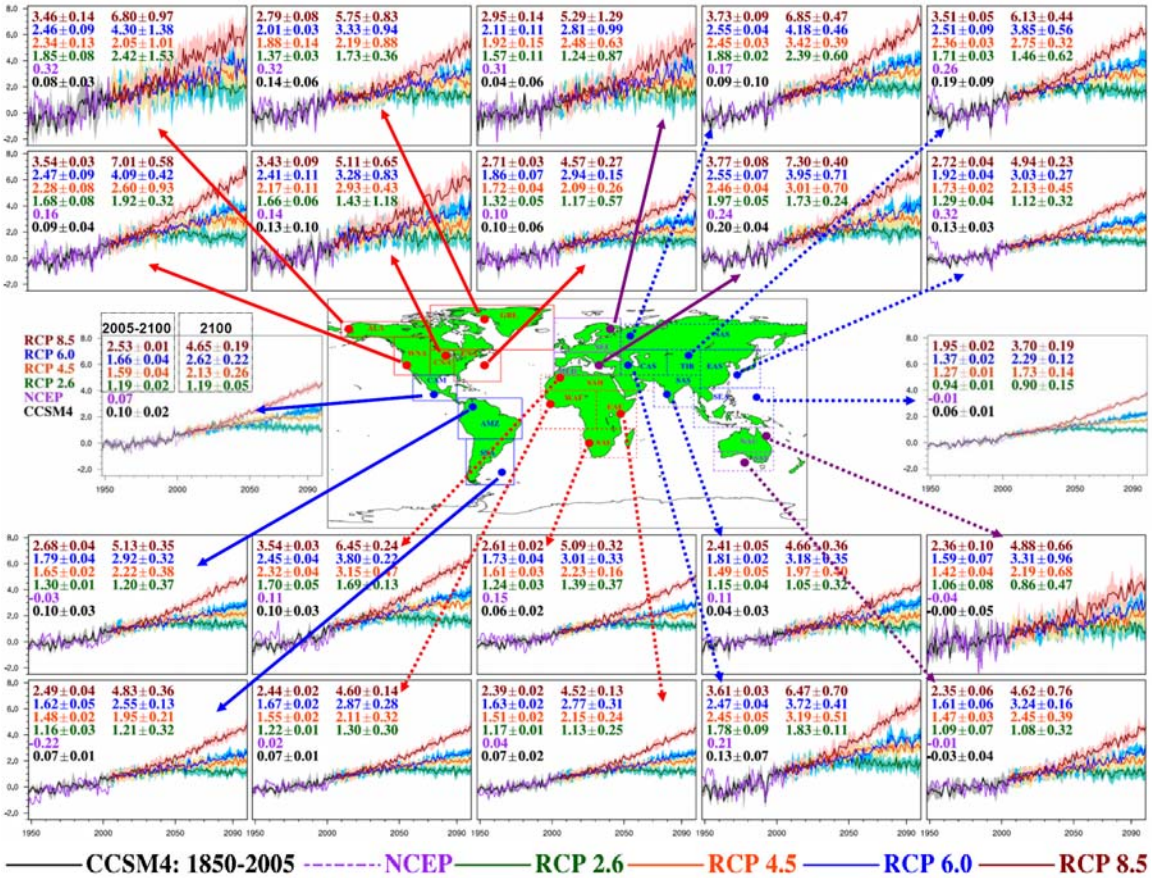

Figure 4.4 Ensemble heat wave intensity anomalies (relative to 1961-1990) ± one standard deviation. In each plot, there are two columns of numbers: On the left, the numbers from bottom to top indicate heat wave intensity ensemble mean anomalies (relative to 1961-1990) ± one standard deviation for CCSM4 (1948-2005), NCEP (1948-2005), RCP 2.6 (2005-2100), RCP 4.5 (2005-2100), RCP 6.0 (2005-2100) and RCP 8.5(2005-2100), respectively (except no standard deviation for NCEP); On the right, the numbers from bottom to top have similar meaning as the top four number in the left column, but for the year of 2100 (the end of 21st century) in the four RCP scenarios.

4.6 Heat wave duration and frequency (number of heat wave events)

As is shown in Table1, Meehl and Tebaldi [2004], using the Parallel Climate Model (PCM), found that, during the period of 1961-1990, ensemble mean heat wave duration ranges from 5.39 to 8.85 days in Chicago under a “business-as-usual” scenario (similar to

SRES A1B), compared to 6.29 days from NCEP. The same model results show values ranging from 8.33 to 13.69 days for Paris, compared with 8.40 days from NCEP. For the same period, the ensemble mean durations ranged from 5.99 to 11.99 days in Chicago and 5.51 and 10.54 days in Paris in CCSM4, both of which encompass the NCEP values and are similar to the ranges from the PCM scenario. At the end of the century (2080-2099), the A1B from PCM result in ensemble mean duration values from 8.47 days to 9.24 days in Chicago, and 11.39 days to 17.04 days in Paris. The CO_2 concentrations in SRES A1B is close to RCP 6.0 by the end of 21st century [*Meehl et al.*, 2011], however, the duration in PCM scenario is much lower than RCP 6.0 (20.96 days ± 1.35 days) for Chicago, but the upper bound of PCM scenario (17.04 days) is close to RCP 6.0 (18.69 days ± 1.04 days) for Paris. Possibly, the higher duration in Chicago in RCP 6.0 results from a slightly different parameterization than A1B as well as the higher resolution in CCSM4 (0.9° by 1.25° in latitude/longitude) than PCM (2.8° in latitude/longitude) [*Meehl et al.*, 2011].

Heat wave ensemble annual mean events in Chicago and Paris for PCM and RCP scenarios are also shown in Table 4.1. Compared to NCEP, both PCM and CCSM4 encompass the NCEP value. At the end of the 21st century (2080-2099) years, the number of annual heat wave events for Chicago in PCM (1.65-2.44) is close to the RCP 6.0 (2.45±0.15) in CCSM4, while it is slightly lower in PCM than RCP 6.0.

Table 4.1 Heat wave duration and frequency (number of events per year)

		1961-1990			2080-2099				
						CCSM4**			
		NCEP	PCM*	CCSM4	PCM*	RCP2.6	RCP 4.5	RCP 6.0	RCP 8.5
Duration	Chicago	6.29	5.39-8.85	5.99- 11.99	8.47-9.24	12.75±1.61	16.69±1.23	20.96±1.35	35.18±1.22
	Paris	8.40	8.33-13.69	5.51-10.54	11.39- 17.04	13.10±2.13	15.50±2.64	18.69±1.04	29.73±2.52
Events	Chicago	1.38	1.09-2.14	0.75-1.11	1.65-2.44	2.12±0.22	2.42±0.17	2.45±0.15	2.3±0.13
	Paris	1.10	1.18-2.17	0.87-1.13	1.70-2.38	2.08±0.18	2.82±0.25	0.98±0.26	3.09±0.29

*All the values for PCM is from Meehl and Tebaldi [2004].

**All the values for RCP scenarios in CCSM4 are mean ± one standard deviation

As is shown in Table 4.2 (also Figure 4.5 and Figure 4.6), during 1948-2005, the ensemble mean heat wave durations for CCSM4 (bottom left number on the left column in each figure) range from 5.07 days ± 0.2 days to 9.72 days ± 0.45 days with a mean of 7.80 days ± 0.19 days among the 22 regions. The mean duration days in CCSM are close to NCEP, with a mean bias of -0.10 days ± 0.19 days among the 22 regions. During the 21st century (2005-2100), a significant increase in heat wave duration is projected to occur in the majority of the regions, with the lower bound occurring in NAU (North Australia) and upper bound occurring in MED (Mediterranean Basin). Overall, compared to the period of 1948-2005, the mean duration increase in 2005-2100 is 45%, 69%, 75% and 126%, respectively, and the increase reaches 45%, 103%, 140% and 275% by the end of 21st century, respectively for the four RCP scenarios. Thus, by the end of the century, the mean regional duration days ranges from 1.45 to 3.74 times as high as the mean duration days from 1948 to 2005.

Table 4.2 Heat wave durations in 22 regions

Regions	CCSM4 (1948-2005)	NCEP (1948-2005)	RCP2.6 (2005-2100)	RCP4.5 (2005-2100)	RCP6.0 (2005-2100)	RCP8.5 (2005-2100)
ALA	9.07±0.51	8.85	12.46±0.36	13.39±0.41	13.70±0.26	17.37±0.65
GRL	9.72±0.45	9.78	13.20±0.25	15.69±0.53	16.30±0.41	20.83±0.33
WNA	8.35±0.21	7.81	13.52±0.39	16.37±0.27	16.78±0.40	21.98±0.37
CNA	8.92±0.34	7.15	14.23±0.13	16.73±0.65	17.70±0.69	23.93±0.57
ENA	7.41±0.14	6.65	12.05±0.39	14.78±0.29	15.07±0.28	20.69±0.24
CAM	7.64±0.42	7.77	12.41±0.22	14.73±0.26	15.33±0.29	21.40±0.14
AMZ	8.39±0.11	8.41	13.16±0.13	14.91±0.16	15.15±0.19	18.81±0.32
SSA	6.22±0.10	5.83	7.45±0.05	8.01±0.08	8.26±0.10	9.96±0.10
NEU	8.78±0.25	8.17	12.88±0.30	15.03±0.72	15.34±0.58	19.39±0.57
MED	8.86±0.16	8.16	16.25±0.27	19.77±0.45	20.07±0.68	27.89±0.32
SAH	7.49±0.07	8.42	12.03±0.19	14.59±0.14	14.93±0.18	18.72±0.32
WAF	7.21±0.06	8.41	10.03±0.10	11.23±0.15	11.63±0.08	14.52±0.14
EAF	7.95±0.03	8.45	11.38±0.05	12.70±0.13	13.15±0.08	15.54±0.04
SAF	6.93±0.10	6.34	9.56±0.14	10.64±0.20	10.88±0.16	13.01±0.07
NAS	8.04±0.05	8.52	10.97±0.16	12.63±0.18	12.94±0.10	16.95±0.45
CAS	8.08±0.08	8.93	12.77±0.58	16.10±0.26	16.37±0.29	22.87±0.22
TIB	7.01±0.08	8.25	9.72±0.11	11.77±0.24	12.23±0.22	16.43±0.31
EAS	7.73±0.26	8.86	10.77±0.20	12.16±0.16	12.78±0.17	15.61±0.16
SAS	9.00±0.18	9.98	12.74±0.24	14.79±0.23	15.61±0.21	19.79±0.36
SEA	7.22±0.34	8.05	9.21±0.08	11.13±0.08	11.96±0.12	17.83±0.28
NAU	5.07±0.20	4.87	6.02±0.12	6.38±0.04	6.65±0.22	8.23±0.15
SAU	6.53±0.12	6.13	8.48±0.11	9.28±0.08	9.57±0.10	11.13±0.13

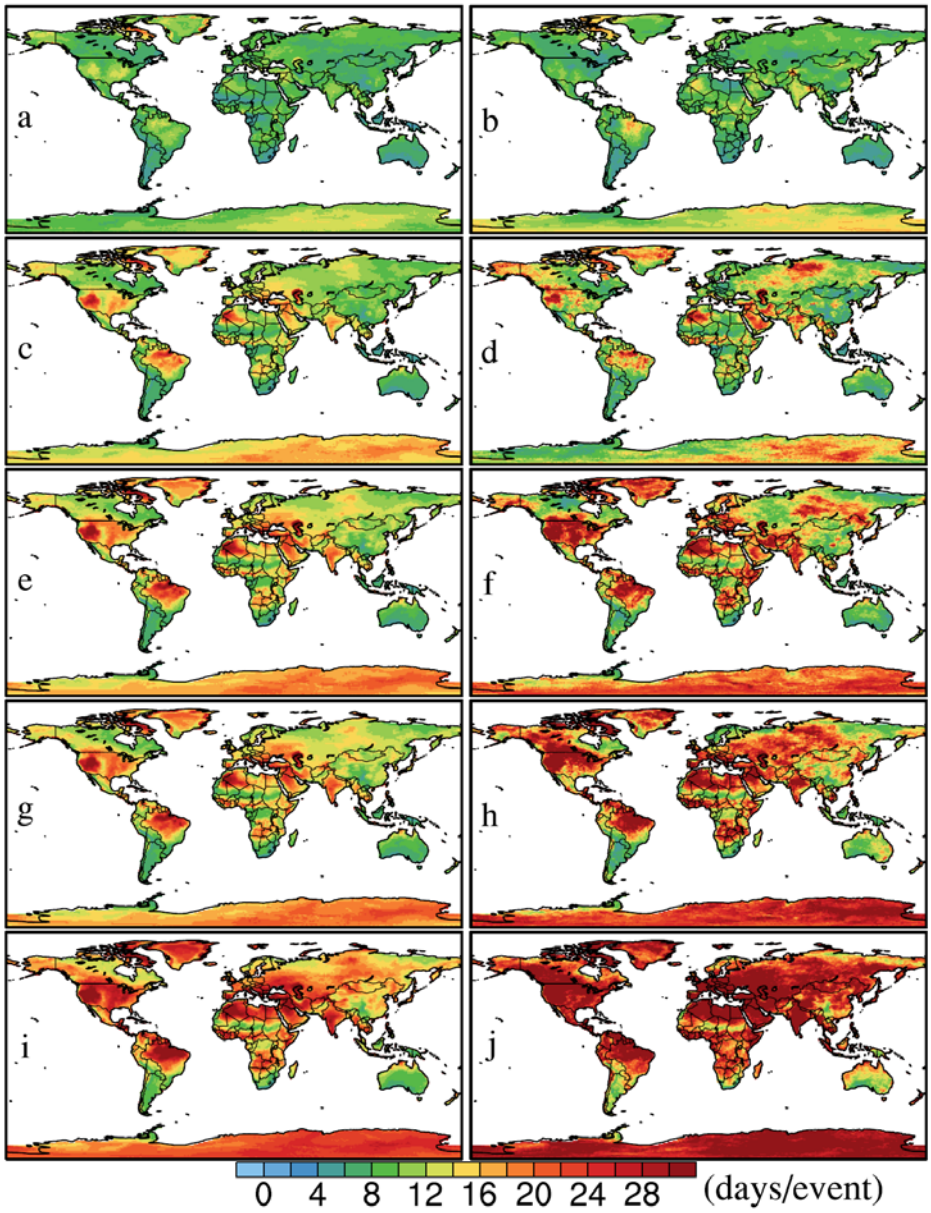

Figure 4.5 Ensemble mean heat wave durations: a: ensemble mean heat wave durations from CCSM4 during 1948-2005, b: the same as a, but from NCEP; c, e, g and i (left column): ensemble mean heat wave duration for RCP 2.6, RCP 4.5, RCP 6.0 and RCP 8.5, respectively, during 2005-2100 from CCSM4; d, f, h and j (right column): ensemble mean heat wave durations for RCP 2.6, RCP 4.5, RCP 6.0 and RCP 8.5, respectively, in the year of 2100 from CCSM4.

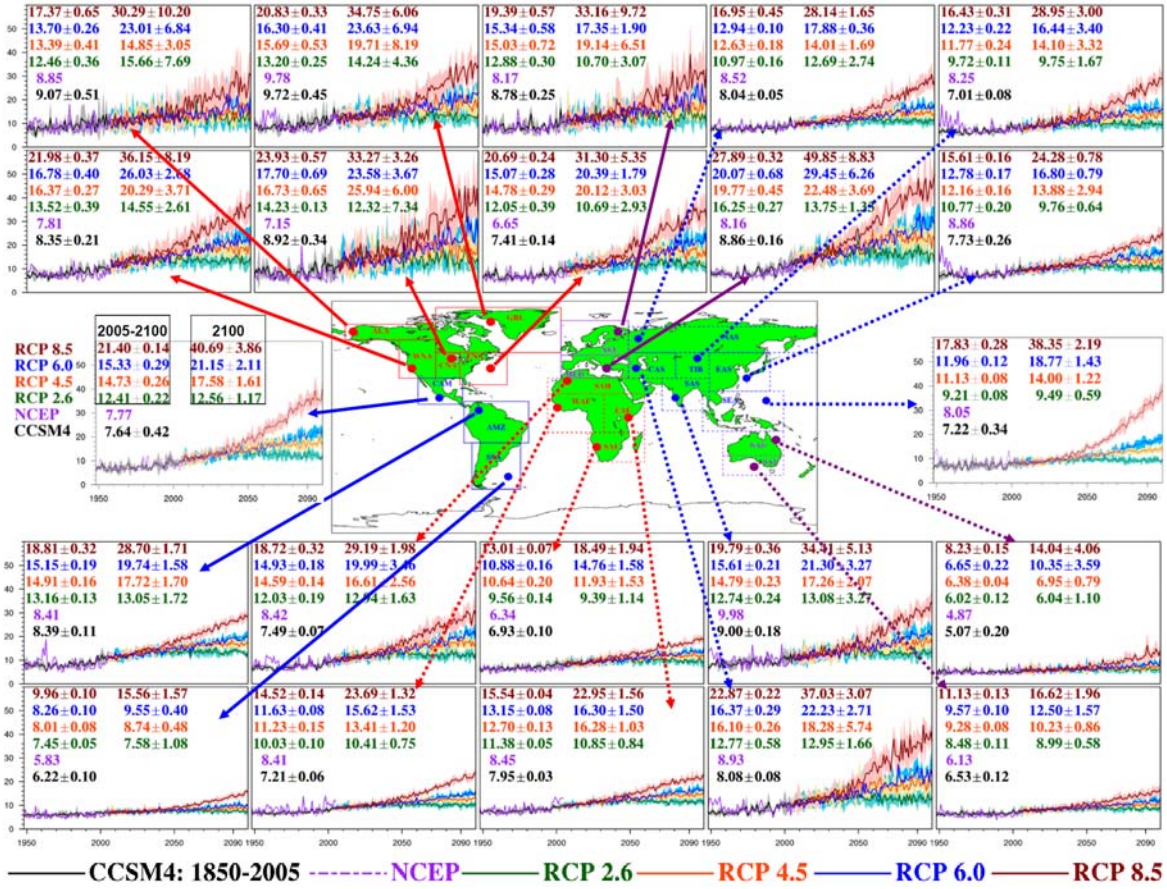

Figure 4.6 Ensemble mean heat wave durations ± one standard deviation. Similar as Fig. 2, in each plot, there are two columns of numbers: On the left, the numbers from bottom to top indicate heat wave duration ensemble mean ± one standard deviation for CCSM4 (1948-2005), NCEP (1948-2005), RCP 2.6 (2005-2100), RCP 4.5 (2005-2100), RCP 6.0 (2005-2100) and RCP 8.5(2005-2100), respectively (except no standard deviation for NCEP); On the right, the numbers from bottom to top have similar meaning as the top four number in the left column, but for the year of 2100 (the end of 21st century) in the four RCP scenarios.

Ensemble mean number of annual heat wave events (heat wave frequency) is shown in Figure 4.7 (with regional mean heat wave frequency shown in Figure 4.8). Figure 4.7 (a) and (b) shows similar spatial distributions of annual mean heat wave events between CCSM4 and NCEP, about one event each year for most of areas. More specifically, the

annual mean heat wave events (Figure 4.8) in the 22 regions in CCSM4 and NCEP are 1.03 ± 0.04 and 1.02, respectively, so NCEP falls within the range of CCSM4. For the four RCP scenarios during 2005-2100 (Figure 4.7 c, e, g and i), there are subtle differences for the number of annual heat wave events except RCP 2.6 shows much fewer events in the tropical areas. By the end of 21st century (Figure 4.7 (d, f, h and j), more than eight events per year occurs in large areas in the southern hemisphere especially in RCP 8.5. Overall, from Figure 4.7 (c)-(j), the large event increases occur near tropical areas and in the southern hemisphere, mainly from 60ºS-30ºN. The possible reasons were explored as below.

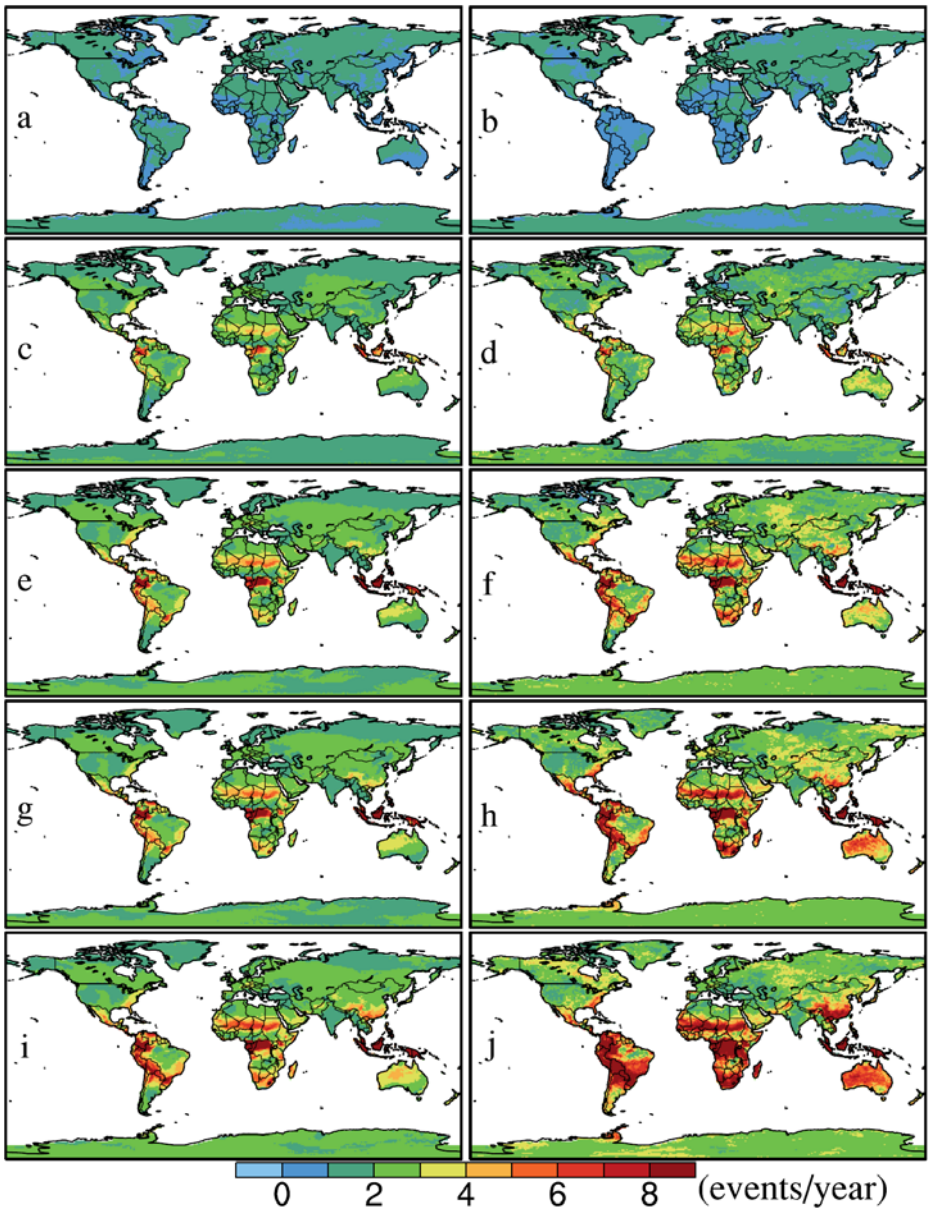

Figure 4.7 The same as Figure 4.5, but for the number of ensemble mean annual heat wave events.

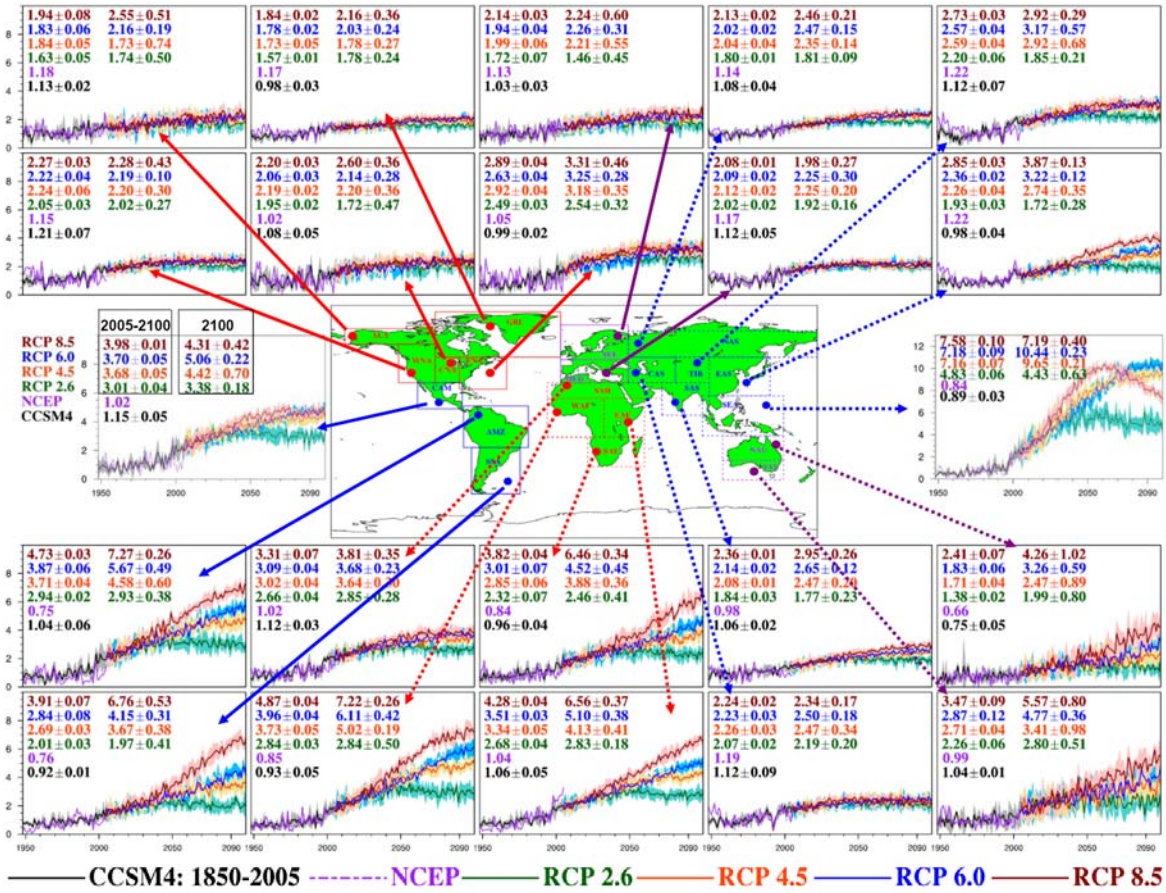

Figure 4.8 The same as Figure 4.6, but for the number of ensemble mean annual heat wave events.

The probability and cumulative probability distribution of daily maximum temperature from 1961-1990 and 2080-2099 are shown in Figure 4.9. From Figure 4.9, the seasonal variations of daily maximum temperature in regions between 30ºN-90ºN (referred to as North Region, marked as _N, and with a range of 255 K to 300 K) are much larger than regions between 60ºS-30ºN (referred to as South Region, marked as _S, and with a range of 298 K to 310 K). The regions (60ºS-30ºN) are surrounded by ocean, and high specific ocean heat capacity leads to small diurnal ocean temperature variations, also heating the surrounding land areas. This impact is especially noticeable in SEA (Southeast Asia, Figure 4.8), a region widely surrounded by ocean, where the largest number of annual heat wave events occurs.

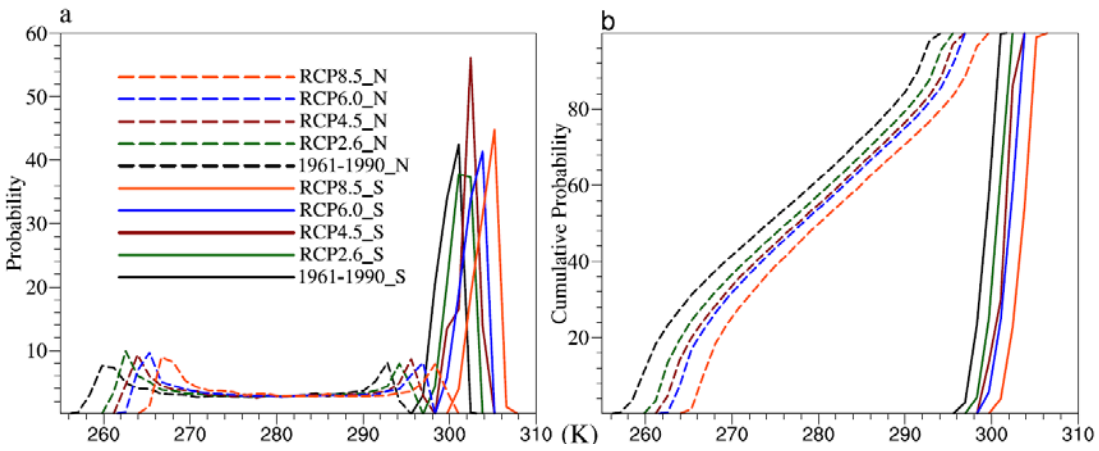

Figure 4.9 Daily maximum temperature probability (left) and cumulative probability (right). a. Probability distributions for ensemble mean daily maximum temperature for base period (1961-1990) and four RCP scenarios (2080-2099) in two regions (30ºN-90ºN, marked as _N and 60ºS-30ºN, marked as _S); b. Same as a but for cumulative distributions.

4.7 Probability distribution of duration and frequency of heat waves

In addition to observing the absolute value of the change in heat wave duration and frequency, the distribution change was also investigated, shown in Figure 4.10. In the present climate (Figure 4.10a), the largest percentile value, 38%, occurs at a duration of 9 days. The right-shift of the probability curves pushes the peak percentage of duration days to larger numbers of 11, 21, 23 and 31 days in the four RCP scenarios, with corresponding peak percentage of 19%, 14%, 13% and 12%, respectively. Looking at the cumulative probability curves in Figure 4.10b, the cumulative distribution for average heat wave duration shows obvious separation. This shift indicates that at same percentile, the four RCP scenarios (in 2080-2099) predict much higher average heat wave duration days than present climate (1961-1990). In 1961-1990, an average heat wave duration days of 12 or less accounts for 95%, while in the four RCP scenarios, the 95 percentile push the average duration days to 19 days or more.

Similar to heat wave duration, the heat wave frequency also shows a shift towards higher number of events. For present climate (Figure 4.10c), the largest percentile value, 49%, occurs at a number of events value of 1.13, while the peak percentage shifts to 1.88

to 2.38 among the four RCP scenarios. The cumulative probability plot (Figure 4.10d) shows significant shifting toward higher values for the number of events. For present climate conditions, 95% of heat wave event values are totaling 1.10 or less, while this number jumps to 3.38 to 7.88 for the RCP scenarios.

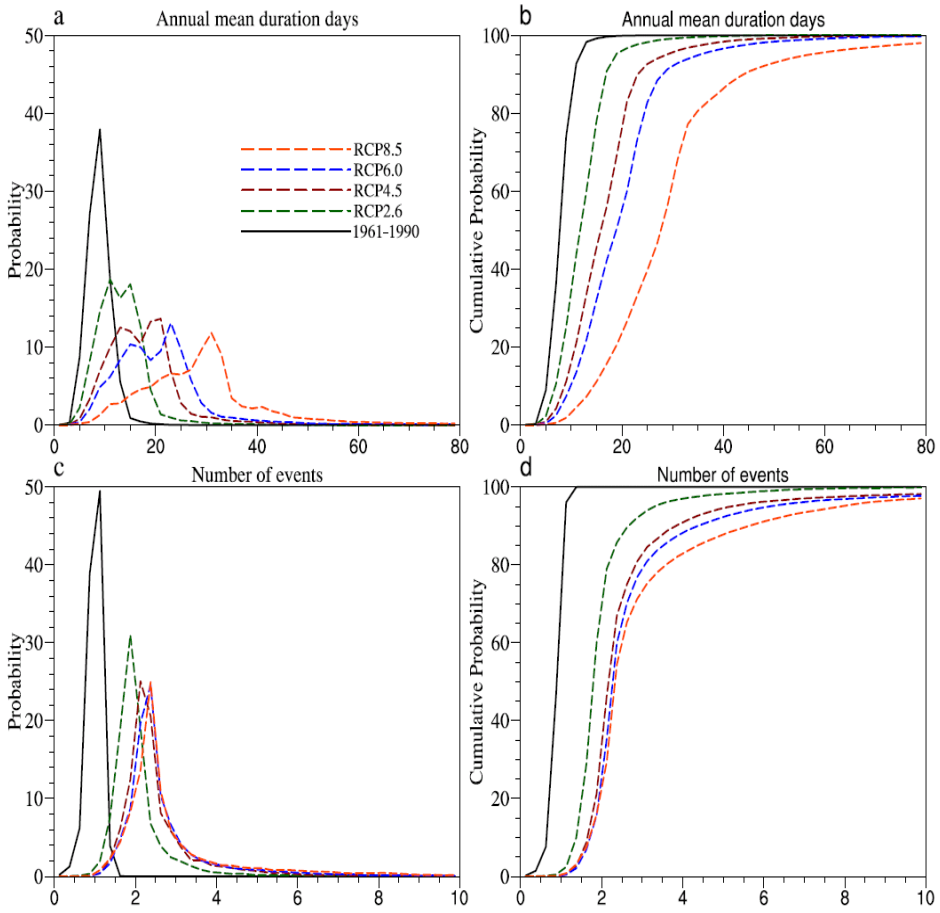

Figure 4.10 Probability and cumulative probability distributions of average heat wave duration and annual frequency for present climate (1961-1990), future climate (2080-2090) in RCP 2.6, RCP 4.5, RCP 6.0 and RCP 8.5. a and b show the probability and cumulative probability for average heat wave duration, while c and d show similar parameters but for heat wave frequency.

4.8 Seasonal extreme temperature duration (SETD)

Based on the two thresholds definition, heat waves most often occur in the summer, so extreme temperatures in other seasons are frequently ignored. To correct this deficiency, the duration of extreme temperature in each season was used to determine the Seasonal Extreme Temperature Duration (SETD). The same criteria and percentage thresholds as used for heat wave duration [*Meehl and Tebaldi*, 2004] can be applied to each season. SETD is the summation of all the extreme temperature periods in the season**.**

Figure 4.11 and Figure 4.12 shows the 22 regional ensemble mean SETD of the present climate (1961-1990) and future climate (2080-2099) for four RCP scenarios. In present climate, the SETD in DEC-JAN-FEB is significantly smaller than the other three seasons, especially in the North Region, the SETD in winter only accounts for a small percentage. However, in future climate, under RCP 8.5, the SETD in DEC-JAN-FEB increases dramatically, especially in the South Region (Figure 4.12), the increase in DEC-JAN-FEB SETD makes the four seasons show similar percentage. Based on Figure 4.11 and Figure 4.12, in the present climate, the SETD (among 22 regions) is from 0.59 days to 1.99 days in the four seasons, while in 2080-2099, it reaches 3.27 to 9.81 days, 8.18 days to 20.34 days, 11.72 days to 27.11 days and 24.69 days to 46.26 days, respectively, for the four RCP scenarios. In future climate scenarios, among the four seasons, the largest SETD percentage increase occurs in DEC-JAN-FEB (5.06 times to 39.98 times higher than present climate) in RCP 8.5, indicating a large temperature distribution change and temperature increase in winter time in the North Region and summer time in the South Region; the next largest increase occurs in JUN-JUL-AUG (4.79 times to 23.43 times), followed by SEP-OCT-NOV (4.47 times to 20.52 times) and MAR-APR-MAY (3.46 times to 13.96 times). In addition to the SETD increases, the SETD percentage among seasons also changes in future climate. The SETD percentage decreases in MAR-APR-MAY in both the North Region (-8% to -15%) and the South Region (-5% to -11%), but increases in DEC-JAN-FEB and JUN-JUL-AUG in both regions (1% to 8% in DEC-JAN-FEB and 1% to 13% in JUN-JUL-AUG), indicating a significant temperature increase in summer and winter in both North and South Region.

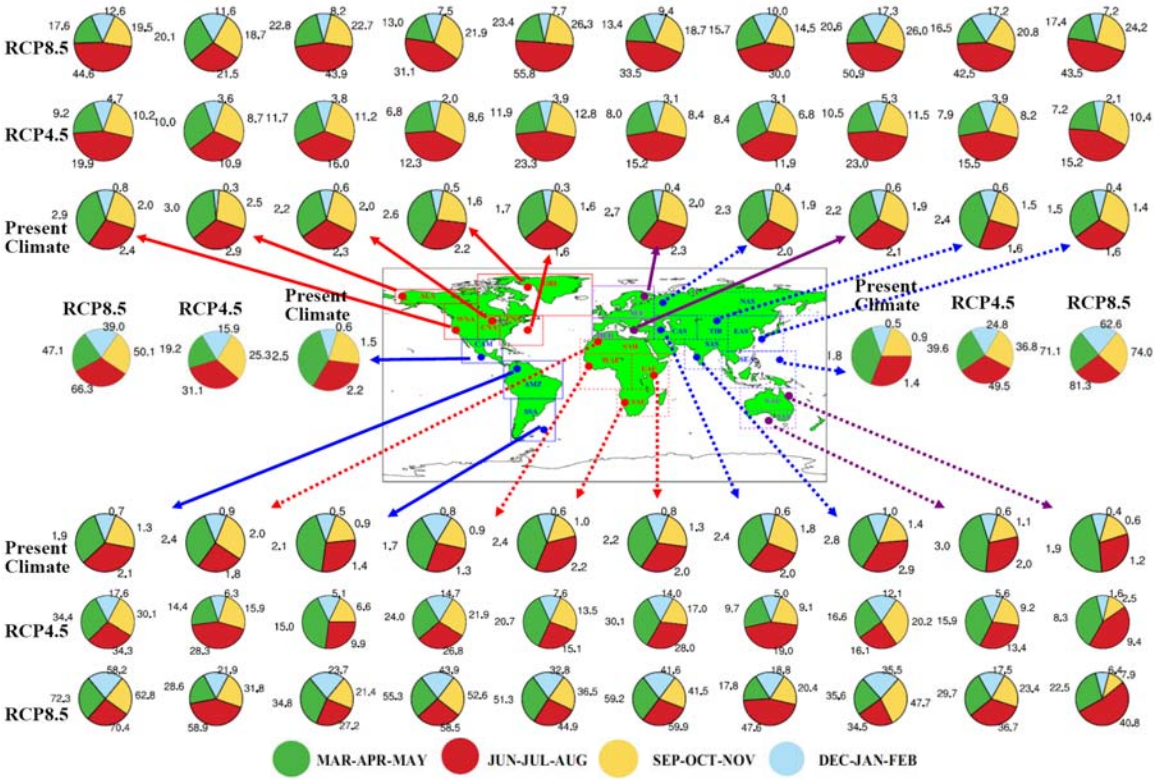

Figure 4.11 Seasonal extreme temperature duration (SETD) at present climate (1961-1990) and future climate (2080-2099) in RCP 4.5 and 8.5 (unit: days). The regions with the same color are considered to be within the same continents, including North America (solid red), South America (solid blue), Europe (solid gray), Africa (dashed red), Asia (dashed blue) and Australia (dashed gray). Four three-month segments are used to separate seasons. The pie charts show the area of each segment representing the relative size of the duration days in each season, while the number along each segment is not the fraction, but the true duration days for a certain season. The fraction can be simply derived by dividing the total duration number of the four seasons. The inner pie charts represent the period for present climate (1961-1990), while the outer ones represent 2080-2099 in RCP4.5 and 8.5.

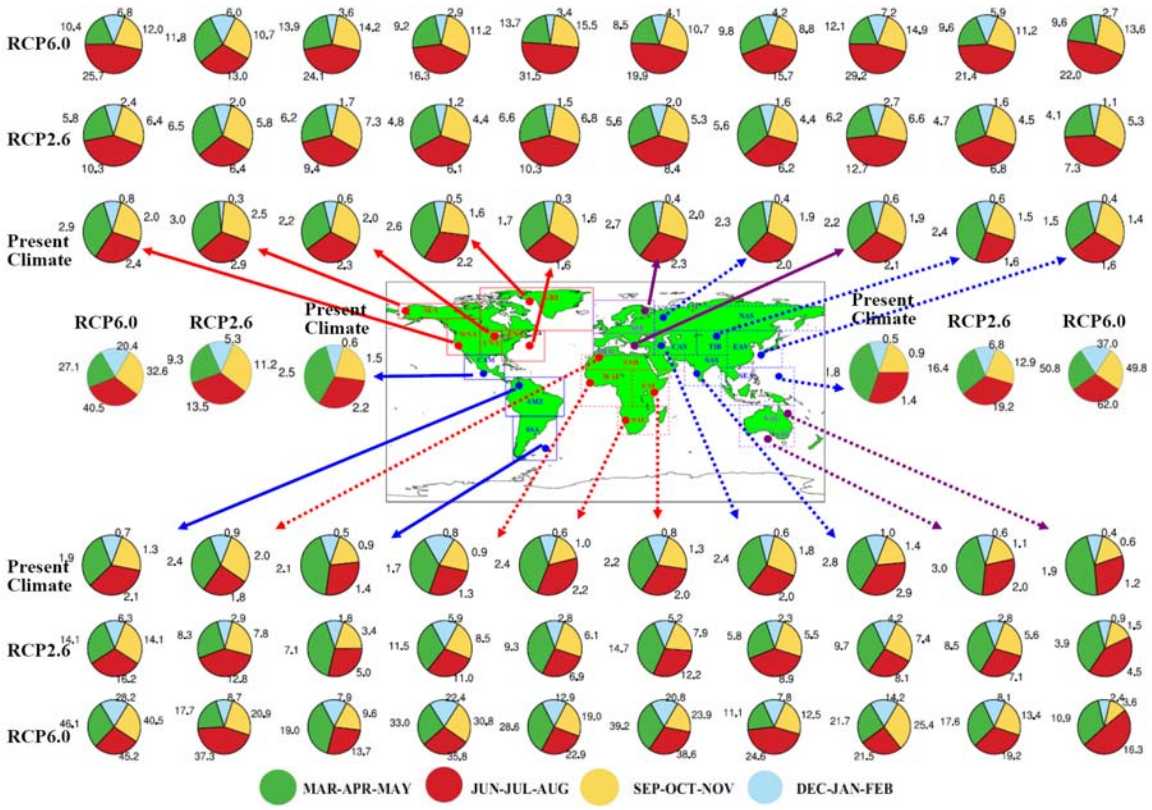

Figure 4.12 The same as Figure 4.11, but for RCP 2.6 and 6.0.

CHAPTER V

5 PROJECTED CHANGES OF EXTREME WEATHER EVENTS IN THE EASTERN UNITED STATES BASED ON A HIGH-RESOLUTION CLIMATE MODELING SYSTEM

5.1 Declaration

This chapter is a slightly revised version of the following paper:

Gao, Y., J. S. Fu, J. B. Drake, Y. Liu and J.-F. Lamarque (2012). Projected changes of extreme weather events in the Eastern United States based on a high-resolution climate modeling system. Environ. Res. Lett., 7, 044025.

5.2 Abstract

This study is the first evaluation of dynamical downscaling using the Weather Research and Forecasting (WRF) Model on a 4km by 4km high resolution scale in the eastern US driven by the new Community Earth System Model version 1.0 (CESM v1.0). First the global and regional climate model results were evaluated, and corrected an inconsistency in skin temperature during the downscaling process by modifying the land/sea mask. In comparison with observations, WRF shows statistically significant improvement over CESM in reproducing extreme weather events, with improvement for heat wave frequency estimation as high as 98%. The fossil fuel intensive scenario Representative Concentration Pathway (RCP) 8.5 was used to study a possible future mid-century climate extreme in 2057-2059. Both heat waves and extreme precipitation in 2057-2059 are more severe than present climate in the Eastern US. The Northeastern US shows large increases in both heat wave intensity (3.05 ºC higher) and annual extreme precipitation (107.3 mm more per year).

5.3 Introduction

Global climate models (GCMs) are designed to simulate large scale global climate at a spatial resolution of several hundred kilometers [*IPCC*, 2007]. However, finer spatial resolution has become increasingly important when studying the impact of climate

change at the local level [*Caldwell et al.*, 2009]. There are two primary methods for studying climate change in more spatial detail: statistical downscaling and dynamical downscaling. Statistical downscaling establishes the empirical relationships between large-scale climate and local climate based upon statistical methods [*Fowler et al.*, 2007]. It demands less computational power and requires less effort to implement, but it is limited by assuming stationary relationship between present observations and the present model climate in a changed future climate [*Diaz-Nieto and Wilby*, 2005]. Dynamical downscaling uses GCMs output to provide the initial and boundary conditions for the regional climate models (RCMs) projecting globally consistent high resolution local climate conditions [*Caldwell et al.*, 2009]. It is computationally demanding and requires considerable implementation effort, but a major advantage is the dependence on physical process rather than statistical correlations and there is no assumption of stationarity [*Fowler et al.*, 2007]. Thus, in order to capture extreme conditions and provide more regional detail, the dynamical downscale technique is used in this study.

Dynamical downscaling has been studied since the early 1990s [*Dickinson et al.*, 1989; *Giorgi*, 1990; *Giorgi et al.*, 1994; *Leung et al.*, 1996; *Podzun et al.*, 1995] - using RCMs with spatial resolutions of 50-60 km. More recently, finer spatial resolution has been applied. Bell et al. [*Bell et al.*, 2004] conducted dynamical downscaling on a 40 km by 40 km resolution, and found 75% of RCMs perform similarly or more favorably than GCMs over 16 stations in California region. Salathe et al. [*Salathé et al.*, 2008] evaluated daily maximum, minimum temperature and precipitation over 55 stations in the Northwestern US at 15 km resolution, and found a cold bias in downscaled RCM results, which is likely inherited from the GCM. Other high resolution downscaling studies were also conducted for California [*Caldwell et al.*, 2009; *Pan et al.*, 2011; *Qian et al.*, 2010]. As these studies have a major focus in the western US, the high resolution dynamical downscaling was previously ignored in the Eastern US. Since the small domain size in previous studies limits the number of observational data (only 16 in Bell et al. [2004] and 55 in Salathe et al. [2008]), it would be more meaningful and representative to evaluate a larger domain with more observational sites (more than 1000), thus the design of a larger eastern US domain in this study. In addition, most previous downscaling studies use

National Center for Atmospheric Research (NCAR) GCM Parallel Climate Model (PCM) or Community Climate System Model version 3 (CCSM3). The PCM has been superseded by the CESM, which includes an updated atmosphere component, the Community Atmosphere Component version 4 (CAM4) [*Neale et al.*, 2010]. To provide downscaling analysis with the new GCM model is the purpose of this study. At the end, the discussions of the newest Coupled Model Intercomparison Project Phase 5 (CMIP5) ([*Taylor et al.*, 2009; *Taylor et al.*, 2012] 'representative concentration pathways[*] (RCPs [*Moss et al.*, 2010]) scenarios in this study could potentially contribute to the upcoming Fifth Assessment Report (AR5) of the United Nations Intergovernmental Panel on Climate Change (IPCC). Thus, the eastern US domain is targeted in this study with a high resolution (4 km by 4 km) to provide an understanding of the dynamics of climate change on a highly resolved regional basis.

A higher resolution is necessary for climate studies of extreme weather events [*Caldwell et al.*, 2009]. Extreme weather events have already significantly influenced North America. According to Lott and Ross [2006] nearly every year since 1980, extreme weather events have caused more than 1 billion dollars in damage in the US. Prior to 2005, four or fewer events occurred yearly; while 5 events were experienced in 2005, an extreme peak was reached with 14 events occurring in 2011[**]. In 2005 the annual loss due to extreme weather events totaled 100 billion dollars, mainly due to Hurricane Katrina. A more commonly occurring extreme event, heat waves, can inflict substantial harm on sensitive populations including the elderly and people with pre-existing health conditions. For instance, several hundred people died in 1995 during the Chicago heat wave and more than 30,000 deaths were attributed to the 2003 European heat wave [*Robine et al.*, 2008; *Whitman et al.*, 1997]. In 2010, about 55,000 premature deaths were attributed to the Russian heat wave ("2010 Disasters in Numbers" CRED***). In addition, more intense heat waves [*Ganguly et al.*, 2009; *Meehl and Tebaldi*, 2004] and

---

[*] http://www.iiasa.ac.at/web-apps/tnt/RcpDb/dsd?Action=htmlpage&page=about

[**] http://www.ncdc.noaa.gov/billions/

[***] http://cred.be/sites/default/files/PressConference2010.pdf

precipitation [*Meehl et al.*, 2011] are likely to occur in a warmer climate. Thus, two kinds of extreme events, heat waves and extreme precipitation, were examined in this study under present and future climate conditions.

5.4 Model Description and Configuration

In this study, CESM version 1.0 was used for global climate simulations. CESM 1.0, the state-of-the-art global climate model developed by the NCAR, is composed of four major components including atmosphere, ocean, land surface and sea-ice. The atmospheric component CAM4, described earlier, uses the finite-volume (FV) dynamical core [*Neale et al.*, 2010] with a horizontal latitude/longitude grid of 0.9 by 1.25 degree and 26 vertical layers. The land component is the Community Land Model (CLM4) [*Oleson*, 2010], which incorporates the effects of CO_2 and Nitrogen on plant fertilization and growth [*Thornton et al.*, 2009]. The ocean component is the Parallel Ocean Program version 2 (POP2) [*Smith*, 2010], with dramatic improvement in the thermocline structure and SST [*Bitz et al.*, 2011] over POP version 1.4 [*Smith et al.*, 1992; *Smith et al.*, 1995] used in CCSM3 and PCM. The sea ice component uses the code from the Los Alamos National Laboratory Sea Ice Model, version 4 (CICE4) [*Hunke and Lipscomb*, 2008], on which substantial improvement has been achieved over new radiative transfer scheme and aerosols [*Holland et al.*, 2011].

The latest version of regional climate model WRF 3.2.1 [*Skamarock and Klemp*, 2008] was used in the regional climate simulations. The most widely used physics in US simulation domain was selected in this study, including: the new Kain-Fritsch convective parameterization [*Kain*, 2004; *Lam et al.*, 2011; *Qian et al.*, 2010; *Wong et al.*, 2012], the Single-Moment 6-class microphysical scheme (WSM6) [*Hong and Lim*, 2006; *Pan et al.*, 2011; *Qian et al.*, 2010; *Wong et al.*, 2012], the Mellor-Yamada-Janjic planetary boundary layer (PBL) scheme [*Janjić*, 1990; *Lam et al.*, 2011; *Mellor and Yamada*, 1982], and the Noah land surface model [*Chen and Dudhia*, 2001; *Lam et al.*, 2011; *Qian et al.*, 2010]. For the shortwave and longwave radiation scheme, the Rapid Radiative Transfer Model (RRTM), widely used in US WRF simulations [*Lam et al.*, 2011; *Lo et*

al., 2008], can reproduce highly accurate line-by-line results, while improved efficiency was provided by the new scheme RRTM for GCMs (RRTMG) [*Iacono et al.*, 2008; *Morcrette et al.*, 2008]. Thus, RRTMG was used in this study. Since there are no cumulus parameterization schemes suitable for the 4 km by 4 km scales at present [*Deng and Stauffer*, 2006], no convective parameterization scheme was used for the 4 km by 4 km domain.

Three domains were designed for WRF simulations, as is shown in Figure 5.1. The outer domain with a resolution of 36 km by 36 km is centered at 97º W, 40º N. The second domain is 12 km by 12 km and covers most of North America. The inner domain with a high resolution of 4 km by 4 km, shown in Figure 5.1, can be divided to three sub-regions based on the definition of the U.S. Global Change Research Program (USGCRP): Northeast (red color), Eastern Midwest (blue color) and Southeast (green color) regions.[*]. The colored points in each state represent the observational data point over quality controlled National Climatic Data Center (NCDC) US COOP network station observations (referred to as NCDC)[**], which will be used for model evaluations in the next section. This dataset is selected to evaluate extreme events; daily maximum temperature, daily minimum temperature and daily precipitation are required for the evaluations. The observational data has been well documented by Meehl et al. [2009]. This domain size is significant and computationally intensive, but the high computational effort for these regions is justified since the regions contain large populations which may be affected by climate change. The main purpose of this study is high resolution downscaling; the regional climate analysis will mainly focus on the downscaled 4 km by 4 km Eastern US.

[*] http://globalchange.gov/publications/reports/scientific-assessments/us-impacts/regional-climate-change-impacts

[**] http://dss.ucar.edu (dataset number ds510.6)

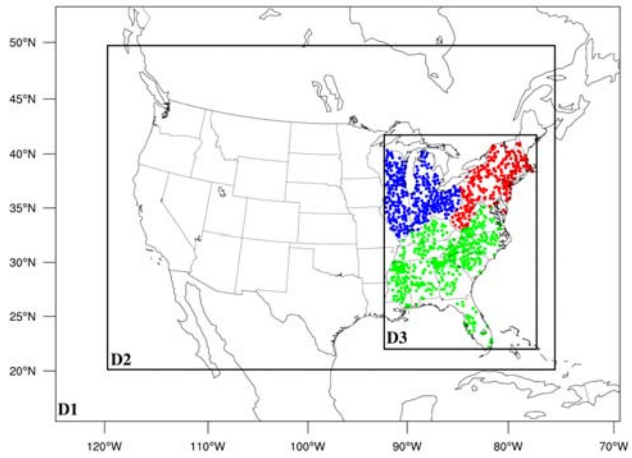

Figure 5.1 WRF simulation domains: D1 (36 km by 36 km resolution), D2 (12 km by 12 km) and D3 (4 km by 4 km). The points represent NCDC US COOP network station observation points in three regions: Northeast (red color), Eastern Midwest (blue color) and Southeast (green color).

For the CMIP5, present climate simulations and four future climate RCP (RCP 2.6, RCP 4.5, RCP 6.0 and RCP 8.5) scenarios were designed. The present climate simulations with CESM are from 1850 to 2005 and the RCP scenarios are from 2005 to 2100. The analysis of global climate simulations were well documented by Meehl et al. [2011]. Considering the limited computational resources in this regional high resolution downscaling study, a four year period (2001-2004) was selected to represent present climate and one RCP scenario (RCP 8.5, [*Riahi et al.*, 2007]) was used to illustrate future climate conditions from 2057-2059. Among the four RCP scenarios, RCP 8.5 projects the most intensive fossil fuel emissions, which is comparable [*Meehl et al.*, 2011] to the Special Report on Emissions Scenarios (SRES) A1FI [*Nakicenovic and Swart*, 2000] scenario.

5.5 The representative of present and future climate

A four year (2001-2004) was selected as present climate and a three year period (2057-2059) as future climate. The selections of the climate periods take into consideration of computational resources and the representative in a 20 year period.

Three members of historical climate simulations (1850-2004) and five members of future climate simulations (RCP 8.5, 2005-2100) were used to justify the representative of the period (2001-2004/2057-2059) used in the regional climate downscaling.

Figure 5.2 shows the ensemble heat wave intensity ± one standard deviation (ºC) for present climate and future climate (RCP 8.5). Among the 23 states in the eastern United States, the mean heat wave intensity during 1985-2004 is 0.49 ºC ± 0.26 ºC to 0.88 ºC ± 0.07 ºC higher than 1850-2005, indicating a slightly warming trend in recent climate. The heat wave intensity during the 20-year period (1985-2004) and 4-year period (2001-2004) ranges from 20.81 ºC ± 0.29 ºC to 26.20 ºC ± 0.33 ºC and from 21.04 ºC ± 0.51 ºC to 26.59 ºC ± 1.37 ºC, respectively. The 4-year period shows slightly higher severity in comparison to the 20-year period, but the small differences between these two periods indicate the 4-year period can be used as present climate.

In future, the temperature is projected to increase in RCP 8.5 during 2005 to 2100. The mid-21st century is selected to determine the changes of heat wave, primarily considering the consistency among the three periods: 2005-2100, 2040-2059 and 2057-2059. During these three periods, the mean heat wave intensity ranges from 23.03 ºC ± 0.04 ºC to 28.82 ºC ± 0.11 ºC, from 22.88 ºC ± 0.12 ºC to 28.73 ºC ± 0.20 ºC and from 23.22 ºC ± 0.43 ºC to 28.54 ºC ± 0.57 ºC, respectively. Thus, under the limitation of computational resources, the period of 2001-2004 and 2057-2059 were selected as the present climate and future climate for the exploration of heat wave intensity.

In addition to heat wave intensity, similar comparisons were made for heat wave duration, heat wave frequency, annual total extreme precipitation, daily mean extreme precipitation and annual extreme precipitation days, listed in the Figure S2 to S6 in the APPENDIX. The period of 2001-2004 is comparable to 1985-2004 and 1850-2004, with slightly higher values in most of the case. Similarly, the period of 2057-2059 is also slightly higher in extreme events in comparison to 2040-2050. Since both of these two periods show slightly higher patterns in comparison to a 20-year period, the comparison/subtraction between present and future climate would reflect the change patterns from a 20-year period.

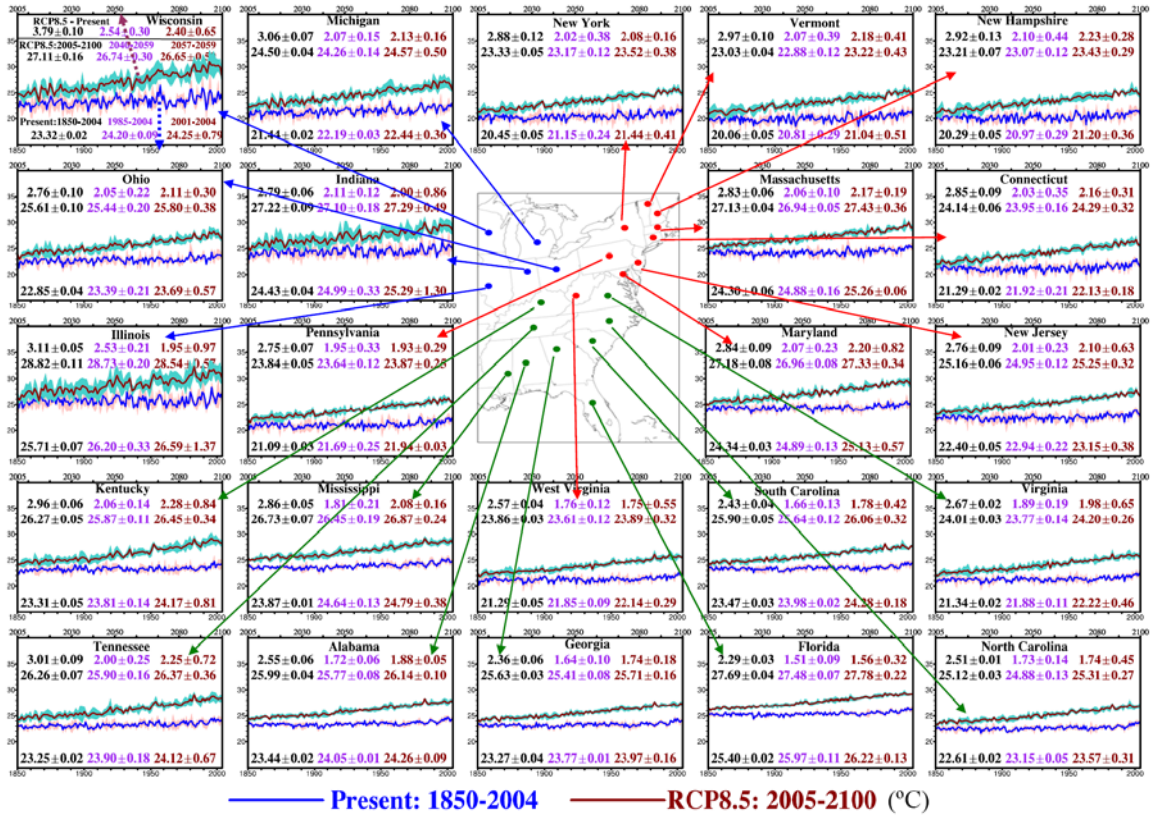

Figure 5.2 Ensemble heat wave intensity ± one standard deviation (ºC) for present climate and future climate (RCP 8.5). The X axis for present climate is scaled at the bottom while the future climate (RCP 8.5) is scaled at the top. In each plot, there are three rows of numbers (marked at the top-left plot): At the bottom, the numbers from left to right indicate heat wave intensity ensemble mean ± one standard deviation during 1850-2005, 1985-2004 and 2001-2004; In the middle, the numbers indicate the RCP 8.5 scenario for the period of 2005-2100, 2040-2059 and 2057-2059; At the top, the numbers indicate the differences between RCP 8.5 and present climate during the three periods listed above.

5.6 Dynamical Downscaling Methodology

At each three-hour interval, CESM outputs were dynamically used to establish boundaries for the outer WRF domain simulations. A number of variables, including both surface and three dimensional variables, are required for dynamical downscaling. Most of

the variables are extracted in the CAM4 outputs, while soil moisture and soil temperature are taken from the CLM4 history outputs.

Surface variables are horizontally interpolated from CESM (CAM4 and CLM4, 0.9 by 1.25 degree spatial resolution in latitude/longitude) to WRF simulation domains. In this step, the WRF Preprocessing System (WPS) is used to interpolate CESM output into WRF domains. Physics are not involved in this process, and theoretically, the outputs from CESM and WPS should show similar spatial patterns or integrity. The modification of skin temperature has been discussed in the Section 2.3.1.1.

5.7 State-level extreme events evaluations of dynamical downscaling

Before investigating the extreme events such as heat waves and extreme precipitation in a future climate, how well WRF predicts the extreme events (by comparing to observations) and how much improvement can be gained from the high resolution downscaling was first evaluated.

5.7.1 Evaluations of heat wave intensity, duration and frequency

Three key parameters of heat waves at an annual basis were used: intensity, duration and frequency. Heat wave intensity (ºC) is defined as the highest three continuous nighttime minima [*Karl and Knight*, 1997]. Heat wave duration (number of days during a heat wave) and frequency (number of heat wave events per year) are based upon two thresholds, T1 and T2, of daily maximum temperature. A heat wave was defined as the longest continuous period satisfying three criteria: a) the maximum daily temperature remained T1 or higher for at least three continuous days, b) the mean daily maximum temperature is higher or equal to T1, and c) in each day, the daily maximum temperature is no lower than T2 [*Huth et al.*, 2000; *Meehl and Tebaldi*, 2004]. T1 and T2 are taken as the 97.5^{th} and 81^{st} percentiles [*Huth et al.*, 2000] of daily maximum temperature at present climate (2001-2004) based on previous studies. Considering model dependency of these percentiles, the thresholds were applied to CESM, WRF and NCDC observational data, respectively. In other words, the same percentile thresholds (97.5^{th}

and 81st) in these three datasets correspond to different temperatures. For future heat waves in CESM and WRF simulations, the same temperature thresholds as present climate were retained in order to characterize the changes between the present and future climate.

The heat wave parameters were first evaluated for each year, and then the four year (2001-2004) mean was calculated and used in the following analysis. The heat wave intensity, duration and frequency were calculated from CESM outputs, WRF outputs and NCDC data. The evaluations were based on the NCDC observations covering 23 states in the Eastern US and all the 1098 observational sites (Figure 5.1) were used for point-point comparisons. Heat waves at each point in the NCDC network and the corresponding grid in CESM/WRF were determined separately. State means were then calculated are compared in Table 5.1. The 23 states can be divided into three regions (shown in Figure 5.1): Northeast, Eastern Midwest and Southeast. The regional mean evaluations are bolded in Table 5.1.

Following each of the regional means is the evaluation for the states belonging to the region. A t-test (α=0.05) was performed to determine the statistical significance of the improvement in WRF over CESM. From Table 5.1, there are 16 and 14 states showing statistically significant improvement for heat wave intensity and duration, respectively. However, only 6 states show statistical improvement for heat wave events, mainly due to the small number of heat wave events. Among the states with statistically significant improvement in WRF over CESM, the greatest improvements include: heat wave intensity in Florida (97%), heat wave duration in Maryland (91%) and heat wave frequency in Kentucky (98%). For those states that CESM achieves lower bias than WRF (marked with underline), the performance differences between CESM and WRF are not statistically significant. Thus, by taking advantage of high resolution topography and land use information, dynamical downscaling statistically improves, or at least performs similarly to, CESM for the heat wave predictions over the Eastern US.

Table 5.1 Evaluations of heat wave intensity, duration and frequency

	Heat wave intensity (ºC)				Heat wave duration (days/event)				Heat wave frequency (events/year)			
Regions/States	NCDC	CESM-NCDC	WRF-NCDC	%[1]	NCDC	CESM-NCDC	WRF-NCDC	%[1]	NCDC	CESM-NCDC	WRF-NCDC	%[1]
Northeast Region	**20.82**	**1.55**	**1.17**	**25**	**5.62**	**1.27**	**-0.41**	**68**	**1.44**	**-0.76**	**-0.29**	**62**
New Hampshire	19.22	2.21	1.91	14	5.42	-0.09	-1.01	91	1.53	-1.05	-0.35	67*
Vermont	19.23	1.30	1.49	13	6.20	1.36	-0.83	39	1.41	-0.91	-0.44	52
Massachusetts	21.70	2.33	0.99	58*	5.28	0.70	-0.46	34*	1.26	-0.34	-0.27	21
Connecticut	21.28	1.44	0.99	31	5.55	-1.10	-1.07	3	1.41	-0.66	-0.27	59
New York	20.16	1.12	0.78	30*	5.97	-0.73	-0.59	19*	1.49	-0.91	-0.57	37*
Pennsylvania	19.93	1.65	1.01	39*	5.92	1.53	-1.13	26*	1.5	-0.71	-0.17	76*
New Jersey	22.17	1.75	1.48	15	5.47	0.73	-0.15	79	1.45	-0.93	-0.22	76*
Maryland	23.24	1.01	1.50	33	6.27	4.34	-0.40	91*	1.36	-0.53	-0.14	74
West Virginia	20.43	1.18	0.38	68*	4.50	4.66	1.96	58*	1.54	-0.78	-0.15	81*
Eastern Midwest Region	**21.31**	**2.51**	**1.15**	**54**	**5.00**	**3.98**	**1.24**	**69**	**1.42**	**-0.23**	**-0.20**	**13**
Wisconsin	20.86	2.21	1.04	53*	5.13	2.97	1.18	60*	1.31	-0.26	-0.39	33
Michigan	20.18	2.47	1.93	22*	4.92	3.00	1.14	62*	1.4	-0.08	-0.07	13
Illinois	22.46	3.36	1.23	63*	4.97	5.30	1.25	76*	1.43	-0.24	-0.15	38
Indiana	21.94	2.53	0.89	65*	5.00	5.95	1.29	78*	1.51	-0.48	-0.21	56
Ohio	21.12	1.98	0.68	66*	4.98	2.70	1.36	50*	1.44	-0.09	-0.18	50
Southeast Region	**22.58**	**1.47**	**0.83**	**43**	**6.51**	**3.67**	**1.98**	**46**	**1.34**	**-0.34**	**-0.24**	**28**
Kentucky	22.28	1.82	0.57	69*	6.56	6.15	1.93	69*	1.26	-0.45	-0.01	98*
Virginia	20.98	2.17	1.28	41*	6.20	3.50	2.13	39*	1.33	-0.39	-0.19	51
Tennessee	22.08	1.62	0.93	43*	6.59	5.97	3.16	47*	1.26	-0.26	-0.21	19
North Carolina	21.61	1.69	1.09	36*	6.82	1.90	0.93	51*	1.36	-0.2	-0.22	9
Mississippi	23.18	1.66	0.79	52*	5.86	4.46	3.55	20	1.4	-0.33	-0.39	15
Alabama	22.78	1.04	1.10	5	5.06	3.53	2.34	34	1.47	-0.59	-0.49	17
Georgia	22.10	1.11	1.06	5	7.63	2.76	0.81	71	1.12	-0.09	-0.1	10
South Carolina	23.04	1.03	0.71	31*	7.78	3.76	1.43	62	1.18	-0.35	-0.08	77
Florida	25.15	1.13	-0.03	97*	6.05	1.04	1.58	34	1.64	-0.37	-0.48	23

[1]Numbers without underline: indicating bias percentage improvement in WRF over CESM in comparison to NCDC data, with formula of (|CESM-NCDC|-|WRF-NCDC|)/|CESM-NCDC|.
Numbers with underline: indicating bias in CESM is smaller than WRF in comparison to NCDC, with formula of (|WRF-NCDC|-|CESM-NCDC|)/|WRF-NCDC|.
*Statistical significance of t-test (α=0.05).

5.7.2 Evaluations of precipitation and extreme precipitation

A rainy day is defined as a day when the daily precipitation totals at least 1 mm [*Salinger and Griffiths*, 2001]. In the current analysis, extreme precipitation is defined as the 95th percentile of all the rainy days [*Diffenbaugh et al.*, 2006; *Salinger and Griffiths*, 2001]. The 95th percentile threshold is calculated as the mean of each year's 95th percentile precipitation from 2001 to 2004 [*Bell et al.*, 2004; *Diffenbaugh et al.*, 2006]. The determination of 95th percentile threshold is location dependent, so no fixed value is used in this definition. The following indices were used for the evaluations:

- Total extreme precipitation (mm/year): Annual total of extreme daily precipitation amounts

- Annual extreme events (days/year): Total annual extreme precipitation days
- Daily extreme precipitation (mm/day): Total amount of annual extreme precipitation divided by total annual extreme precipitation days.

The probability distributions of precipitation on rainy days are shown in Figure 5.3 for each of the 23 states in the Eastern US. In addition, the probability distributions of daily precipitation 40 mm or more is magnified and plotted in the middle of each plot. The value of 40 is significant because in the majority of the states, daily precipitation values of 40 mm or more account for less than 5% of rainy days, which is considered extreme precipitation. Annual extreme precipitation totals were also evaluated and listed in the upper portion of each plot.

WRF-simulated precipitation probability distributions are in closer agreement with NCDC observations than CESM (Figure 5.3). The CESM tends to yield larger percentages of rainy days with daily precipitation from 1-5 mm, but lower percentages with daily precipitation of 10 mm or more. The probability distributions of extreme precipitation in WRF agree more closely with NCDC data, while CESM data substantially underestimate the frequency of extreme precipitation. In the Northeast, six states (Massachusetts, New York, Pennsylvania, New Jersey, Maryland and West Virginia) have improvement over 70% in both total extreme precipitation and extreme precipitation days in WRF over CESM. Three states in the Eastern Midwest (Wisconsin, Illinois and Indiana) and five states in the Southeast (Kentucky, Virginia, North Carolina, Georgia and South Carolina) have similarly high improvement in WRF over CESM. However, a few exceptions exist. For instance, WRF over predicts extreme precipitation in New Hampshire and Connecticut, and the amount by which precipitation is over predicted is larger than the under predicted amount in CESM. In parts of the Southeast, such as in Florida, both CESM and WRF under predict the extreme precipitation, but WRF tends to capture more extreme events. This phenomenon indicates that dynamical downscaling with WRF has the capability of predicting extreme precipitation better than

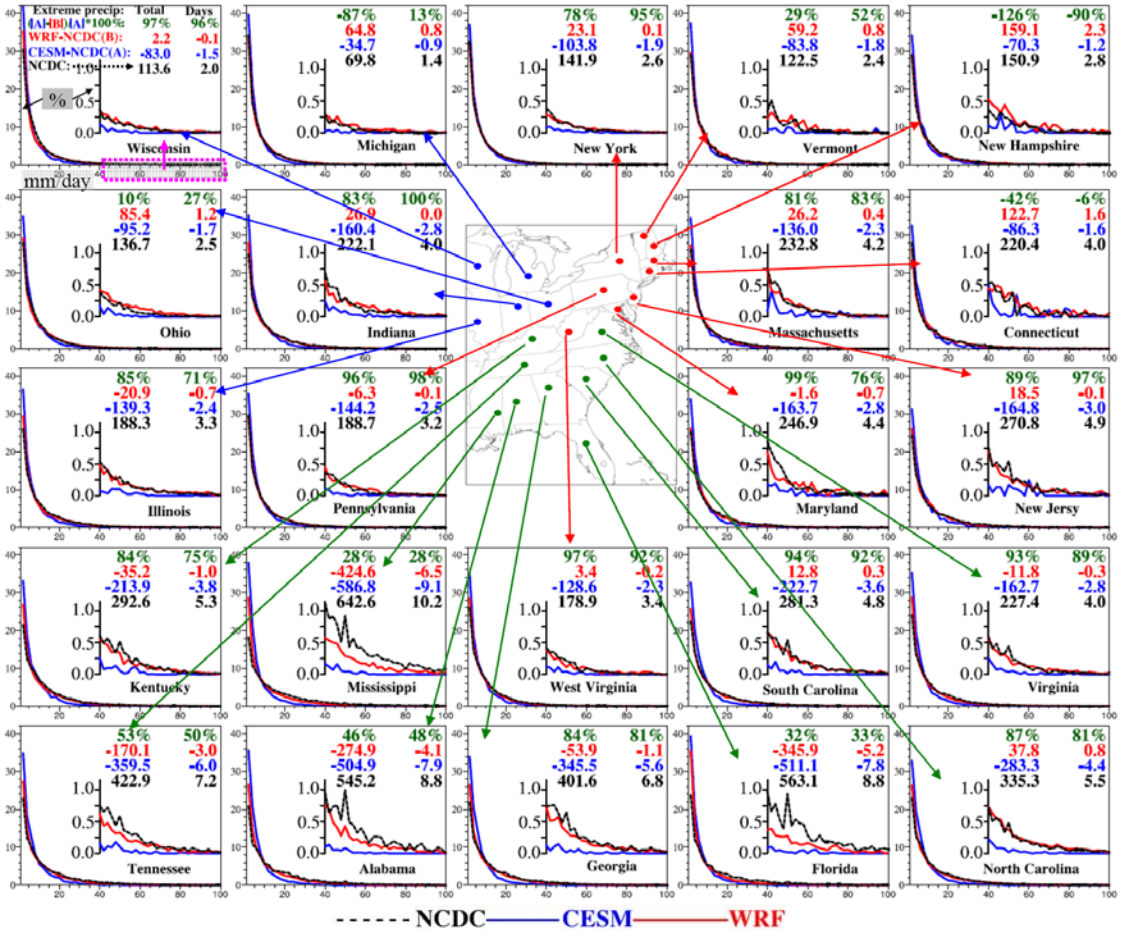

Figure 5.3 Probability distributions of precipitation from NCDC, CESM and WRF outputs. The probability distributions of daily precipitation 40 mm or more (extreme precipitation) is zoomed in and plotted in the middle of each plot. Total annual extreme precipitation amounts and days were listed in the upper portion of each plot. The numbers on the left represent total annual extreme precipitation, with NCDC in black, bias in CESM (CESM-NCDC) in blue, bias in WRF (WRF-NCDC) in red and the bias reduction in WRF over CESM ((|CESM-NCDC|-|WRF-NCDC|)/(|CESM-NCDC|)*100%, in green); The numbers on the right are similar to the left but apply to the annual extreme precipitation days.

CESM. However, more than 20 hurricane events* occurred during 2001-2004, which is possibly not captured well by either CESM or WRF, resulting in less extreme precipitation events in both models compared to NCDC. Overall, 32-33% improvement was achieved in WRF downscaled outputs.

5.8 Increasing trends of state-level extreme events by the end of 2050s

5.8.1 Increasing trends of heat wave intensity, duration and frequency

The spatial distributions of heat wave intensity, duration and frequency at present (2001-2004) and future climate (RCP 8.5, 2057-2059) are shown in Figure 5.4 and the Region/State means are shown in Table 5.2.

Figure 5.4(a) shows, at present, the heat wave intensity is higher in the Southeast (mostly higher than 23 ºC) than the Northeast and the Eastern Midwest. A few hot spots, indicating higher heat wave intensity, are located in the megacities, such as Chicago and Detroit in the Eastern Midwest, Washington D.C., Philadelphia and New York City in the Northeast, Memphis and Atlanta in the Southeast. By the end of 2050s (2057-2059), the severity of heat waves increases in most of the areas in the Eastern US (Figure 5.4(b) and (c)). Again, the Southeast still shows highest intensity; however, the highest increase occurs in the Northeast (Figure 5.4(c)), reaching 3 to 5 ºC, pushing the Northeast to the current conditions in the Southeast. In the Northeast, six states (New Hampshire, Vermont, New York, Pennsylvania, New Jersey and Maryland) have an increase of higher than 3 ºC, with the highest increase occurring in the state of New York.

Figure 5.4(d) shows, at present, the heat wave duration is similar in the Northeast and Eastern Midwest, about 4 days/event, while in Southeast it could reach more than 7 days/event. By the end of 2050s, the heat wave duration decreases in the center areas (Tennessee, Mississippi and Alabama) of Southeast, while the Northeast and Eastern Midwest show an increase of 2 days per event on average (Figure 5.4(e) and (f)). There

* http://en.wikipedia.org/wiki/List_of_Florida_hurricanes_%282000%E2%80%93present%29#2001

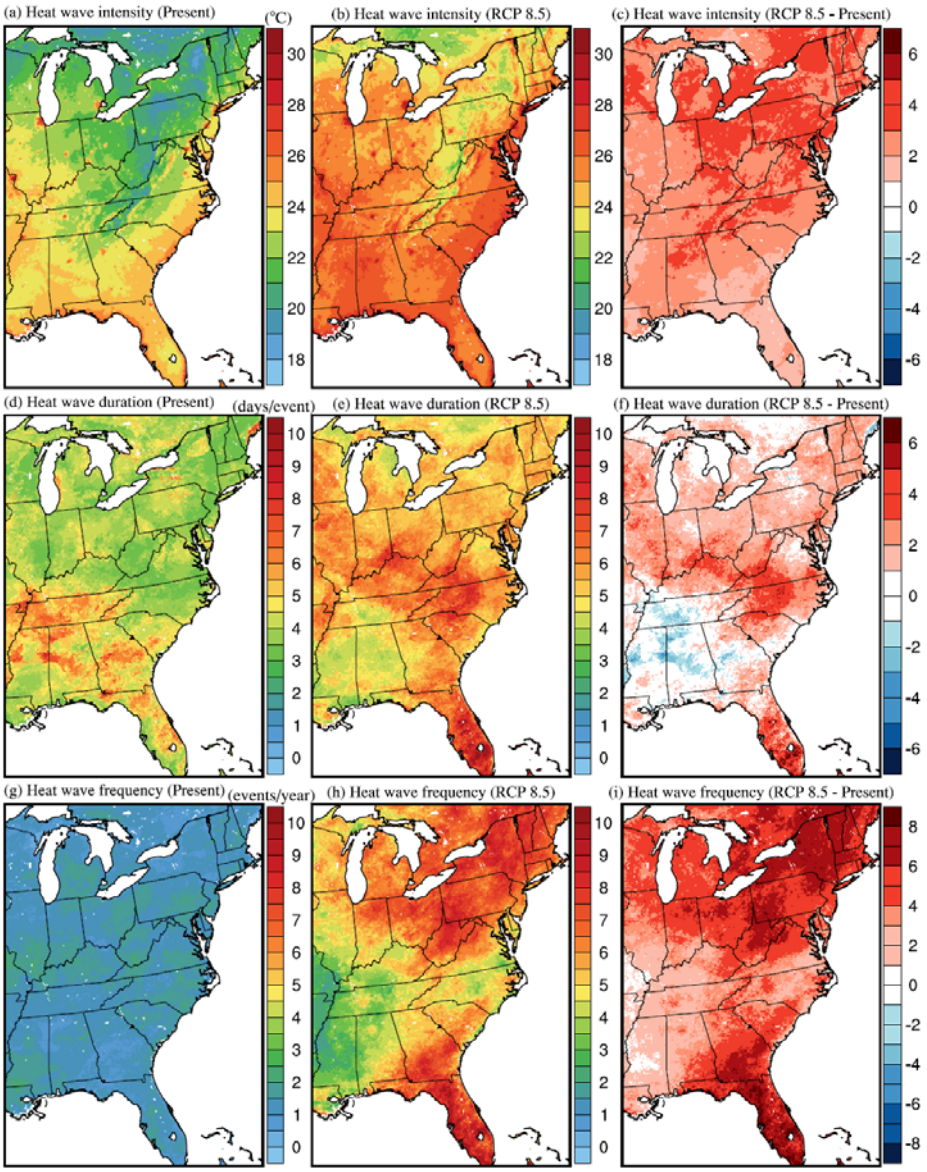

Figure 5.4 The spatial distributions of heat wave intensity, duration and frequency at present (2001-2004) and future climate (RCP 8.5, 2057-2059): (a) four year average of heat wave intensity at present climate (2001-2004), (b) three year average of heat wave intensity at future climate under RCP 8.5, (c) the differences of heat wave intensity between RCP 8.5 and present climate (RCP 8.5 – present climate), (d) , (e) and (f) are similar as (a), (b) and (c), but applies to heat wave duration, (g), (h) and (i) are similar as (a), (b) and (c) as well, but applies to heat wave frequency.

is about 1 event per year at present from Figure 5.4(g), while 5 or more events could occur in the Northeast, Eastern Midwest and Florida by the end of the 2050s under the RCP 8.5 scenario (Figure 5.4(h) and (i)). Combining the heat wave durations, the total heat wave days in the Northeast and Eastern Midwest would be higher than Southeast.

Table 5.2 Heat wave intensity, duration and frequency

	Heat wave intensity (ºC)			Heat wave duration (days/event)			Heat wave frequency (events/year)		
Regions/States	Present	RCP 8.5	RCP 8.5 - Present	Present	RCP 8.5	RCP 8.5 - Present	Present	RCP8.5	RCP 8.5 - Present
Northeast Region	**21.81**	**24.85**	**3.05**	**3.61**	**5.53**	**1.92**	**1.24**	**7.03**	**5.79**
New Hampshire	21.16	24.23	3.07	3.22	5.35	2.13	1.29	7.41	6.12
Vermont	20.84	24.02	3.18	3.37	5.35	1.98	1.15	7.94	6.79
Massachusetts	22.21	25.05	2.84	3.60	5.47	1.87	1.02	7.13	6.11
Connecticut	22.45	25.43	2.98	3.68	5.71	2.03	1.24	6.53	5.29
New York	20.84	24.08	3.24	3.78	5.32	1.54	0.96	7.65	6.69
Pennsylvania	20.97	24.16	3.19	3.85	5.48	1.63	1.33	7.26	5.93
New Jersey	23.44	26.55	3.11	3.59	5.49	1.90	1.36	6.26	4.90
Maryland	23.26	26.33	3.07	3.91	5.67	1.76	1.34	5.89	4.55
West Virginia	21.08	23.82	2.74	3.53	5.96	2.43	1.45	7.16	5.71
Eastern Midwest Region	**22.26**	**25.05**	**2.78**	**3.86**	**5.65**	**1.78**	**1.23**	**5.57**	**4.34**
Wisconsin	21.63	24.61	2.98	3.64	5.63	1.99	0.97	5.23	4.26
Michigan	21.70	24.62	2.92	3.96	5.00	1.04	1.20	5.78	4.58
Illinois	23.48	25.74	2.26	3.97	5.94	1.97	1.32	4.50	3.18
Indiana	22.72	25.28	2.56	3.87	5.87	2.00	1.37	5.66	4.29
Ohio	21.79	24.99	3.20	3.88	5.80	1.92	1.30	6.70	5.40
Southeast Region	**23.53**	**25.99**	**2.46**	**4.55**	**5.78**	**1.23**	**1.25**	**5.02**	**3.77**
Kentucky	22.80	25.54	2.74	4.22	6.28	2.06	1.41	4.48	3.07
Virginia	22.50	25.43	2.93	3.70	6.00	2.30	1.38	5.38	4.00
Tennessee	23.00	25.69	2.69	5.47	5.46	-0.01	1.16	3.88	2.72
North Carolina	23.27	26.06	2.79	3.82	6.45	2.63	1.35	4.71	3.36
Mississippi	23.99	26.21	2.22	4.70	4.41	-0.29	1.35	2.93	1.58
Alabama	23.80	26.34	2.54	4.96	4.57	-0.39	1.12	4.33	3.21
Georgia	23.74	25.92	2.18	4.98	5.66	0.68	1.02	6.19	5.17
South Carolina	23.98	26.32	2.34	4.41	6.08	1.67	1.33	5.46	4.13
Florida	24.67	26.38	1.71	4.66	7.11	2.45	1.09	7.81	6.72

5.8.2 Increases in the state-level extreme precipitation

At present (Figure 5.5(a) and Table 5.3), the total extreme precipitation in the Northeast and Southeast is larger than the Eastern Midwest. The highest annual extreme precipitation, 371.0 mm, occurs in Connecticut. By the end of 2050s, while scattered decreases in extreme precipitation exist, most areas show increasing patterns, as seen in Figure 5.5(b) and (c). As shown in Figure 5.5(c), the largest increase (dark green) takes place mainly in the coastal states, including New Hampshire, New Jersey, North Carolina, South Carolina, Georgia and Alabama, with an increase of around 150 mm/year

(Table 5.3). From Table 5.3, almost half of the states have a total extreme precipitation increase of more than 35%, including five states in the Northeast (New Hampshire, Vermont, Massachusetts, New Jersey and Maryland), two in the Eastern Midwest (Illinois and Indiana) and four in the Southeast (North Carolina, Alabama, Georgia and South Carolina). However, some inland regions show decreasing extreme precipitation (Figure 5.5(c), including part of New York, Pennsylvania, Ohio and West Virginia, Illinois, and Tennessee. Wisconsin is the only state with overall decreasing mean extreme precipitation by the end of 2050s (18.3 mm less per year from Table 5.3).

Daily extreme precipitation ranges from 40 to 60 mm/day at present (Figure 5.5(d)). By the end of 2050s (Figure 5.5(e) and (f)), smaller increases occur in the Northeast and Eastern Midwest, while larger increases occur in the Southeast. As shown in Figure 5.5(c) and (f)), the Southeast has the largest increase in both daily extreme precipitation and annual extreme precipitation days, while the Eastern Midwest shows less increase. At present, about 4 to 6 days have extreme precipitation (Figure 5.5(g)), while 8 to 12 days could occur in large areas of the Northeast and Southeast by the end of 2050s (Figure 5.5(h)), indicating the extreme precipitation days could increase to twice as many as present conditions (Figure 5.5(i)).

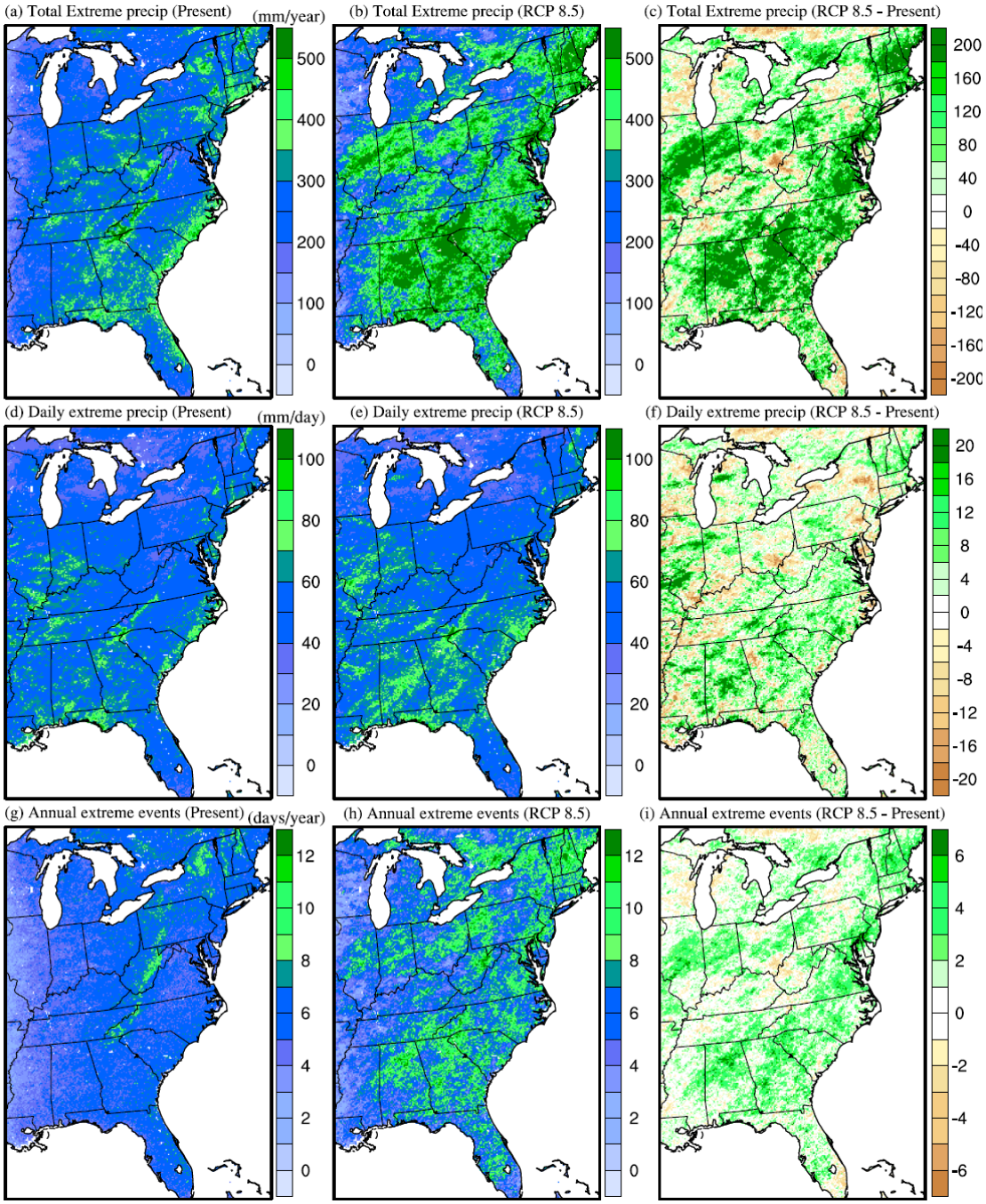

Figure 5.5 The spatial distributions of total extreme precipitation, daily extreme precipitation and annual extreme events at present (2001-2004) and future climate (RCP 8.5, 2057-2059)

Table 5.3 Total extreme precipitation, daily extreme precipitation and annual extreme events

	Total extreme precipitation (mm/year)			Daily extreme precipitation (mm/day)			Annual extreme events (days/year)		
Regions/States	Present	RCP8.5	RCP 8.5 - Present	Present	RCP8.5	RCP 8.5 - Present	Present	RCP8.5	RCP 8.5 - Present
Northeast Region	**308.7**	**416.1**	**107.3**	**51.1**	**52.6**	**1.5**	**6.1**	**7.9**	**1.8**
New Hampshire	324.4	537.6	213.3	49.7	55.7	6.0	6.5	9.6	3.1
Vermont	286.2	415.7	129.5	43.1	46.7	3.6	6.5	8.8	2.2
Massachusetts	328.5	454.3	125.8	54.5	56.7	2.1	6.1	8.1	2.1
Connecticut	371.0	444.3	73.3	61.4	60.7	-0.8	6.2	7.4	1.3
New York	292.5	332.5	40.0	45.7	44.9	-0.8	6.4	7.4	1.0
Pennsylvania	290.8	359.8	69.0	47.9	49.6	1.6	6.1	7.3	1.2
New Jersey	307.7	458.4	150.7	57.8	56.9	-0.9	5.4	8.1	2.8
Maryland	272.9	402.3	129.3	52.9	54.3	1.4	5.2	7.5	2.3
West Virginia	304.8	339.5	34.8	46.7	48.3	1.5	6.6	7.2	0.6
Eastern Midwest Region	**235.2**	**293.8**	**58.7**	**50.6**	**52.0**	**1.5**	**4.7**	**5.6**	**0.9**
Wisconsin	182.9	164.7	-18.3	44.5	43.5	-1.0	4.0	3.8	-0.2
Michigan	217.8	254.0	36.1	42.1	44.2	2.2	5.2	5.8	0.6
Illinois	208.0	322.9	114.9	55.6	60.0	4.4	3.7	5.3	1.6
Indiana	277.8	386.8	109.1	58.5	60.1	1.7	4.8	6.5	1.7
Ohio	289.3	340.8	51.5	52.1	52.3	0.2	5.6	6.6	1.1
Southeast Region	**294.6**	**405.0**	**110.4**	**56.8**	**60.6**	**3.9**	**5.2**	**6.7**	**1.5**
Kentucky	287.6	329.8	42.3	55.6	57.3	1.7	5.2	5.8	0.5
Virginia	262.0	388.2	126.3	50.2	54.5	4.4	5.2	7.1	1.9
Tennessee	293.2	365.7	72.5	57.8	59.4	1.6	5.1	6.2	1.1
North Carolina	338.1	477.7	139.6	59.3	64.6	5.3	5.7	7.4	1.7
Mississippi	226.0	286.8	60.8	57.4	60.4	3.0	4.0	4.8	0.8
Alabama	288.7	458.1	169.4	58.5	65.5	7.0	5.0	7.1	2.1
Georgia	330.4	490.7	160.4	59.3	63.6	4.3	5.6	7.8	2.2
South Carolina	323.1	482.4	159.4	57.9	62.9	5.0	5.6	7.7	2.1
Florida	302.1	365.4	63.3	55.0	57.7	2.7	5.6	6.4	0.8

In addition to the extreme precipitation days, the percentage change of annual extreme precipitation to annual total precipitation was also compared and listed in Table 5.4. At present, the extreme precipitation accounts for 25% (West Virginia) to 30% (Wisconsin) of annual total precipitation; by the end of 2050s, these percentage ranges from 27% in West Virginia to 39% in Illinois, with a mean increase of 7% across the Eastern US. The three largest increases (more than 10%) occur in New Hampshire (13%), Alabama (12%) and Illinois (11%). At present, Wisconsin has the largest percentage in extreme precipitation (30%). However, it is the only state that is projected to have a slight decrease in extreme precipitation percentage (about 1%), while all other states show increasing trends in extreme precipitation percentage (3% to 13%).

Table 5.4 Percentage change of annual extreme precipitation to annual total precipitation

	95% precip/total precip Present	95% precip/total precip RCP8.5	95% precip/total precip RCP 8.5 -Present
Northeast Region	**26%**	**33%**	**7%**
New Hampshire	26%	39%	13%
Vermont	25%	35%	10%
Massachusetts	26%	35%	8%
Connecticut	26%	32%	6%
New York	26%	30%	4%
Pennsylvania	25%	29%	4%
New Jersey	26%	35%	9%
Maryland	27%	34%	7%
West Virginia	25%	27%	3%
Midwest Region	**27%**	**33%**	**5%**
Wisconsin	30%	29%	0%
Michigan	27%	31%	4%
Illinois	28%	39%	11%
Indiana	27%	34%	7%
Ohio	26%	29%	4%
Southeast Region	**26%**	**34%**	**8%**
Kentucky	26%	31%	5%
Virginia	26%	34%	8%
Tennessee	27%	32%	6%
North Carolina	26%	33%	7%
Mississippi	27%	36%	9%
Alabama	26%	38%	12%
Georgia	27%	35%	8%
South Carolina	26%	33%	8%
Florida	28%	34%	6%

5.9 Increasing trends of city-level extreme weather events

5.9.1 Increasing trends of heat wave intensity, duration and frequency

In addition to the state-level heat wave studies, city-level heat waves were also explored. Among the top 50 cities by population in US, 20 cities are located in the eastern

US*, and the locations for each city are shown in Figure 5.6. Among the 20 cities, most of them have areas greater or equal to 400 km^2. To reduce single grid bias in WRF and also match CESM grids, 25 (5 x 5) WRF grid cells centered at the city and all the NCDC data in this region were used. The evaluations and future change of heat wave intensity, duration and frequency of the 20 cities are listed in Table 5.5. Heat waves in each city were determined with NCDC, CESM and WRF data (both present and future climate for model simulations) using the same criteria as in the state level analysis. The underlined numbers indicate that WRF did not perform as well as CESM in comparison to NCDC. Overall, after downscaling, most of the cities show improvement in heat wave reproducing, and the mean improvement in the 20 cities is 21%, 71% and 57% for heat wave intensity, duration and frequency, respectively. In future (RCP 8.5, 2057-2059), widespread increase occurs in all of these major cities in the eastern US, from 1.81 ºC to 3.71 ºC with a mean of 3.10 ºC for heat wave intensity, from 0.09 days/event to 4.25 days/event with a mean of 1.85 days/event for heat wave duration, and from 1.70 events/year to 7.55 events/year with a mean of 4.38 events/year for heat wave frequency.

Figure 5.6 Top 20 cities by population in Eastern US

* http://en.wikipedia.org/wiki/List_of_United_States_cities_by_population

Table 5.5 Heat wave intensity, duration and frequency in top 20 cities by population in Eastern US

	Heat wave intensity (ºC)				Heat wave duration (days/event)				Heat wave frequency (events/year)			
City	NCDC	CESM	WRF[1]	WRF[2]	NCDC	CESM	WRF[1]	WRF[2]	NCDC	CESM	WRF[1]	WRF[2]
New York	24.75	23.25	24.92	3.58	3.00	4.00	3.62	1.82	1.38	0.56	1.35	4.07
Chicago	24.80	25.05	26.20	3.34	3.67	4.25	3.60	1.37	1.25	1.5	1.15	5.05
Philadelphia	23.17	22.22	24.31	3.69	3.00	9.00	3.18	2.42	1.50	0.25	1.64	4.63
Jacksonville	24.91	26.75	25.02	1.81	3.88	6.75	4.57	1.60	1.50	1.00	1.08	5.28
Indianapolis	23.50	24.54	23.04	3.03	4.71	4.00	4.04	1.84	1.88	0.81	1.18	4.35
Columbus	21.75	23.54	21.94	3.63	4.74	3.67	3.61	2.55	1.46	1.50	1.36	5.03
Charlotte	22.81	24.00	22.96	2.62	5.00	5.83	3.75	4.25	1.25	1.00	1.29	3.30
Detroit	21.67	23.30	24.25	3.67	5.25	4.00	3.67	1.39	1.50	1.00	1.41	4.70
Memphis	25.37	25.75	25.07	2.18	6.67	9.50	5.52	0.09	1.50	1.25	1.14	1.70
Baltimore	23.85	23.17	23.99	3.65	4.67	4.33	3.46	1.95	1.13	0.88	1.44	5.09
Boston	22.29	24.87	23.06	3.41	3.00	6.35	3.55	1.27	1.22	1.16	1.16	5.22
Washington, D.C.	23.96	23.86	24.33	3.55	4.67	4.33	4.11	1.43	1.25	1.00	1.29	4.70
Nashville	22.54	24.32	23.46	3.21	6.75	6.50	5.26	0.19	1.15	1.20	1.14	2.46
Louisville	22.14	24.08	23.63	2.98	4.00	5.00	3.75	2.73	1.00	0.67	1.66	3.13
Milwaukee	21.51	22.01	23.18	3.51	4.30	6.00	3.76	0.95	1.47	1.08	1.10	4.70
Virginia Beach	24.53	26.83	24.85	2.10	3.00	5.67	3.08	1.80	1.00	1.00	0.44	5.14
Atlanta	22.22	22.80	23.83	3.08	5.25	5.50	4.66	0.72	1.00	1.25	1.19	3.69
Raleigh	22.93	24.43	23.54	2.89	3.00	4.95	3.25	3.27	1.75	1.92	1.53	2.46
Miami	27.41	27.53	26.05	2.40	3.00	3.00	3.91	3.72	1.75	1.00	0.85	7.55
Cleveland	22.59	21.60	23.04	3.71	3.50	6.25	3.83	1.73	1.17	1.25	1.20	5.25

[1]The numbers in this column indicate present period (2001-2004) from WRF simulations. Values without (with) underline indicate absolute bias in WRF is smaller (larger) than CESM in comparison to NCDC data.
[2]The numbers in this column indicate the heat wave increase of future climate period (2057-2059) in RCP 8.5 in comparison to present climate (2001-2004).

5.9.2 Wide increases in the city-level extreme precipitation

The evaluations and future change of extreme precipitation of the 20 cities are listed in Table 5.6. After downscaling, WRF simulated total annual extreme precipitation in 11 cities shows lower biases than CESM when compared to NCDC data. However, the daily extreme precipitation and annual total precipitation days show much higher improvement in WRF. In particular, the annual total precipitation days in WRF (mean bias = -0.1 days/year) perform much better than CESM (mean bias = 2.6 days/year) in all the 20 cities. By the end of the 2050s, the annual total extreme precipitation in most of the cities are projected to increase, and four of them have increases over 200.0 mm/year, with the

highest increase in Philadelphia (315.1 mm), followed by Baltimore(227.3 mm), Virginia Beach (210.7 mm) and Boston (207.4 mm). The annual total precipitation in Philadelphia and Baltimore is primarily due to the increase of frequency of extreme precipitation. In Boston, it is due to the increase of both annual extreme precipitation days and daily mean extreme precipitation. In Virginia Beach, the increase mainly comes from the daily extreme precipitation. Among the 20 cities, 8 cities (Philadelphia, Indianapolis, Columbus, Charlotte, Baltimore, Boston Washington, D.C., Milwaukee) are projected to have at least 2 days increase per year in extreme precipitation in future climate, and three cities (New York, Chicago and Detroit) have at least 1 day increase. On the contrary, a few states in the Southeast, including Jacksonville, Miami and Nashville, are projected to have less annual extreme precipitation, which could be related to the secondary organic aerosol (SOA), and more studies are needed to evaluate the causes.

Table 5.6 Total extreme precipitation, daily extreme precipitation and annual extreme events in top 20 cities by population in Eastern US

	Total extreme precipitation (mm/year)				Daily extreme precipitation (mm/day)				Annual extreme events (days/year)			
City	NCDC	CESM	WRF[1]	WRF[2]	NCDC	CESM	WRF[1]	WRF[2]	NCDC	CESM	WRF[1]	WRF[2]
New York	319.6	283.1	309.1	82.5	56.5	35.8	59.0	6.2	5.8	8.0	5.3	1.0
Chicago	240.0	186.4	224.0	121.7	46.1	27.7	51.7	9.9	5.3	6.8	4.5	1.3
Philadelphia	320.1	250.6	300.2	315.1	50.5	32.7	56.3	-0.5	6.3	7.5	5.3	5.8
Jacksonville	304.9	297.0	438.5	-36.2	57.1	31.2	65.2	2.5	5.7	9.5	6.6	-0.5
Indianapolis	281.2	227.8	319.3	168.8	52.5	32.3	64.4	0.1	5.3	7.1	5.1	2.8
Columbus	232.3	241.0	259.8	130.1	43.0	32.3	47.7	2.8	5.4	7.4	5.4	2.3
Charlotte	284.1	245.9	271.7	115.3	54.9	31.3	49.7	1.7	5.2	7.9	5.4	2.1
Detroit	184.6	186.5	263.8	65.5	32.4	25.1	46.0	-0.6	5.8	7.5	5.9	1.3
Memphis	333.8	254.5	239.5	2.4	74.0	30.7	62.7	-6.3	4.3	8.3	3.9	0.2
Baltimore	292.9	275.5	297.2	227.3	47.5	34.3	58.5	1.5	6.0	8.0	5.1	4.1
Boston	297.7	256.5	302.7	207.4	54.0	37.4	50.3	9.3	5.6	7.0	6.1	2.5
Washington, D.C.	279.1	275.3	257.7	170.1	47.9	32.4	49.8	1.4	5.8	8.5	5.1	3.2
Nashville	348.1	252.2	299.6	-10.0	60.0	31.8	64.2	-2.5	5.8	7.9	4.8	0.1
Louisville	253.1	262.6	267.3	75.6	54.6	34.7	52.0	2.3	4.5	7.7	5.2	0.8
Milwaukee	212.6	171.4	222.4	120.7	42.7	25.5	44.4	4.1	4.9	6.6	5.0	2.1
Virginia Beach	290.8	239.9	316.7	210.7	49.8	29.3	63.1	29.7	5.8	8.3	4.8	0.5
Atlanta	342.8	280.9	370.3	22.8	63.0	29.6	66.5	0.8	5.4	9.5	5.7	0.2
Raleigh	253.3	244.4	316.8	58.4	53.7	30.0	61.1	5.1	4.8	8.4	5.3	0.5
Miami	245.9	282.8	197.1	-17.9	57.1	25.0	39.8	9.7	4.5	11.4	4.9	-1.2
Cleveland	225.4	199.2	286.9	37.4	35.8	27.5	48.4	-0.1	6.3	7.3	5.9	0.9

[1]The numbers in this column indicate present period (2001-2004) from WRF simulations. Values without (with) underline indicate absolute bias in WRF is smaller (larger) than CESM in comparison to NCDC data.
[2]The numbers in this column indicate the precipitation increase of future climate period (2057-2059) in RCP 8.5 in comparison to present climate (2001-2004).

5.10 Statistical justification in downscaled climate outputs

Considering the computational limitations, only one member global climate output was downscaled. To achieve the statistical benefits, the standard deviation from ensemble CESM outputs was applied to the downscaled WRF outputs. The ensemble CESM standard deviations have been shown Figure A1 to A6 in the APPENDIX. The single member downscaled results were listed in Table 5.2 and Table 5.3. Combining the data in these two tables and the standard deviation in Figure A1-A6, the heat wave intensity was listed in Table 5.7 and heat wave duration, heave wave frequency, annual total extreme precipitation, daily mean extreme precipitation and annual extreme precipitation days ± one standard deviation were listed in Table A1 to Table A5 in the APPENDIX.

Table 5.7 Heat wave intensity ± one standard deviation

	Heat wave intensity (ºC)		
Regions/States	Present	RCP 8.5	RCP 8.5 - Present
Northeast Region	**21.81±0.31**	**24.85±0.34**	**3.05±0.39**
New Hampshire	21.16±0.36	24.23±0.29	3.07±0.28
Vermont	20.84±0.51	24.02±0.43	3.18±0.41
Massachusetts	22.21±0.06	25.05±0.36	2.84±0.19
Connecticut	22.45±0.18	25.43±0.32	2.98±0.31
New York	20.84±0.41	24.08±0.38	3.24±0.16
Pennsylvania	20.97±0.03	24.16±0.25	3.19±0.29
New Jersey	23.44±0.38	26.55±0.32	3.11±0.63
Maryland	23.26±0.57	26.33±0.34	3.07±0.82
West Virginia	21.08±0.29	23.82±0.32	2.74±0.55
Midwest Region	**22.26±0.88**	**25.05±0.51**	**2.78±0.59**
Wisconsin	21.63±0.79	24.61±0.59	2.98±0.65
Michigan	21.70±0.36	24.62±0.50	2.92±0.16
Illinois	23.48±1.37	25.74±0.57	2.26±0.97
Indiana	22.72±1.30	25.28±0.49	2.56±0.86

Ohio	21.79±0.57	24.99±0.38	3.20±0.30
Southeast Region	**23.53±0.35**	**25.99±0.25**	**2.46±0.42**
Kentucky	22.80±0.81	25.54±0.34	2.74±0.84
Virginia	22.50±0.46	25.43±0.26	2.93±0.65
Tennessee	23.00±0.67	25.69±0.36	2.69±0.72
North Carolina	23.27±0.31	26.06±0.27	2.79±0.45
Mississippi	23.99±0.38	26.21±0.24	2.22±0.16
Alabama	23.80±0.09	26.34±0.10	2.54±0.05
Georgia	23.74±0.16	25.92±0.16	2.18±0.18
South Carolina	23.98±0.18	26.32±0.32	2.34±0.42
Florida	24.67±0.13	26.38±0.22	1.71±0.32

CHAPTER VI

6 THE IMPACT OF HEAT WAVES ON AIR QUALITY IN THE UNITED STATES

6.1 Declaration

This chapter is a slightly revised version of a manuscript, to be submitted to a journal for publication.

6.2 Abstract

The statistical evaluation in this study showed strong confidence that the statistical metrics in retrospective studies can be applied to climate studies as benchmarks. Among all the metrics, MFB/MFE are the most useful ones, and particular for ozone, they almost all fall within the benchmarks. In future decades, even with large reductions of NMVOCs and NOx, the increase of methane emissions and increased boundary concentrations could enhance the formation of ozone particularly with high temperature intensification. This has been observed in RCP 8.5, in which ozone increases in western US. More intense heat waves that were projected in future climates, especially, in RCP 8.5, a mean increase of 54% and 313% for duration and frequency. During heat wave periods, in RCP 8.5, all regions show a higher percentage of MDA8 with levels over 75 ppb. More than 15% MDA8 were projected during the heat wave period than non-heat wave period in three regions (West, Southwest and West North Central). The mean MDA8 increase during heat wave period in RCP 8.5 is 3.1 to 9.5 ppbv in US. The $PM_{2.5}$ in the U.S. decreases 16% to 39% (for all 9 climate regions) in RCP 4.5 and 28% to 44% by the end of 2050s in RCP 8.5.

6.3 Introduction

The impact of climate change on air quality has been widely studied. Bell et al [2007] found under Intergovernmental Panel on Climate Change (IPCC) Special Report on Emissions Scenarios (SRES) A2 climate scenario, by keeping emissions as the present

condition, an average of 4.8 ppb, up to 9.6 ppbv, was projected to increase in summer daily 1-h maximum ozone by 2050s. They also found the mean number of days exceeding the maximum daily 8-h ozone (MDA8) standard increased by 68%. Nolte et al. [2008] found by 2050s, an overall of 2 to 5 ppbv increase of MDA8 in Texas and parts of the eastern U.S under A1B scenario while maintaining emissions at current level. Lam et al. [2011] found under A1B scenario, about 5 ppbv reduction was projected for MDA8 by 2050s due to the combined effect of climate change and emission reductions. Under A1FI with increased anthropogenic emissions, Huang et al. [2008] found in 2050s, that mean ozone concentrations increase +4% to +9% in majority of the areas in US, by using global chemistry model (Model for OZone And Related Chemical Tracers, MOZART).

To date, most studies focused on the IPCC SRES A1 and A2 scenarios [*Nakicenovic and Swart*, 2000]. However, for the upcoming Fifth Assessment Report (AR5) of the United Nations IPCC, the Coupled Model Intercomparison Project Phase 5 (CMIP5) ([*Taylor et al.*, 2009; *Taylor et al.*, 2012] 'representative concentration pathways* (RCPs [*Moss et al.*, 2010]) scenarios have been designed. Compared to SRES scenarios, these new RCP scenarios employ different emissions pathways [*Lamarque et al.*, 2011b]. The impact of climate on air quality under these plausible scenarios is one of the major focuses in AR5. Using global chemistry models, by the end of 21st century, the tropospheric ozone is projected to decrease in RCP 2.6, RCP 4.5 and RCP 6.0 [*Lamarque et al.*, 2011b], and increase in RCP 8.5 [*Kawase et al.*, 2011; *Lamarque et al.*, 2011b]. The regional scale studies on the RCP scenarios are very limited, i.e., by using A Unified Regional Air-quality Modelling System (AURAMS) on a 45 km by 45 km resolution, Kelly et al. [2012] found under A2 climate and RCP 6 emissions, almost entire US show decrease of ozone concentrations. It is believed that higher spatial resolution is necessary to achieve better regional scale climate and air quality [*Caldwell et al.*, 2009]. Thus, to address the issue, this study applies a dynamical downscaling technique from a global

*http://www.iiasa.ac.at/web-apps/tnt/RcpDb/dsd?Action=htmlpage&page=about

chemistry model to a high spatial resolution domain (12 km by 12 km continental US domain) under the new RCP scenarios.

In either global and regional climate studies, the evaluation of model results in were mainly on regional or monthly scales [*Lam et al.*, 2011; *Lamarque et al.*, 2010], and statistical evaluation was usually applied in the retrospective studies [*USEPA*, 2007]. By applying high resolution downscaling methodology in this study, one of the primary goals is to evaluate whether the evaluation method in the retrospective studies can be used in the climate quality studies. This could provide important benchmarks for future climate studies.

In the retrospective studies, the ozone and particulate matter (PM) levels have been investigated during extreme weather conditions - heat wave events. Stedman [2004] estimated, during the first two weeks of August 2003 in England and Wales, that an extra 21-38% (423 and 769 persons) excess deaths are associated with the elevated ambient ozone and PM_{10} concentrations. Vieno et al. [2010] found during 2003 heat waves, the first two weeks in August, an temperature increase of 5 ºC could increase up to 9 ppbv surface ozone at Writtle (70 km NE of London). In pure climate studies, more intense heat waves are likely to occur in the future climate [*Ganguly et al.*, 2009; *Gao et al.*, 2012; *Meehl and Tebaldi*, 2004]. Unlike the retrospective studies, in climate studies, its impact on air quality is usually compared among different emission scenarios. The impacts in different climate conditions (such as heat wave/non-heat wave period) under the same scenario are ignored. Thus, by using a high resolution downscaling system and comprehensive chemical model, in this study, the ozone concentrations during heat waves and non-heat wave periods under the same scenario were evaluated.

6.4 Model description and configuration

Global climate CESM and chemistry model CAM-Chem has been described in Section 2.2.1 and 2.2.2. Regional climate model WRF 3.2.1 and regional chemistry model CMAQ has been discussed in Section 2.2.3.3 and 2.2.4.

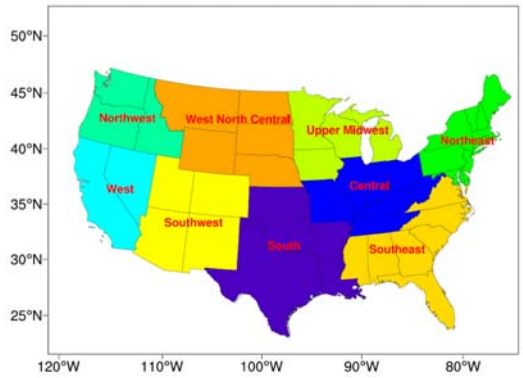

Figure 6.1 12 km by 12 km simulation domain with nine climate regions in U.S.

Figure 6.1 shows simulation domain with a spatial resolution of 12 km by 12 km, and it includes 9 climate regions based on National Climatic Data Center (NCDC)*. The 9 climate regions are the major focus in the following discussions. An outer domain of 36 km by 36 km was designed to achieve smoother downscaling from CESM to WRF, but not used for analysis.

For the CMIP5 [*Taylor et al.*, 2009; *Taylor et al.*, 2012], a total of four RCP scenarios (2005-2100), including RCP 2.6, RCP 4.5, RCP 6.0 and RCP 8.5, have been designed in addition to present climate (1850-2005). Considering the limitations of computational resources, two scenarios, RCP 4.5 and RCP 8.5, were selected in this study. The primary purposes of this selection are to evaluate and compare the climate and air quality under low to medium emission scenario (RCP 4.5 [*Smith and Wigley*, 2006; *Wise et al.*, 2009]) and fossil fuel intensive emission scenario (RCP 8.5 [*Riahi et al.*, 2007]). CAM-Chem was conducted from 2001 to the end of the century continuously on a global scale. After the global chemistry simulations, a four-year period (2001-2004) was selected to represent present climate and three year period (2057-2059) was used to illustrate future climate conditions. The selection of the present climate considers the closest climate period before the start of RCP scenarios (2005), while future climate in 2050s possibly

* http://www.ncdc.noaa.gov/temp-and-precip/us-climate-regions.php

captures enough climate change signal and also avoid the large uncertainties in projecting emission too far in future [*Nolte et al.*, 2008].

6.5 Dynamical downscaling

Dynamical downscaling is a technique that uses the outputs from GCMs to provide the initial and boundary conditions for the regional climate/chemistry models. The downscaling process involves species mapping, horizontal and vertical interpolations. The first step for downscaling is to map the species in global chemistry model CAM-Chem to the regional chemistry model CMAQ, listed in Table 2.2 [*Emmons et al.*, 2010; *Yarwood et al.*, 2005]. During this process, most species can be mapped directly between these two models except secondary organic aerosol (SOA). Bulk aerosol model was used in CAM-chem [*Lamarque et al.*, 2012], thus only combined anthropogenic and biogenic SOA was generated. However, a more sophisticated aerosol scheme 6 (AE6) was in CMAQ 5.0, including 24 semi-volatile SOA and 7 nonvolatile SOA [*Carlton et al.*, 2010]. No universal ratios can be applied to anthropogenic and biogenic SOA in order to achieve all SOA species in CMAQ. As suggested by Carlton et al. [2010], default profile initial and boundary conditions were first used to drive CMAQ simulations, and the ratios among SOA species were achieved from the outputs. These grid dependent ratios were applied to total anthropogenic SOA and biogenic SOA from CAM-Chem so as to achieve the initial and boundary conditions for all SOA species.

6.5.1 Initial and boundary conditions

In the downscaling process, CAM-Chem was used to provide the initial and boundary conditions for CMAQ. Initial conditions are needed only for the first time step while the temporal resolution of boundary conditions is usually 3 hourly or 6 hourly in order to represent diurnal patterns. Three hourly boundary conditions were generated to achieve better diurnal representation.

First of all, it is important to keep the downscaled initial and boundary conditions consistent with CAM-Chem. Figure 6.2 shows the boundary conditions for the continental US domain used in CMAQ and the corresponding grids in CAM-Chem. Due

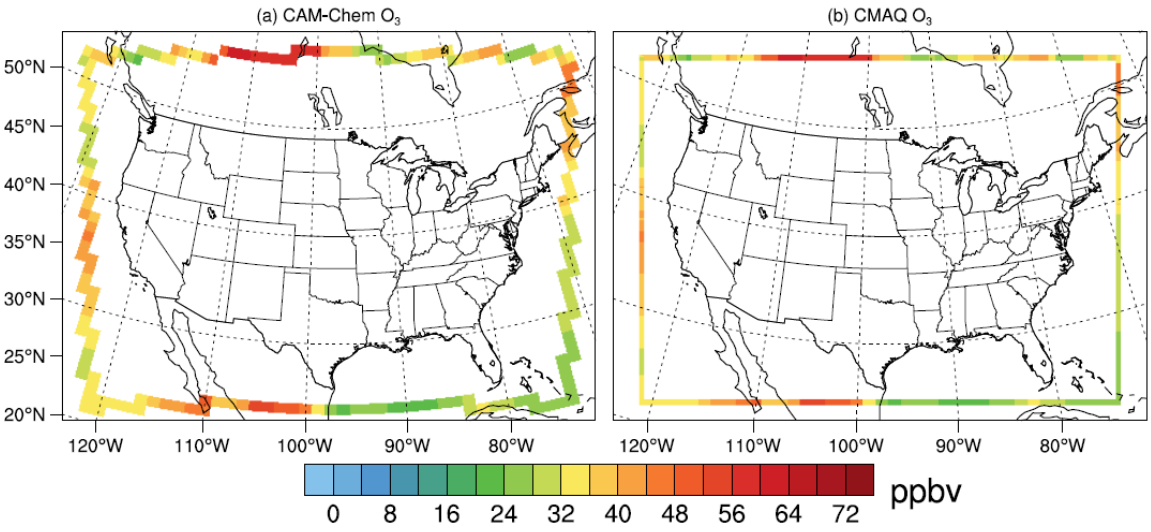

Figure 6.2 Boundary comparisons between CAM-Chem and CMAQ for O_3 concentrations at on July 1st, 2001

to the differences of spatial resolutions between CAM-Chem and CMAQ, the grids in CAM-Chem closest to CMAQ ones were used. Thus, unlike the domain used in CMAQ (Figure 6.2 (b)), the grids in CAM-Chem (Figure 6.2(a)) are not located in the same rows or columns. Comparing Figure 6.2(a) and (b), they are consistent with each other in all the four boundaries, i.e., the high ozone areas in the top and lower left boundaries (between 60-70 ppbv), and the boundaries located in the Pacific ocean and Atlantic ocean show similar patterns. Initial conditions have also been checked and similar patterns were found.

Considering the vertical layer height differences between CAM-Chem and CMAQ, linear interpolations were applied to the layers in CAM-Chem. For a layer l in CMAQ, find two layers in CAM-Chem, where the lower and higher heights of layer l are located. Assume the lower height is located in the layer m (CAM-Chem) with the height of h_m and higher height is located in layer n (CAM-Chem) with the height of h_n. The interpolations were as follows, where C represents concentrations:

a) $m = n$

$C_l = C_m$

b) $n - m = 1$

$$C_l = \frac{(h_m - h_{l-1}) * C_m + (h_l - h_m) * C_n}{h_l - h_{l-1}}$$

c) $n - m \geq 2$

$$C_l = \frac{(h_m - h_{l-1}) * C_m + \sum_{i=m+1}^{n-1} C_i * (h_i - h_{i-1}) + (h_l - h_m) * C_n}{h_l - h_{l-1}}$$

6.5.2 Emission inventory

Since the initial year of RCP scenarios is 2005, the year of 2005 National Emission Inventory* was processed by Sparse Matrix Operator Kernel Emissions (SMOKE) 2.7, and then used to scale the emissions from 2001-2004. The scaling ratios for 2001-2004 were listed in Table 6.1, based on US EPA**. In Table 6.1, emissions in 2005 are listed with the unit of Tg, the emissions of the other years are listed as a ratio of 2005. The projections of future emissions in RCP 4.5 and RCP 8.5 are based on the RCP database***. However, the RCP emissions did not take into consideration of $PM_{2.5}$ and PM_{10}, which is required as emission input for CMAQ. Thus, the following assumption is used: the projection of $PM_{2.5}$ follows the summation of organic carbon (OC), black carbon (BC) and SO_4, while the projection of PM_{10} follows the summation of $PM_{2.5}$, coarse mode dust and sea salt emissions. Biogenic emissions are highly affected by meteorological conditions such as temperature and radiation, thus Biogenic Emissions Inventory System (BEIS) Modeling 3.12 was used to generate hourly biogenic emissions for each year at present (2001-2004) and future (2057-2059) climate.

From Table 6.1, most emissions show decreasing trends in both RCP 4.5 and RCP 8.5 scenarios: i.e., CO reduce more than 70%, NMVOC and NOx reduce close to 70% and

* http://www.epa.gov/ttn/chief/net/2005inventory.html#inventorydata
** http://www.epa.gov/ttn/chief/trends/index.html#tables
*** http://www.iiasa.ac.at/web-apps/tnt/RcpDb/dsd?Action=htmlpage&page=welcome

50% in RCP 8.5, 40% and 60% in RCP 4.5. On the contrary, the emissions of NH_3 increase in both scenarios, and methane emissions increase 60% in RCP 8.5.

Table 6.1 Projection factor for anthropogenic emissions

	Present climate				2005(Tg)	RCP 4.5			RCP 8.5		
	2001	2002	2003	2004		2057	2058	2059	2057	2058	2059
CO	1.142	1.194	1.129	1.065	93.030	0.272	0.268	0.264	0.246	0.243	0.240
NOX	1.139	1.117	1.078	1.039	18.914	0.342	0.338	0.334	0.493	0.487	0.482
PM10	1.121	1.008	1.006	1.003	21.149	0.552	0.552	0.551	0.542	0.540	0.538
PM2.5	1.282	1.022	1.015	1.007	5.456	0.761	0.754	0.747	0.422	0.417	0.413
SO2	1.092	1.012	1.008	1.004	14.594	0.169	0.166	0.163	0.148	0.137	0.126
VOC	0.929	1.149	1.112	1.074	18.421	0.632	0.630	0.628	0.314	0.310	0.306
NH3	0.904	1.012	1.008	1.004	4.085	1.254	1.253	1.252	1.536	1.544	1.551
CH4	1.202	1.187	1.172	1.156	32.180	0.893	0.888	0.883	1.612	1.626	1.640
BC	1.007	1.005	1.004	1.002	0.394	0.723	0.716	0.709	0.264	0.262	0.260
OC	1.145	1.109	1.073	1.036	1.141	1.060	1.051	1.042	0.609	0.606	0.604

6.6 Evaluation of model outputs

Statistical evaluation by matching the observations and model outputs temporally and spatially are commonly used in the retrospective studies and benchmarks have been established for evaluation criteria [*USEPA*, 2007]. However, in climate studies, regional area or monthly mean are usually used to evaluate the model performance [*Lam et al.*, 2011; *Lamarque et al.*, 2010]. This study aims to evaluate whether the statistical methods applied in the retrospective studies can be used in the climate studies. This hypothesis may not apply to global climate models considering the coarse spatial resolution; however, it is theoretically reasonable in regional climate/chemistry models considering improved meteorological conditions from downscaling, plus detailed and accurate regional high resolution emissions inventory. To test the evaluation, all the observations

from Air Quality System (AQS)* are used to evaluate the present climate period from 2001-2004. By matching temporally (hourly for gas species and daily for $PM_{2.5}$, PM_{10} and $PM_{2.5}$ sub-species) and spatially (grid match) with observations, statistical evaluation was shown in Table 6.2. The benchmarks in the retrospective study were also listed in the Table 6.2, and the comparison between the statistical metrics and benchmarks could provide important references for future climate studies.

There are a total of three group of metrics: Mean Fractional Bias/Mean Fractional Error (MFB/MFE), Normalized Mean Bias/Normalized Mean Error (NMB/NME), and Mean Normalized Bias (MNB) and Mean Normalized Error (MNE). Based on US EPA [2007], the benchmarks of MFB/MFE are ±15/35 for ozone, ±30/50 for $PM_{2.5}$, and ±50/75 for $PM_{2.5}$ species, and less stringent for less abundant $PM_{2.5}$ species. Among all these metrics, the MFB and MFE is the least biased, and the MNB and MNE are the most biased and least useful metrics, particularly when observations are small. Thus, MNB and MNE are only calculated for O_3 with 40 and 60 ppb cut off values. For all the 2086661 sites at present climate condition, all statistical metrics for O_3 with 40 ppbv cut off meets the criteria. For O_3 with 60 ppbv cut off, the absolute errors are less than 30%, while biases for all three metrics (MFB/NMB/MNB) are slightly lower than -15%. For $PM_{2.5}$, the metrics are slightly higher (10-25% higher) than the benchmarks, and this is considered to be acceptable for climate studies. For $PM_{2.5}$ species such as elemental carbon (EC), organic matters (OMC), and sulfate (SO4), MFB/MFE and NMB/NME are quite close (within ±10%) to benchmark. No benchmark is available for PM_{10}, and the performance shows it is close to $PM_{2.5}$. No benchmarks are available for CO and NO_2 either, and the biases are all less than 50% and with most of the errors less than 85%.

Thus, it is reasonable to apply statistical evaluation for high resolution regional climate studies, and the performance, particularly for MFB/MFE, is comparable to the benchmarks used in the retrospective study.

---

* http://www.epa.gov/ttn/airs/airsaqs/detaildata/downloadaqsdata.htm

Table 6.2 Statistical evaluations

	CO	NO3	NO2	O3_40[1]	O3_60[2]	PM10	EC	OMC	SO_4	$PM_{2.5}$
MFB	-29±2	-16±3	-9±3	-5±1	-21±1	-56±2	-8±5	-41±4	-26±3	-35±2
MFE	83±3	113±1	80±1	27±1	28±1	83±1	76±2	82±2	68±2	65±1
NMB	-41±2	28±6	-4±3	-1±1	-17±1	-50±2	0±8	-32±7	-35±3	-33±3
NME	63±1	122±4	71±2	25±1	24±1	67±1	78±3	74±2	63±1	58±1
MNB	/	/	/	1±1	-16±1	-14±3	/	/	/	-5±3
MNE	/	/	/	26±1	23±1	76±2	/	/	/	63±2
No. points	3051180	13531	3280637	2086661	487991	130421	16518	16518	16112	146483
Bench mark		50/75		15/35	15/35		50/75	50/75	50/75	30/50

[1]a cutoff value of 40 ppbv is set.

[2]a cutoff value of 60 ppbv is set.

6.7 Climate impact on air quality

Figure 6.3 shows the cumulative distributions of Maximum daily 8-hr ozone (MDA8) for present climate (2001-2004) and future climate (RCP 4.5 and RCP 8.5, 2057-2059). Overall, compared with present climate, the cumulative distribution of RCP 4.5 shift to the left, indicating reduced ozone concentrations under the emission reduction scenario RCP 4.5, which is also the case for most of the SRES A1 and A2 scenarios ([*Lam et al.*, 2011; *Nolte et al.*, 2008]). Comparing RCP 4.5 with RCP 8.5, the distribution shifting right in RCP 8.5 indicates higher ozone concentrations under this scenario. In RCP 8.5, the eastern areas of U.S. (Northeast, Southeast, Central and South) show ozone decrease in the high ozone concentration levels. However, the western areas (Northwest, West and North West Central) show increase in higher percentile ozone distributions. In addition, the percentage of exceeding 60 and 75 ppbv is also listed in Figure 6.3. The National Ambient Air Quality Standards (NAAQS) standard (2008) use 75 ppbv, and the reason for considering 60 ppbv is considering that the NAAQS might become more stringent in future. The negative numbers indicate ozone exceedance decrease in future compared with present. From Figure 6.3, all blue numbers (second row) are negative, indicating ozone concentration decreases in RCP 4.5. However, in RCP 8.5, the exceedance of 60

ppbv could increase by 5 to 10 % in the western United States. In both scenarios, VOCs and NOx has been reduced dramatically, more than 35% VOC and 75% NOx in RCP 4.5, 70% VOC and 50% NOx in RCP 8.5 have been reduced. However, the major emission differences of these two scenarios are the methane emissions. In RCP 4.5, about 10% reduction by 2050s, while in RCP 8.5 the methane is increasing (60% by 2050s). Thus, the increase of methane emissions could be one of the major drivers in future climate. In addition, the increase of ozone in RCP 8.5 is more noticeable in the western U.S, which is likely to be contributed by the increased boundary concentrations. More sensitivity studies are needed to achieve quantitative analysis of the boundary effects.

In addition, for each region, percentage change of areas of 3-year mean annual 4th MDA8 ozone exceeding 75 ppbv (NAAQS) was evaluated. In RCP 4.5, the largest decrease occurs in Southeast (63%), Central (75%) and South (48%), and In RCP 8.5, the largest decrease occur in the Central (31%). However, West North Central and Northwest show increase of 24% and 13%, respectively, in RCP 8.5.

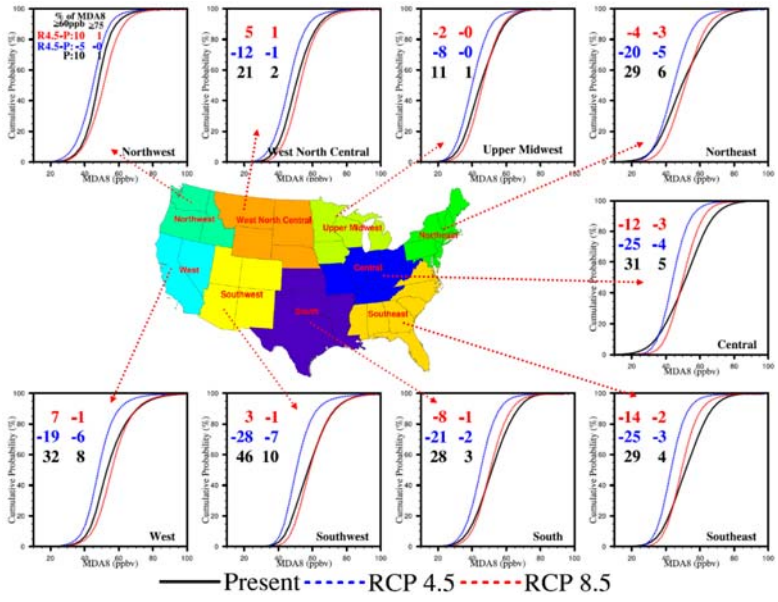

Figure 6.3 Cumulative distributions of MDA8 ozone. There are two columns of numbers: the numbers on the left show the percentage of MDA8 ozone exceeding 60 ppbv at present (2001-2004), the percentage change in RCP 4.5 (2057-2059, blue) and RCP 8.5 (2057-2059, red) compared with present; the numbers on the right are similar as left but for MDA8 ozone exceeding 75 ppbv

The distributions of $PM_{2.5}$ at present and future climate conditions were shown in Figure 6.4. As suggested in the NAAQS standard, a three-year average was used. At present, eastern US shows a regional mean of 5.2 to 8.0 ug/m3, with small areas near New York close to the NAAQS standard (15 $\mu g/m^3$). The western US show concentrations less than 4 ug/m^3, which is well below the NAAQS standard. In the future, all nine regions show mean concentrations less than 5 ug/m^3, with 16% to 39% reduction in RCP 4.5 and 28% to 44% reduction in RCP 8.5. Among the 9 regions, the $PM_{2.5}$ concentrations are 4% to 12% lower in RCP 8.5 than RCP 4.5, primarily from 30% more reductions of $PM_{2.5}$ in RCP 8.5 (Table 6.1). Unlike ozone, the changes of $PM_{2.5}$ are more directly related to emissions.

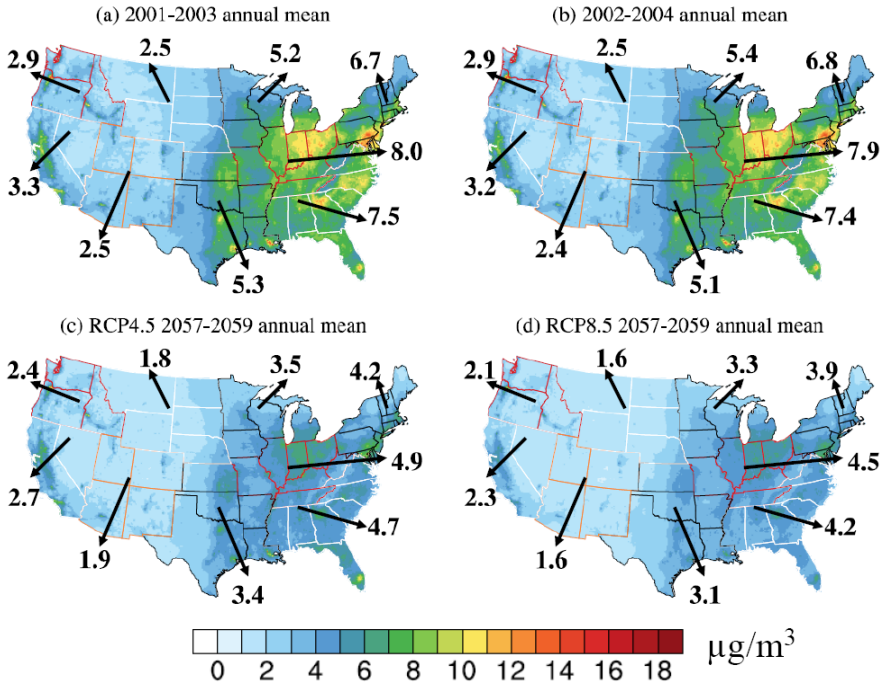

Figure 6.4 Three-year mean PM2.5 concentrations at present and future, the numbers along each figure represent mean concentrations in the 9 climate regions. The state boundary was labeled with different colors to distinguish different regions as shown in Figure 6.1.

6.8 More intense heat waves and its impact on air quality

6.8.1 Heat wave duration and frequency (number of annual events)

To date, the studies of climate impact on air quality have been focused on the comparison between different climate scenarios or different emissions scenarios [*Kawase et al.*, 2011; *Lam et al.*, 2011; *Nolte et al.*, 2008]. However, in the same scenario, under different meteorological conditions, such as a heat wave period and non-heat wave period, ozone could increase. This is very important particularly for control strategies or policies. Thus, heat waves were first investigated and followed by the impact of heat waves on ozone formation.

Two key parameters of heat waves were used on an annual basis: duration and frequency. The definitions of heat wave duration (number of days during a heat wave) and frequency (number of heat wave events per year) have been discussed in Section 5.7.1.

Figure 6.5 shows the heat wave duration and frequency at present and future climate. At present (Figure 6.5a,b), the heat wave duration ranges from 3.7 to 4.4 days per event, and the number of annual heat wave events are 1 to 1.5. In RCP 4.5 (Figure 6.5c,d), by the end of 2050s, most of the regions show increasing trends for heat wave duration except Central and Upper Midwest, showing little or a slight decrease. The mean increase of duration across the entire US is 23%, while the largest increase is 68% occurring in the Southwest. For the annual number of events, all the regions show increase patterns, with mean increase in US of 131%. The increase in Northeast and Northwest reach more than 2 times compared with present climate. Much more intense heat waves were projected to occur in RCP 8.5 (Figure 6.5e,f), with mean increase of 54% and 313% for duration and frequency, more than 2 times higher than the increase in RCP 4.5 (23% and 131%). The duration increase ranges from 29% to 90% among the 9 regions; the increase of events is more significant, and the least increase is 173% in the West, while the highest increase reaches 564% in Northeast.

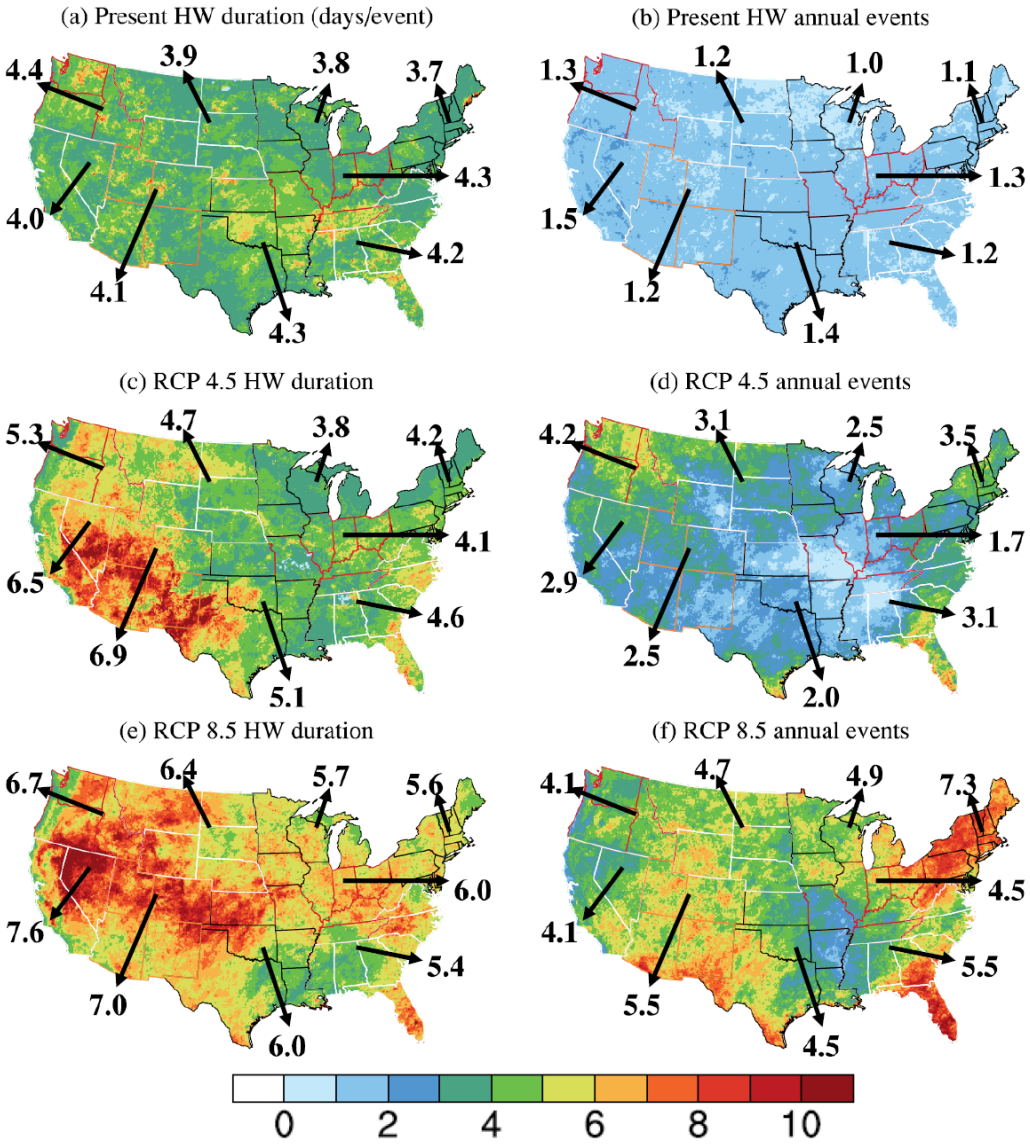

Figure 6.5 The heat wave duration and frequency. The state boundary was labeled with different colors to distinguish different regions as shown in Figure 6.1.

6.8.2 Impact of heat waves on ozone

In the same scenario, the emission differences among different days are expected to be minimal. Thus, the meteorological conditions could play the most important role. As is shown in Figure 6.6, in a majority of the regions, there are right shifts of distribution during the heat wave period compared to non-heat wave period, which pushes the higher MDA8 values accounting for a larger percentage. Except Southeast, in RCP 8.5, all other

regions show higher percentage of MDA8 ozone over 75 ppb, particularly, three regions (West, Southwest and West North Central) show differences of higher than 15%. For MDA8 ozone over 60 ppbv, 2/3 of the regions show higher than 15% during the heat wave period. The mean MDA8 differences in the regions except Southeast during heat wave days in RCP 8.5 are 3.1 to 9.5 ppbv.

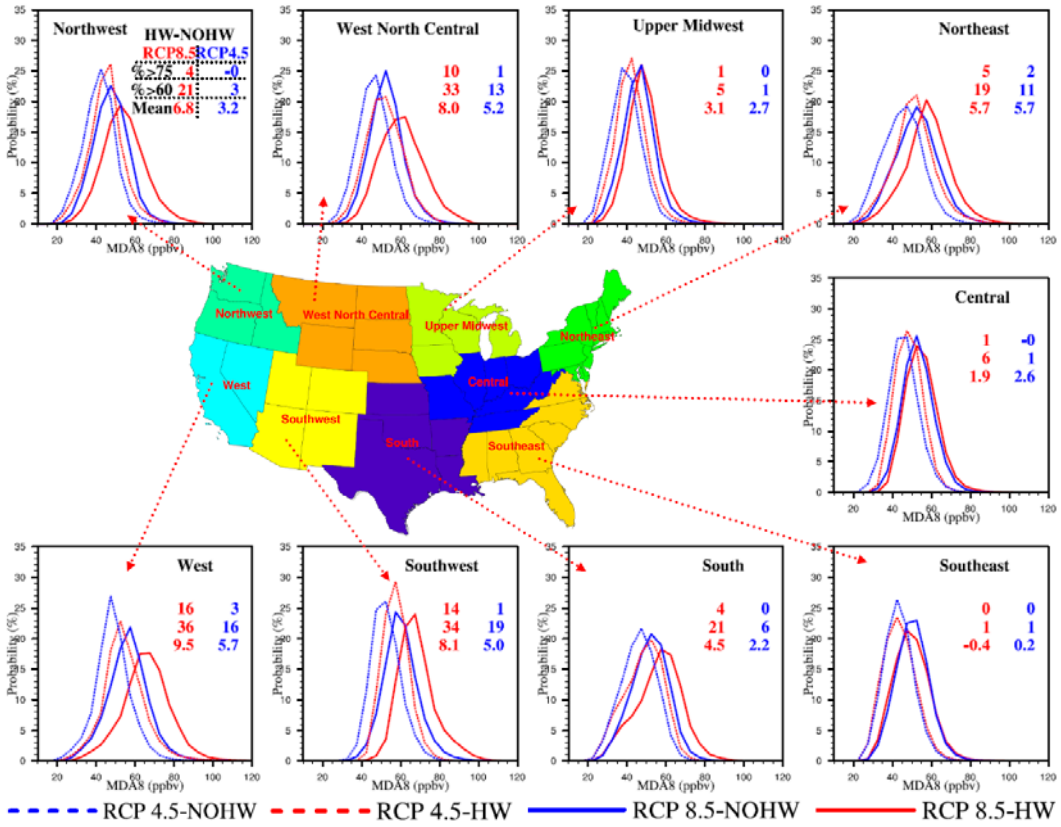

Figure 6.6 Distributions of MDA8 during the heat wave period and non-heat wave period for RCP 4.5 and RCP 8.5. There are two columns of numbers, and they represent the differences of mean MDA8 ozone, percentage greater than 75 ppbv and 60 ppbv between heat wave period and non-heat wave period for RCP 4.5 and RCP 8.5.

Chapter VII

7 SUMMARY

7.1 Summary of the study

This study involves multiple scales of climate and chemistry modeling. First, the analysis of heat waves was based on an ensemble member of monthly/daily global climate data. Following the large scale analysis, this study tends to answer how much improvement can be achieved from a high resolution downscaling system. To answer this question, global climate simulations were conducted on a three hourly basis in order to provide high temporal boundary conditions. After that, dynamical downscaling was applied to the three hourly global model outputs, and provides initial and boundary conditions for regional climate model on a 4 km by 4 km high resolution scale. By comparing with observations, much improved skills were achieved in predicting heat waves and extreme precipitation through the implementation of high resolution downscaling. It demonstrates the necessity of high resolution regional modeling for evaluating local extreme weather events. However, due to the limitation of computational resources, only 3 years of future climate simulations were conducted. The inter-annual variability may change the conclusion when comparing future climate with present climate. Thus, multiple years (6-10 years) simulations are needed in future when the computational resources are available.

In addition to climate, chemistry module has also been implemented. It enables this study to investigate the climate impact, particularly heat waves, on air quality, which could provide useful information for policy makers. The skill comparison between global climate model and regional climate model was comprehensive, while similar comparison between global and regional chemistry modeling was not included in the dissertation. In future, comprehensive evaluations will be conducted to investigate the improvement from high resolution chemistry downscaling studies.

7.2 Summary from paper I

Ensemble regional heat waves with CCSM4 perform well compared with observations during the historical period (1948-2005), providing confidence for using the ensemble member outputs when performing heat wave studies.

Heat waves show widespread increases in both intensity and duration/frequency. These increases are associated with both absolute value increases and probability distribution shifts, and occur not only in summer, but also in other seasons, especially winter, based on SETD in the new modeling results. In the RCP scenarios, both heat wave intensity and duration/frequency show larger increases compared to previous studies conducted by Ganguly et al. [2009] and Meehl and Tebaldi [*Meehl and Tebaldi*, 2004]. These results stress the importance of adaptation and mitigation to future climate, and the necessity that all seasons be taken into consideration instead of focusing only on summer.

The three hourly outputs have been published in the Earth System Grid (http://esg2-gw.ccs.ornl.gov) and made publicly available for downscaling and for use in high resolution climate change studies that can be used to study the relationship between heat waves and public health on a county by county level.

7.3 Summary from paper 2

The regional climate dynamical downscaling technique has been successfully applied to CESM results for the RCP8.5 climate change scenario to generate high resolution climate outputs. When conducting dynamical downscaling, one should examine spatial patterns to determine whether consistency between models exists. In this study, the inconsistency in skin temperature between CESM and WRF was corrected by modifying the land/sea mask from CESM. The downscaling using CCSM has been widely studied, but no one has reported inconsistency of skin temperature so far. From this study, it is recommended downscaling studies using either CCSM/CESM or other global climate models compare the spatial patterns between global climate models and WPS outputs before producing WRF simulations.

The extreme events evaluations of CESM and WRF in comparison to NCDC network prove that WRF is more capable than CESM in reproducing local extreme events. The percentage improvement could reach as high as 97% in Florida for heat wave intensity, 91% in Maryland for heat wave duration, 98% in Kentucky for heat wave frequency, more than 95% in Wisconsin and Pennsylvania for both annual total extreme precipitation and annual extreme events. Thus, by taking advantage of high resolution topography and land use information, the dynamical downscaling dramatically improves the ability of reproducing heat wave and extreme precipitation over the Eastern US. Thus, the coarse resolution global climate model results may not be suitable for regional/local extreme climate studies.

The RCP8.5 scenario was used as an example to study the future climate in 2057-2059 compared to present climate in 2001-2004. By the end of 2050s, the heat waves become more severe in most regions of the Eastern US. The increases in the Northeast and Eastern Midwest are more than the Southeast, which reduces the severity of differences among the North and South regions. It is an indicator that Northeast and Eastern Midwest may suffer more resulting from a steeper increase in the severity of heat waves. The total annual extreme precipitation in both the Northeast and Southeast have a mean increase of 35% or more, suggesting a greater risk of flooding in future climate conditions. Considering both heat waves and extreme precipitation, the Northeast region shows the largest increases. Thus, it is important that the Northeast take actions to mitigate the impact from climate change in the next several decades.

7.4 Summary from paper 3

The evaluation is important step before pursuing any future projections. The climate studies do not represent a particular year, and thus only regional and annual mean is evaluated for most of the case. However, the regional model does have detailed and accurate emission inventory, and the regional climate downscaling also improves the meteorological conditions by taking advantage of local high resolution topography. Thus, it is possible and important to test the statistical evaluations used in retrospective studies.

The tests in this study showed strong confidence that the statistical metrics can be applied to climate studies, and the benchmarks in the retrospective studies could be applied to the climate studies, or with slight relaxation. Among all the metrics, MFB/MFE are the most useful ones, and particular for ozone, among 2086661 sites, they almost all fall within the benchmarks. This study provides important references for future climate studies, and further evaluations are needed to confirm the findings.

Unlike the studies comparing different emission scenarios, this study also investigated the impact of heat waves on the ozone formation under the same scenario. In both RCP 4.5 and RCP 8.5, most regions show significant right shifts of probability distribution for MDA8 ozone, indicating increased ozone concentrations during the heat wave period. The impact of heat waves on MDA8 ozone could be as large as 3.1 to 9.5 ppbv. This finding addresses important issues regarding future air quality control, as emission controls may not be adequate if the standard becomes more stringent.

Chapter VIII

8 FUTURE STUDIES

From this study, about 300 T data has been produced. It includes both global climate/chemistry and regional climate/chemistry modeling results. Further analysis can be conducted, such as the impact of heat waves on public health and the impact of extreme precipitation on agriculture and infrastructure, etc.

Currently, only 3 to 4 years of high resolution downscaling simulations were conducted. The downscaling tool can be used for longer simulations and other regions as well. In future, when the computational resources are available, decadal simulations can be produced. In addition, the high resolution downscaling can be applied to China or other regions, and evaluation of multiple regions will make a more interesting study.

The impact of climate on air quality is one of the major focuses in this study. In future, the feedback of aerosol to climate can be further explored. In addition, the chemistry downscaling is limited in U.S., and extending the region to China could be more important. Because the emissions in China may not reduce as high as that in U.S., and the long range transport could play an important role in U.S. air quality in future.

REFERENCES

Aghedo, A. M., K. W. Bowman, H. M. Worden, S. S. Kulawik, D. T. Shindell, J. F. Lamarque, G. Faluvegi, M. Parrington, D. B. A. Jones, and S. Rast (2011), The vertical distribution of ozone instantaneous radiative forcing from satellite and chemistry climate models, *J. Geophys. Res.*, *116*(D1), D01305.

Bell, J. L., L. C. Sloan, and M. A. Snyder (2004), Regional changes in extreme climatic events: A future climate scenario, *J. Climate*, *17*(1), 81-87.

Bell, M., R. Goldberg, C. Hogrefe, P. Kinney, K. Knowlton, B. Lynn, J. Rosenthal, C. Rosenzweig, and J. Patz (2007), Climate change, ambient ozone, and health in 50 US cities, *Climatic Change*, *82*(1), 61-76.

Bitz, C. M., K. M. Shell, P. R. Gent, D. A. Bailey, G. Danabasoglu, K. C. Armour, M. M. Holland, and J. T. Kiehl (2011), Climate Sensitivity of the Community Climate System Model, Version 4, *J. Climate*, *25*(9), 3053-3070.

Bonan, G. B. (1996), A land surface model (LSM version 1.0) for ecological, hydrological, and atmospheric studies: Technical description and user's guide., *NCAR Technical Note NCAR/TN-417+STR*.

Brohan, P., J. J. Kennedy, I. Harris, S. F. B. Tett, and P. D. Jones (2006), Uncertainty estimates in regional and global observed temperature changes: A new data set from 1850, *J. Geophys. Res.*, *111*(D12), D12106.

Byun, D., and J. K. S. Ching (1999), Science Algorithms of the EPA Models-3 CommunityMultiscale Air Quality (CMAQ) Modeling System.*Rep.*, 727 pp, U. S. Environmental Protection Agency, Office of Research and Development, EPA, Washington, DC.

Byun, D., and K. L. Schere (2006), Review of the governing equations, computational algorithms, and other components of the models-3 Community Multiscale Air Quality (CMAQ) modeling system, *Applied Mechanics Reviews*, *59*(1-6), 51-77.

Caldwell, P., H.-N. S. Chin, D. C. Bader, and G. Bala (2009), Evaluation of a WRF dynamical downscaling simulation over California, *Climatic Change: An Interdisciplinary, International Journal Devoted to the Description, Causes and Implications of Climatic Change*, *95*(3).

Carlton, A. G., P. V. Bhave, S. L. Napelenok, E. O. Edney, G. Sarwar, R. W. Pinder, G. A. Pouliot, and M. Houyoux (2010), Model Representation of Secondary Organic Aerosol in CMAQv4.7, *Environ. Sci. Technol.*, *44*(22), 8553-8560.

Chen, F., and J. Dudhia (2001), Coupling an Advanced Land Surface–Hydrology Model with the Penn State–NCAR MM5 Modeling System. Part I: Model Implementation and Sensitivity, *Mon. Weather. Rev.*, *129*(4), 569-585.

Danabasoglu, G., S. C. Bates, B. P. Briegleb, S. R. Jayne, M. Jochum, W. G. Large, S. Peacock, and S. G. Yeager (2011), The CCSM4 Ocean Component, *J. Climate*, *25*(5), 1361-1389.

Deng, A., and D. R. Stauffer (2006), On Improving 4-km Mesoscale Model Simulations, *Journal of Applied Meteorology and Climatology*, *45*(3), 361-381.

Diaz-Nieto, J., and R. L. Wilby (2005), A comparison of statistical downscaling and climate change factor methods: impacts on low flows in the River Thames, United Kingdom, *Climatic Change*, *69*(2), 245-268.

Dickinson, R. E., R. M. Errico, F. Giorgi, and G. T. Bates (1989), A regional climate model for the western United States, *Climatic Change*, *15*(3), 383-422.

Dickinson, R. E., K. W. Oleson, G. Bonan, F. Hoffman, P. Thornton, M. Vertenstein, Z.-L. Yang, and X. Zeng (2006), The Community Land Model and its climate statistics as a component of the Community Climate System Model, *J. Climate*, *19*(11), 2302-2324.

Diffenbaugh, N. S., J. L. Bell, and L. C. Sloan (2006), Simulated changes in extreme temperature and precipitation events at 6 ka, *Paleogeogr. Paleoclimatol. Paleoecol.*, *236*(1-2), 151-168.

Dukowicz, J. K., and R. D. Smith (1994), Implicit free-surface method for the Bryan-Cox-Semtner ocean model, *J. Geophys. Res.*, *99*(C4), 7991-8014.

Emmons, L. K., et al. (2010), Description and evaluation of the Model for Ozone and Related chemical Tracers, version 4 (MOZART-4), *Geosci. Model Dev.*, *3*(1), 43-67.

Fowler, H. J., S. Blenkinsop, and C. Tebaldi (2007), Linking climate change modelling to impacts studies: recent advances in downscaling techniques for hydrological modelling, *International Journal of Climatology*, *27*(12), 1547-1578.

Ganguly, A. R., K. Steinhaeuser, D. J. Erickson, M. Branstetter, E. S. Parish, N. Singh, J. B. Drake, and L. Buja (2009), Higher trends but larger uncertainty and geographic variability in 21st century temperature and heat waves, *Proc. Natl. Acad. Sci. USA*, *106*(37), 15555-15559.

Gao, Y., J. S. Fu, J. B. Drake, Y. Liu, and J.-F. Lamarque (2012), Projected changes of extreme weather events in the Eastern United States based on a high-resolution climate modeling system, *Environ. Res. Lett.*, *7*, 044025.

Gent, P., S. Yeager, R. Neale, S. Levis, and D. Bailey (2010), Improvements in a half degree atmosphere/land version of the CCSM, *Climate Dynamics*, *34*(6), 819-833.

Gent, P. R., et al. (2011), The Community Climate System Model Version 4, *J. Climate*, *24*(19), 4973-4991.

Giorgi, F. (1990), Simulation of Regional Climate Using a Limited Area Model Nested in a General Circulation Model, *J. Climate*, *3*(9), 941-963.

Giorgi, F., and R. Francisco (2000), Uncertainties in regional climate change prediction: a regional analysis of ensemble simulations with the HADCM2 coupled AOGCM, *Climate Dynamics*, *16*(2-3), 169-182.

Giorgi, F., C. Shields Brodeur, and G. T. Bates (1994), Regional Climate Change Scenarios over the United States Produced with a Nested Regional Climate Model, *J. Climate*, *7*(3), 375-399.

Hansen, J., M. Sato, and R. Ruedy (2012), Perception of climate change, *Proc. Natl. Acad. Sci. USA*, *published ahead of print August 20, 2012, doi:10.1073/pnas.1205276109*.

Holland, M. M., D. A. Bailey, B. P. Briegleb, B. Light, and E. Hunke (2011), Improved Sea Ice Shortwave Radiation Physics in CCSM4: The Impact of Melt Ponds and Aerosols on Arctic Sea Ice, *J. Climate*, *25*(5), 1413-1430.

Hong, S.-Y., and J.-O. Lim (2006), The WRF Single-Moment 6-Class Microphysics Scheme (WSM6), *J. Korean Meteor. Soc.*, *42*(2), 129-151.

Hostetler, S. W., F. Giorgi, G. T. Bates, and P. J. Bartlein (1994), Lake-atmosphere feedbacks associated with paleolakes bonneville and lahontan, *Science*, *263*(5147), 665-668.

Huang, H.-C., et al. (2008), Impacts of long-range transport of global pollutants and precursor gases on U.S. air quality under future climatic conditions, *J. Geophys. Res.*, *113*(D19), D19307.

Hunke, E. C., and W. H. Lipscomb (2008), CICE: the Los Alamos Sea Ice Model, Documentation and Software, Version 4.0, *Los Alamos National Laboratory Tech. Rep. LA-CC-06-012.*

Huth, R., J. Kysely, and L. Pokorna (2000), GCM simulation of heat waves, dry spells, and their relationships to circulation, *Climatic Change*, *46*(1), 29-60.

Iacono, M. J., J. S. Delamere, E. J. Mlawer, M. W. Shephard, S. A. Clough, and W. D. Collins (2008), Radiative forcing by long-lived greenhouse gases: Calculations with the AER radiative transfer models, *J. Geophys. Res.*, *113*(D13), D13103.

IPCC (2007), Climate Change 2007: The Physical Science Basis. Contribution of Working Group I to the Fourth Assessment Report of the Intergovernmental Panel on Climate Change*Rep.*, 1008 pp, Cambridge University Press, Cambridge, United Kingdom and New York, NY, USA.

IPCC 2007 Climate Change 2007: The Physical Science Basis. Contribution of Working Group I to the Fourth Assessment Report of the Intergovernmental Panel on Climate Change ed S Solomon, D Qin, M Manning, M Marquis, K Averyt, M Tignor, H L Miller and Z Chen (Cambridge: Cambridge University Press)

Janjić, Z. I. (1990), The Step-Mountain Coordinate: Physical Package, *Mon. Weather. Rev.*, *118*(7), 1429-1443.

Kain, J. S. (2004), The Kain–Fritsch Convective Parameterization: An Update, *Journal of Applied Meteorology*, *43*(1), 170-181.

Karl, T. R., and R. W. Knight (1997), The 1995 Chicago heat wave: how likely is a recurrence?, *Bull. Amer. Meteor. Soc.*, *78*(6), 1107-1119.

Kawase, H., T. Nagashima, K. Sudo, and T. Nozawa (2011), Future changes in tropospheric ozone under Representative Concentration Pathways (RCPs), *Geophys. Res. Lett.*, *38*(5), L05801.

Kelly, J., P. A. Makar, and D. A. Plummer (2012), Projections of mid-century summer air-quality for North America: effects of changes in climate and precursor emissions, *Atmos. Chem. Phys. Discuss.*, *12*(2), 3875-3940.

Lam, Y. F., J. S. Fu, S. Wu, and L. J. Mickley (2011), Impacts of future climate change and effects of biogenic emissions on surface ozone and particulate matter concentrations in the United States, *Atmos. Chem. Phys.*, *11*(10), 4789-4806.

Lamarque, J.-F., and S. Solomon (2010), Impact of Changes in Climate and Halocarbons on Recent Lower Stratosphere Ozone and Temperature Trends, *J. Climate*, *23*(10), 2599-2611.

Lamarque, J.-F., J. R. McConnell, D. T. Shindell, J. J. Orlando, and G. S. Tyndall (2011a), Understanding the drivers for the 20th century change of hydrogen peroxide in Antarctic ice-cores, *Geophys. Res. Lett.*, *38*(4), L04810.

Lamarque, J.-F., G. Kyle, M. Meinshausen, K. Riahi, S. Smith, D. van Vuuren, A. Conley, and F. Vitt (2011b), Global and regional evolution of short-lived radiatively-active gases and aerosols in the Representative Concentration Pathways, *Climatic Change*, *109*(1), 191-212.

Lamarque, J. F., et al. (2012), CAM-chem: description and evaluation of interactive atmospheric chemistry in the Community Earth System Model, *Geosci. Model Dev.*, *5*(2), 369-411.

Lamarque, J. F., et al. (2010), Historical (1850–2000) gridded anthropogenic and biomass burning emissions of reactive gases and aerosols: methodology and application, *Atmos. Chem. Phys.*, *10*(15), 7017-7039.

Lawrence, D. M., P. E. Thornton, K. W. Oleson, and G. B. Bonan (2007), The Partitioning of Evapotranspiration into Transpiration, Soil Evaporation, and Canopy Evaporation in a GCM: Impacts on Land–Atmosphere Interaction, *J. Hydrometeorol*, *8*(4), 862-880.

Lawrence, D. M., K. W. Oleson, M. G. Flanner, C. G. Fletcher, P. J. Lawrence, S. Levis, S. C. Swenson, and G. B. Bonan (2011), The CCSM4 land simulation, 1850-2005: Assessment of surface climate and new capabilites, *J. Climate, accepted*.

Leung, L. R., M. S. Wigmosta, S. J. Ghan, D. J. Epstein, and L. W. Vail (1996), Application of a subgrid orographic precipitation/surface hydrology scheme to a mountain watershed, *J. Geophys. Res.*, *101*(D8), 12803-12817.

Lo, J. C.-F., Z.-L. Yang, and R. A. Pielke, Sr. (2008), Assessment of three dynamical climate downscaling methods using the Weather Research and Forecasting (WRF) model, *J. Geophys. Res.*, *113*(D9), D09112.

Lott, N., and T. Ross (2006), Tracking billion-dollar U.S. weather disasters, *Bull. Amer. Meteor. Soc.*, *87*(5), 557-559.

McGregor, J. L., and K. Walsh (1994), Climate change simulations of Tasmanian precipitation using multiple nesting, *J. Geophys. Res.*, *99*(D10), 20889-20905.

Meehl, G. A., and C. Tebaldi (2004), More intense, more frequent, and longer lasting heat waves in the 21st century, *Science*, *305*(5686), 994-997.

Meehl, G. A., C. Tebaldi, G. Walton, D. Easterling, and L. McDaniel (2009), Relative increase of record high maximum temperatures compared to record low minimum temperatures in the U.S, *Geophys. Res. Lett.*, *36*(23), L23701.

Meehl, G. A., et al. (2011), Climate system response to external forcings and climate change projections in CCSM4, *J. Climate*, *25*(11), 3661-3683.

Mellor, G. L., and T. Yamada (1982), DEVELOPMENT OF A TURBULENCE CLOSURE-MODEL FOR GEOPHYSICAL FLUID PROBLEMS, *Reviews of Geophysics*, *20*(4), 851-875.

Morcrette, J. J., H. W. Barker, J. N. S. Cole, M. J. Iacono, and R. Pincus (2008), Impact of a New Radiation Package, McRad, in the ECMWF Integrated Forecasting System, *Mon. Weather. Rev.*, *136*(12), 4773-4798.

Moss, R. H., et al. (2010), The next generation of scenarios for climate change research and assessment, *Nature*, *463*, 747-756.

Nakicenovic, N., and R. Swart (2000), *Special Report on Emissions Scenarios: A Special Report of Working Group III of the Intergovernmental Panel on Climate Change*,

Cambridge University Press, Cambridge, United Kingdom and New York, NY, USA.
Neale, R. B., J. H. Richter, and M. Jochum (2008), The Impact of Convection on ENSO: From a Delayed Oscillator to a Series of Events, *J. Climate*, *21*(22), 5904-5924.
Neale, R. B., et al. (2010), Description of the NCAR Community Atmosphere Model (CAM 4.0), NCAR Tech. Note NCAR/TN-XXX+STR (Draft)*Rep.*, 194 pp, National Center for Atmospheric Research, Boulder, Colorado.
Nolte, C. G., A. B. Gilliland, C. Hogrefe, and L. J. Mickley (2008), Linking global to regional models to assess future climate impacts on surface ozone levels in the United States, *J. Geophys. Res.*, *113*(D14), D14307.
Oleson, K. W., et al (2010), Technical Description of version 4.0 of the Community Land Model (CLM), *NCAR Technical Note NCAR/TN-478+STR*.
Pan, L.-L., S.-H. Chen, D. Cayan, M.-Y. Lin, Q. Hart, M.-H. Zhang, Y. Liu, and J. Wang (2011), Influences of climate change on California and Nevada regions revealed by a high-resolution dynamical downscaling study, *Climate Dynamics*, *37*(9), 2005-2020.
Parmesan, C., and P. Martens (2008), *Climate change, wildlife and human health. Ch. 14 in: SCOPE Assessment: Biodiversity, Global Change and Human Health: from Ecosystem Services to Spread of Disease*, Island Press.
Parmesan, C., T. L. Root, and M. R. Willig (2000), Impacts of Extreme Weather and Climate on Terrestrial Biota, *Bull. Amer. Meteor. Soc.*, *81*(3), 443-450.
Podzun, R., A. Cress, D. Majewski, and V. Renner (1995), Simulation of European climate with a limited area model. II: AGCM boundary conditions, *Contrib. Atmos. Phys.*, *68*, 205-225.
Qian, Y., S. J. Ghan, and L. R. Leung (2010), Downscaling hydroclimatic changes over the Western US based on CAM subgrid scheme and WRF regional climate simulations, *International Journal of Climatology*, *30*(5), 675-693.
Riahi, K., A. Grübler, and N. Nakicenovic (2007), Scenarios of long-term socio-economic and environmental development under climate stabilization, *Technological Forecasting and Social Change*, *74*(7), 887-935.
Robine, J.-M., S. L. K. Cheung, S. Le Roy, H. Van Oyen, C. Griffiths, J.-P. Michel, and F. R. Herrmann (2008), Death toll exceeded 70,000 in Europe during the summer of 2003, *Comptes Rendus Biologies*, *331*(2), 171-178.
Salathé, E. P., R. Steed, C. F. Mass, and P. H. Zahn (2008), A High-Resolution Climate Model for the U.S. Pacific Northwest: Mesoscale Feedbacks and Local Responses to Climate Change, *J. Climate*, *21*(21), 5708-5726.
Salinger, M. J., and G. M. Griffiths (2001), Trends in New Zealand daily temperature and rainfall extremes, *International Journal of Climatology*, *21*(12), 1437-1452.
Schar, C., P. L. Vidale, D. Luthi, C. Frei, C. Haberli, M. A. Liniger, and C. Appenzeller (2004), The role of increasing temperature variability in European summer heatwaves, *Nature*, *427*(6972), 332-336.
Skamarock, W. C., and J. B. Klemp (2008), A time-split nonhydrostatic atmospheric model for weather research and forecasting applications, *J. Comput. Phys.*, *227*(7), 3465-3485.

Smith, R., and P. Gent (2004), The Parallel Ocean Program (POP) reference manual, Ocean Component of the Community Climate System Model (CCSM), *Los Alamos National Laboratory Tech. Rep. LAUR-10-01853*.
Smith, R. D., J. K. Dukowicz, and R. C. Malone (1992), Parallel ocean general circulation modeling, *Physica D: Nonlinear Phenomena*, *60*(1–4), 38-61.
Smith, R. D., S. Kortas, and B. Meltz (1995), Curvilinear coordinates for global ocean models, *Los Alamos National Laboratory Tech. Rep. LA-UR-95-1146*.
Smith, R. D., et al. (2010), The Parallel Ocean Program (POP) reference manual, Ocean Component of the Community Climate System Model (CCSM) and Community Earth System Model (CESM), *Los Alamos National Laboratory Tech. Rep. LAUR-10-01853*.
Smith, S. J., and T. M. L. Wigley (2006), Multi-Gas Forcing Stabilization with the MiniCAM, *Energy Journal*, *(Special Issue #3)*, 373-391.
Snyder, M. A., J. L. Bell, L. C. Sloan, P. B. Duffy, and B. Govindasamy (2002), Climate responses to a doubling of atmospheric carbon dioxide for a climatically vulnerable region, *Geophys. Res. Lett.*, *29*(11), 1514.
Stedman, J. R. (2004), The predicted number of air pollution related deaths in the UK during the August 2003 heatwave, *Atmos. Environ.*, *38*(8), 1087-1090.
Taylor, K. E., R. J. Stouffer, and G. A. Meehl (2009), A Summary of the CMIP5 Experiment Design, http://www-pcmdi.llnl.gov/.
Taylor, K. E., R. J. Stouffer, and G. A. Meehl (2012), An Overview of CMIP5 and the Experiment Design, *Bull. Am. Meteorol. Soc.*, *93*(4), 485-498.
Tebaldi, C., K. Hayhoe, J. M. Arblaster, and G. A. Meehl (2006), Going to the extremes: An intercomparison of model-simulated historical and future changes in extreme events, *Climatic Change*, *79*, 185-211.
Thornton, P. E., J.-F. Lamarque, N. A. Rosenbloom, and N. M. Mahowald (2007), Influence of carbon-nitrogen cycle coupling on land model response to CO2 fertilization and climate variability, *Global Biogeochem. Cycles*, *21*(4), GB4018.
Thornton, P. E., S. C. Doney, K. Lindsay, J. K. Moore, N. Mahowald, J. T. Randerson, I. Fung, J. F. Lamarque, J. J. Feddema, and Y. H. Lee (2009), Carbon-nitrogen interactions regulate climate-carbon cycle feedbacks: results from an atmosphere-ocean general circulation model, *Biogeosciences*, *6*(10), 2099-2120.
Trenberth, K. E., J. C. Berry, and L. E. Buja (1993), Vertical Interpolation and Truncation of Model-coordinate Data*Rep.*, 54 pp, National Center for Atmospheric Research, Boulder, Colorado.
USEPA (2007), Guidance on the Use of Models and Other Analyses for Demonstrating Attainment of Air Quality Goals for Ozone, PM2.5. and Regional Haze, *EPA-454/B-07e002*.
Vieno, M., et al. (2010), Modelling surface ozone during the 2003 heat-wave in the UK, *Atmos. Chem. Phys.*, *10*(16), 7963-7978.
Weisheimer, A., and T. N. Palmer (2005), Changing frequency of occurrence of extreme seasonal temperatures under global warming, *Geophys. Res. Lett.*, *32*(20), L20721.

Whitman, S., G. Good, E. R. Donoghue, N. Benbow, W. Shou, and S. Mou (1997), Mortality in Chicago attributed to the July 1995 heat wave, *Am. J. Public. Health.*, *87*(9), 1515-1518.

Wise, M., K. Calvin, A. Thomson, L. Clarke, B. Bond-Lamberty, R. Sands, S. J. Smith, A. Janetos, and J. Edmonds (2009), Implications of Limiting CO2 Concentrations for Land Use and Energy, *Science*, *324*(5931), 1183-1186.

Wong, D. C., J. Pleim, R. Mathur, F. Binkowski, T. Otte, R. Gilliam, G. Pouliot, A. Xiu, J. O. Young, and D. Kang (2012), WRF-CMAQ two-way coupled system with aerosol feedback: software development and preliminary results, *Geosci. Model Dev.*, *5*(2), 299-312.

Yarwood, G., S. Rao, M. Yocke, and G. Whitten (2005), Updates to the Carbon Bond Chemical Mechanism: CB05.*Rep.*, U.S. Environmental Protection Agency, Research Triangle Park, NC.

APPENDIX

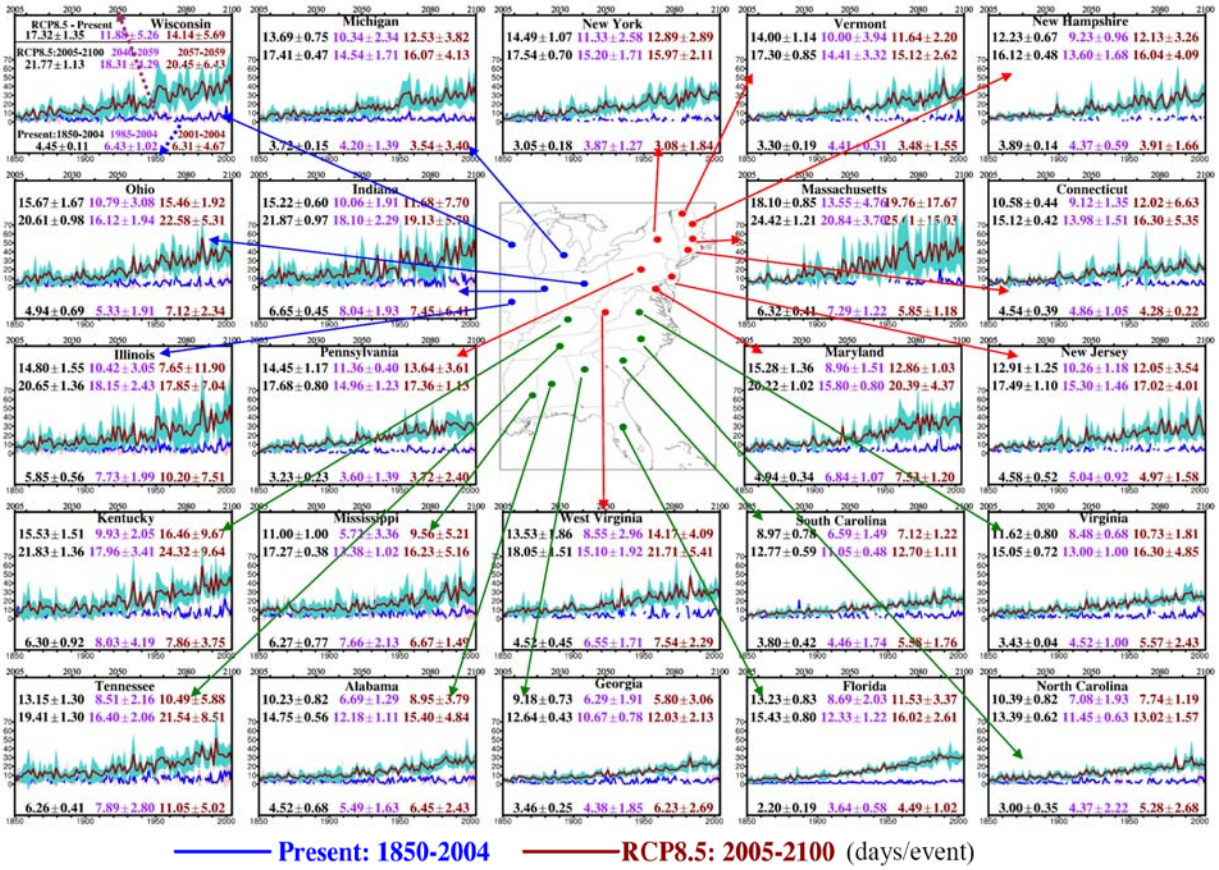

Figure A1. Ensemble heat wave duration ± one standard deviation (ºC) for present climate and future climate (RCP 8.5). The X axis for present climate is scaled at the bottom while the future climate (RCP 8.5) is scaled at the top. In each plot, there are three rows of numbers (marked at the top-left plot): At the bottom, the numbers from left to right indicate heat wave duration ensemble mean ± one standard deviation during 1850-2005, 1985-2004 and 2001-2004; In the middle, the numbers indicate the RCP 8.5 scenario for the period of 2005-2100, 2040-2059 and 2057-2059; At the top, the numbers indicate the differences between RCP 8.5 and present climate during the three periods listed above.

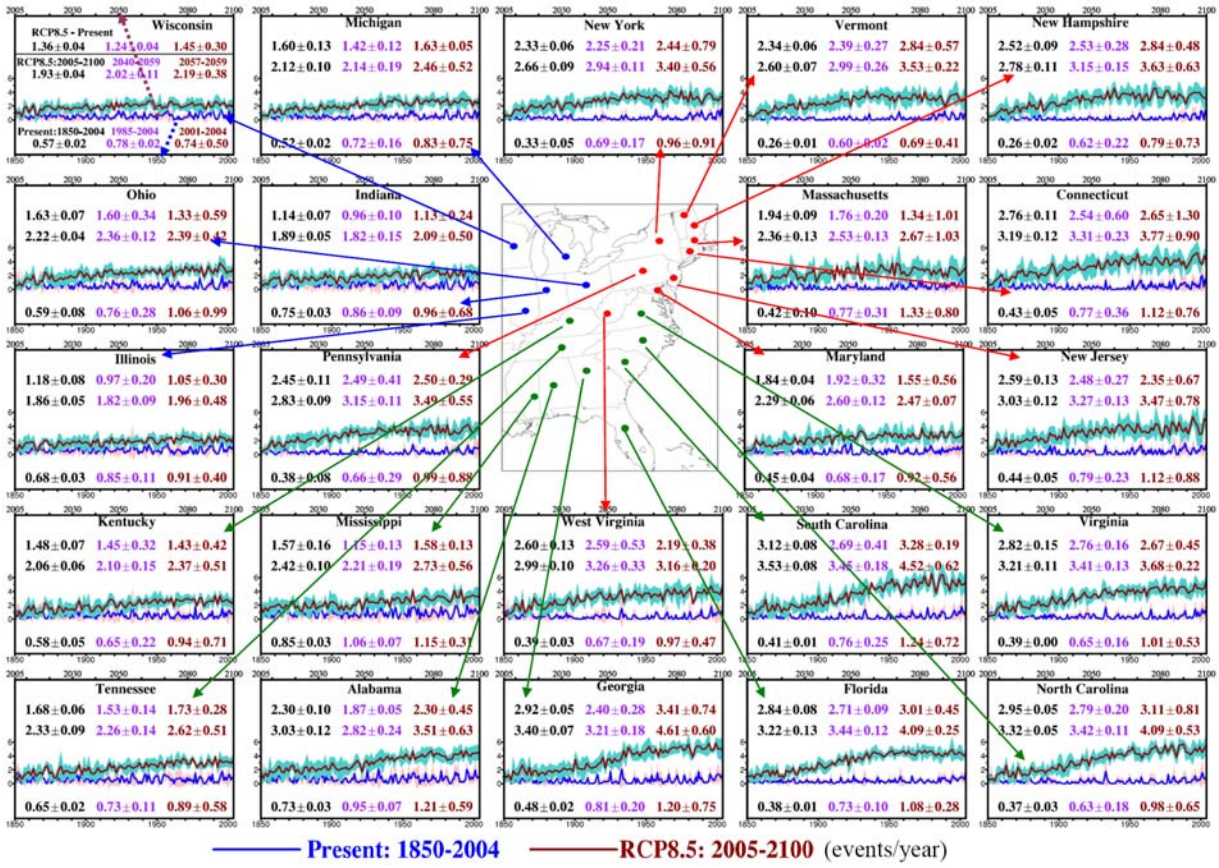

Figure A2 The same as Figure A1 but for heat wave events

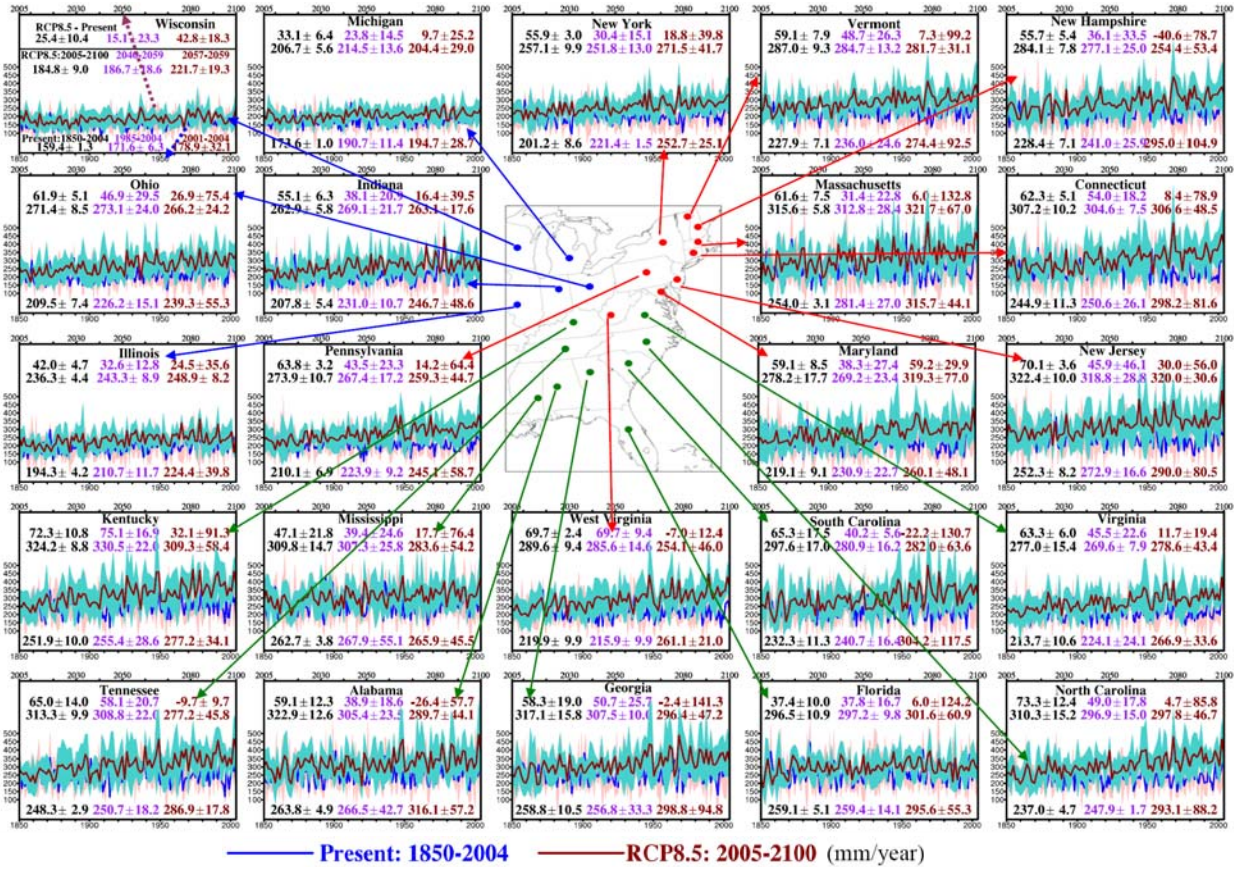

Figure A3 The same as Figure A1 but for annual total extreme precipitation

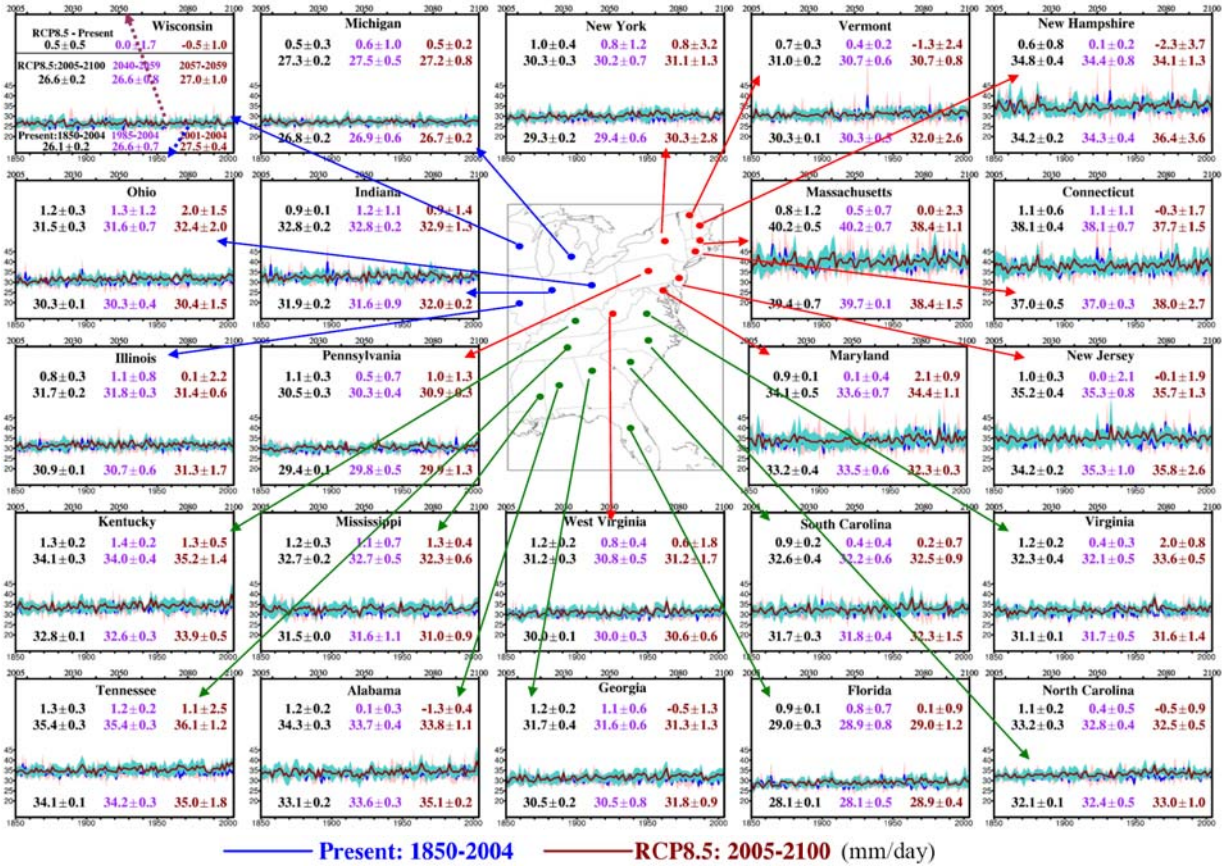

Figure A4 The same as Figure A1 but for daily mean extreme precipitation

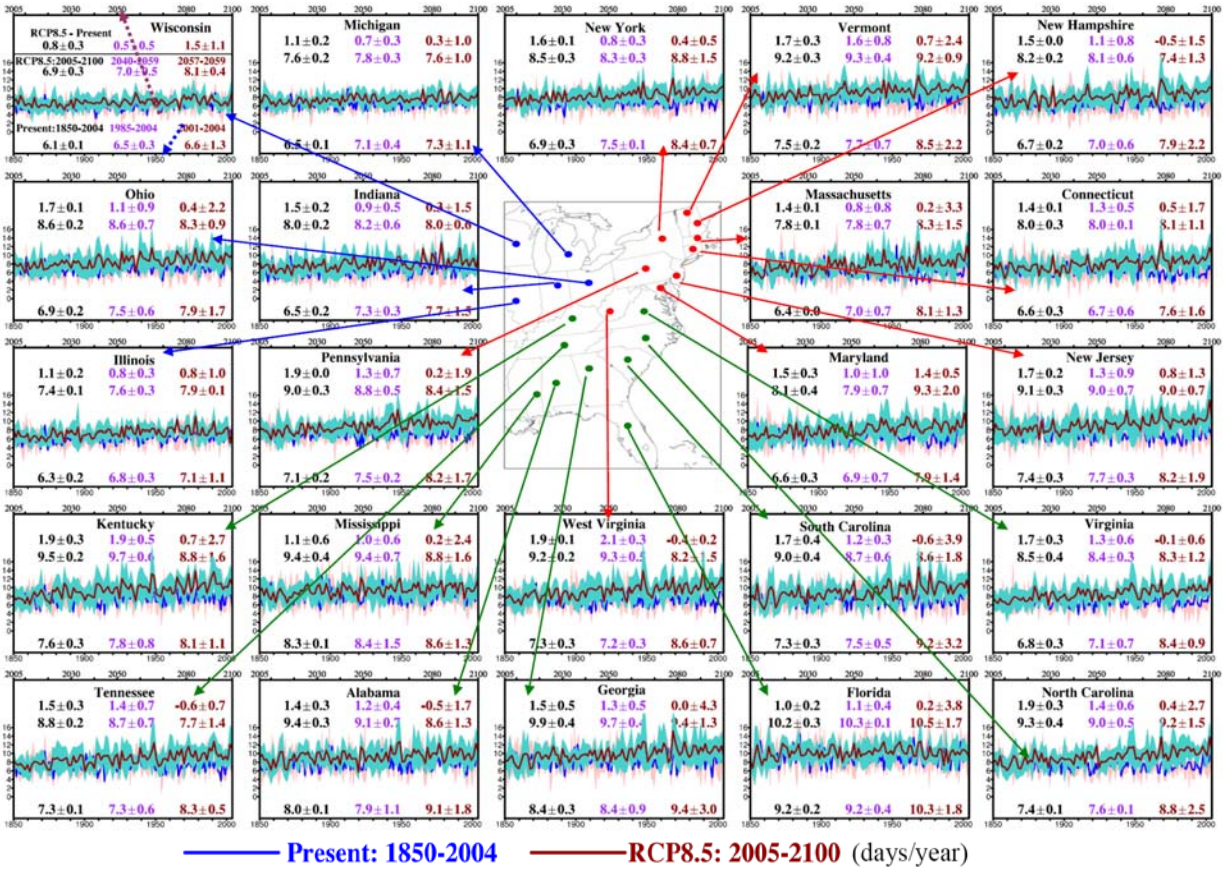

Figure A5. The same as Figure A1 but for annual total extreme precipitation days

Table A1 Heat wave duration ± one standard deviation

	Heat wave duration (days/event)		
Regions/States	Present	RCP 8.5	RCP 8.5 - Present
Northeast Region	**3.61±1.45**	**5.53±4.84**	**1.92±5.10**
New Hampshire	3.22±1.66	5.35±4.09	2.13±3.26
Vermont	3.37±1.55	5.35±2.62	1.98±2.20
Massachusetts	3.60±1.18	5.47±15.03	1.87±17.67
Connecticut	3.68±0.22	5.71±5.35	2.03±6.63
New York	3.78±1.84	5.32±2.11	1.54±2.89
Pennsylvania	3.85±2.40	5.48±1.13	1.63±3.61
New Jersey	3.59±1.58	5.49±4.01	1.90±3.54
Maryland	3.91±1.20	5.67±4.37	1.76±1.03
West Virginia	3.53±2.29	5.96±5.41	2.43±4.09
Midwest Region	**3.86±4.87**	**5.65±5.74**	**1.78±6.21**
Wisconsin	3.64±4.67	5.63±6.43	1.99±5.69
Michigan	3.96±3.40	5.00±4.13	1.04±3.82
Illinois	3.97±7.51	5.94±7.04	1.97±11.90
Indiana	3.87±6.41	5.87±5.79	2.00±7.70
Ohio	3.88±2.34	5.80±5.31	1.92±1.92
Southeast Region	**4.55±2.59**	**5.78±4.49**	**1.23±3.91**
Kentucky	4.22±3.75	6.28±9.64	2.06±9.67
Virginia	3.70±2.43	6.00±4.85	2.30±1.81
Tennessee	5.47±5.02	5.46±8.51	-0.01±5.88
North Carolina	3.82±2.68	6.45±1.57	2.63±1.19
Mississippi	4.70±1.49	4.41±5.16	-0.29±5.21
Alabama	4.96±2.43	4.57±4.84	-0.39±3.79
Georgia	4.98±2.69	5.66±2.13	0.68±3.06
South Carolina	4.41±1.76	6.08±1.11	1.67±1.22
Florida	4.66±1.02	7.11±2.61	2.45±3.37

Table A2 Heat wave frequency ± one standard deviation

	Heat wave frequency (events/year)		
Regions/States	Present	RCP 8.5	RCP 8.5 - Present
Northeast Region	**1.24±0.74**	**7.03±0.59**	**5.79±0.71**
New Hampshire	1.29±0.73	7.41±0.63	6.12±0.48
Vermont	1.15±0.41	7.94±0.22	6.79±0.57
Massachusetts	1.02±0.80	7.13±1.03	6.11±1.01
Connecticut	1.24±0.76	6.53±0.90	5.29±1.30
New York	0.96±0.91	7.65±0.56	6.69±0.79
Pennsylvania	1.33±0.88	7.26±0.55	5.93±0.29
New Jersey	1.36±0.88	6.26±0.78	4.90±0.67
Maryland	1.34±0.56	5.89±0.07	4.55±0.56
West Virginia	1.45±0.47	7.16±0.20	5.71±0.38
Midwest Region	**1.23±0.66**	**5.57±0.46**	**4.34±0.30**
Wisconsin	0.97±0.50	5.23±0.38	4.26±0.30
Michigan	1.20±0.75	5.78±0.52	4.58±0.05
Illinois	1.32±0.40	4.50±0.48	3.18±0.30
Indiana	1.37±0.68	5.66±0.50	4.29±0.24
Ohio	1.30±0.99	6.70±0.42	5.40±0.59
Southeast Region	**1.25±0.57**	**5.02±0.49**	**3.77±0.44**
Kentucky	1.41±0.71	4.48±0.51	3.07±0.42
Virginia	1.38±0.53	5.38±0.22	4.00±0.45
Tennessee	1.16±0.58	3.88±0.51	2.72±0.28
North Carolina	1.35±0.65	4.71±0.53	3.36±0.81
Mississippi	1.35±0.31	2.93±0.56	1.58±0.13
Alabama	1.12±0.59	4.33±0.63	3.21±0.45
Georgia	1.02±0.75	6.19±0.60	5.17±0.74
South Carolina	1.33±0.72	5.46±0.62	4.13±0.19
Florida	1.09±0.28	7.81±0.25	6.72±0.45

Table A3 Total annual extreme precipitation ± one standard deviation

	Total annual extreme precipitation (mm/year)		
Regions/States	Present	RCP 8.5	RCP 8.5 - Present
Northeast Region	**308.7±66.9**	**416.1±49.3**	**107.3±72.5**
New Hampshire	324.4±104.9	537.6±53.4	213.3±78.7
Vermont	286.2±92.5	415.7±31.1	129.5±99.2
Massachusetts	328.5±44.1	454.3±67.0	125.8±132.8
Connecticut	371.0±81.6	444.3±48.5	73.3 ±78.9
New York	292.5±25.1	332.5±41.7	40.0 ±39.8
Pennsylvania	290.8±58.7	359.8±44.7	69.0 ±64.4
New Jersey	307.7±80.5	458.4±30.6	150.7±56.0
Maryland	272.9±48.1	402.3±77.0	129.3±29.9
West Virginia	304.8±21.0	339.5±46.0	34.8 ±12.4
Midwest Region	**235.2±40.9**	**293.8±19.7**	**58.7 ±38.8**
Wisconsin	182.9±32.1	164.7±19.3	-18.3±18.3
Michigan	217.8±28.7	254.0±29.0	36.1 ±25.2
Illinois	208.0±39.8	322.9±8.2	114.9±35.6
Indiana	277.8±48.6	386.8±17.6	109.1±39.5
Ohio	289.3±55.3	340.8±24.2	51.5 ±75.4
Southeast Region	**294.6±60.4**	**405.0±51.6**	**110.4±81.8**
Kentucky	287.6±34.1	329.8±58.4	42.3 ±91.3
Virginia	262.0±33.6	388.2±43.4	126.3±19.4
Tennessee	293.2±17.8	365.7±45.8	72.5 ±9.7
North Carolina	338.1±88.2	477.7±46.7	139.6±85.8
Mississippi	226.0±45.5	286.8±54.2	60.8 ±76.4
Alabama	288.7±57.2	458.1±44.1	169.4±57.7
Georgia	330.4±94.8	490.7±47.2	160.4±141.3
South Carolina	323.1±117.5	482.4±63.6	159.4±130.7
Florida	302.1±55.3	365.4±60.9	63.3 ±124.2

Table A4. Daily extreme precipitation ± one standard deviation

	Daily extreme precipitation (mm/day)		
Regions/States	Present	RCP 8.5	RCP 8.5 - Present
Northeast Region	**51.1±2.2**	**52.6±1.1**	**1.5±2.2**
New Hampshire	49.7±3.6	55.7±1.3	6.0±3.7
Vermont	43.1±2.6	46.7±0.8	3.6±2.4
Massachusetts	54.5±1.5	56.7±1.1	2.1±2.3
Connecticut	61.4±2.7	60.7±1.5	-0.8±1.7
New York	45.7±2.8	44.9±1.3	-0.8±3.2
Pennsylvania	47.9±1.3	49.6±0.3	1.6 ±1.3
New Jersey	57.8±2.6	56.9±1.3	-0.9±1.9
Maryland	52.9±0.3	54.3±1.1	1.4 ±0.9
West Virginia	46.7±0.6	48.3±1.7	1.5±1.8
Midwest Region	**50.6±0.8**	**52.0±1.1**	**1.5±1.3**
Wisconsin	44.5±0.4	43.5±1.0	-1.0±1.0
Michigan	42.1±0.2	44.2±0.8	2.2±0.2
Illinois	55.6±1.7	60.0±0.6	4.4±2.2
Indiana	58.5±0.2	60.1±1.3	1.7±1.4
Ohio	52.1±1.5	52.3±2.0	0.2±1.5
Southeast Region	**56.8±1.0**	**60.6±1.0**	**3.9±0.9**
Kentucky	55.6±0.5	57.3±1.4	1.7±0.5
Virginia	50.2±1.4	54.5±0.5	4.4±0.8
Tennessee	57.8±1.8	59.4±1.2	1.6±2.5
North Carolina	59.3±1.0	64.6±0.5	5.3±0.9
Mississippi	57.4±0.9	60.4±0.6	3.0±0.4
Alabama	58.5±0.2	65.5±1.1	7.0±0.4
Georgia	59.3±0.9	63.6±1.3	4.3±1.3
South Carolina	57.9±1.5	62.9±0.9	5.0±0.7
Florida	55.0±0.4	57.7±1.2	2.7±0.9

Table A5 Annual extreme precipitation events ± one standard deviation

	Annual extreme precipitation events (days/year)		
Regions/States	Present	RCP 8.5	RCP 8.5 - Present
Northeast Region	**6.1±1.6**	**7.9±1.3**	**1.8 ±1.6**
New Hampshire	6.5±2.2	9.6±1.3	3.1 ±1.5
Vermont	6.5±2.2	8.8±0.9	2.2 ±2.4
Massachusetts	6.1±1.3	8.1±1.5	2.1 ±3.3
Connecticut	6.2±1.6	7.4±1.1	1.3 ±1.7
New York	6.4±0.7	7.4±1.5	1.0 ±0.5
Pennsylvania	6.1±1.7	7.3±1.5	1.2 ±1.9
New Jersey	5.4±1.9	8.1±0.7	2.8 ±1.3
Maryland	5.2±1.4	7.5±2.0	2.3 ±0.5
West Virginia	6.6±0.7	7.2±1.5	0.6 ±0.2
Midwest Region	**4.7±1.3**	**5.6±0.6**	**0.9 ±1.4**
Wisconsin	4.0±1.3	3.8±0.4	-0.2±1.1
Michigan	5.2±1.1	5.8±1.0	0.6 ±1.0
Illinois	3.7±1.1	5.3±0.1	1.6 ±1.0
Indiana	4.8±1.5	6.5±0.6	1.7 ±1.5
Ohio	5.6±1.7	6.6±0.9	1.1 ±2.2
Southeast Region	**5.2±1.8**	**6.7±1.5**	**1.5 ±2.5**
Kentucky	5.2±1.1	5.8±1.6	0.5 ±2.7
Virginia	5.2±0.9	7.1±1.2	1.9 ±0.6
Tennessee	5.1±0.5	6.2±1.4	1.1 ±0.7
North Carolina	5.7±2.5	7.4±1.5	1.7 ±2.7
Mississippi	4.0±1.3	4.8±1.6	0.8 ±2.4
Alabama	5.0±1.8	7.1±1.3	2.1 ±1.7
Georgia	5.6±3.0	7.8±1.3	2.2 ±4.3
South Carolina	5.6±3.2	7.7±1.8	2.1 ±3.9
Florida	5.6±1.8	6.4±1.7	0.8 ±3.8

VITA

Yang Gao was born in Qingdao, Shandong Province, China. In 2006, Yang graduated with a Bachelor of Engineering and a minor in computer science from Jilin Institute of Chemical Technology, Jilin, China. The same year, he enrolled at Tsinghua University, Beijing, China to pursue a Master in Environmental Engineering.

In 2008, Yang graduated with a Masters of Engineering from Tsinghua University and joined the PhD program on climate and air quality studies at the University of Tennessee. In December 2012, he graduated with a PhD in Civil Engineering and a minor in Computational Science.